FREQUENCY STABILITY IN THIN-FILM PIEZOELECTRIC-ON-SUBSTRATE OSCILATORS

BY

MOHSEN SHAHMOHAMMADI GHAHSAREH

Bachelor of Science in Electrical Engineering
Isfahan University of Technology
Isfahan, Iran
1995

Master of Science in Electrical Engineering
K. N. Toosi University of Technology
Tehran, Iran
1999

Submitted to the Faculty of the
Graduate College of the
Oklahoma State University
in partial fulfillment of
the requirements for
the Degree of
DOCTOR OF PHILOSOPHY
December, 2013

FREQUENCY STABILITY IN THIN-FILM

PIEZOELECTRIC-ON-SUBSTRATE OSCILLATORS

Dissertation Approved:

Dr. Reza Abdolvand

Dissertation Adviser

Dr. John M. Acken

Dr. Daryoosh Vashaee

Dr. Khaled Sallam

Outside Committee Member

ACKNOWLEDGEMENTS

This dissertation is dedicated to my parents, Hassan and Setareh, for their love and sacrifices throughout my life.

The completion of this dissertation would not have been possible without the encouragement and support of a number of individuals.

First and foremost, I would like to sincerely thank my adviser, Dr. Reza Abdolvand, whom I am deeply indebted to, for his inspiration and encouragement, patient teaching and guidance throughout the whole process of this dissertation.

I also appreciate my committee members for their time and effort to analyze my dissertation and provide constructive suggestions. My gratitude goes to Dr. John Acken, Dr. Khaled Sallam, and Dr. Daryoosh Vashaee. I would also thank Dr. Jerzy Krasinski for his valuable discussions in my defense presentation.

Finally, I would like to thank other graduate students, particularly Brandon P. Harrington, Hediyeh Fatemi, Mohammad Modarres-Zadeh, Jonathan Gonzales and Zachary Carpenter, who have been great sources of help and discussion.

Acknowledgements reflect the views of the author and are not endorsed by committee members or Oklahoma State University.

Name: MOHSEN SHAHMOHAMMADI GHAHSAREH

Date of Degree: December 2013

Title of Study: FREQUENCY STABILITY IN THIN-FILM PIEZOELECTRIC-ON-SUBSTRATE OSCILATORS

Major Field: ELECTRICAL ENGINEERING

Abstract: For many years, crystal oscillators have been used as the *de facto* frequency reference in almost all electronic platforms because they offer excellent stability and superior phase noise. This is mainly due to the high quality factor (Q) and exceptional temperature stability of quartz crystals. However, the size of quartz resonators is relatively large, and they cannot be readily integrated with microelectronics. This ultimately impedes the complete integration of the high-performance oscillators with the electronics. Achieving such integration will enable frequency control devices with a smaller form factor, lower cost, greater flexibility, and potentially higher reliability. Microelectromechanical systems (MEMS) resonator technology is gradually gaining popularity as a solution for the integration barrier and high-performance micro-machined oscillators have been presented by researchers and companies recently. However, one of the most important drawbacks of MEMS resonators has been their relatively large and linear temperature coefficient of frequency (TCF) (e.g., around −30 ppm/°C for Si-based).

The subject of this dissertation is on the frequency stability in thin-film piezoelectric-on-substrate oscillators (TPoS). In this regard, jitter and temperature dependency of the oscillation frequency are studied. The dependency of jitter of TPoS on the resonator characteristics (i.e. quality factor and motional impedance) is studied where the results provide experimental validation for the suppression of overall oscillator circuit noise through the operation of the resonator beyond the bifurcation.

A novel temperature compensation technique for silicon-based lateral-extensional MEMS oscillators is introduced, which is based on the properly orienting an extensional-mode resonator on a highly doped n-type silicon substrate. The existence of a local zero temperature coefficient of frequency (i.e., turnover point) in extensional-mode silicon microresonators, fabricated on highly n-type-doped substrates and aligned to the [100] crystalline orientation is demonstrated. It is shown that the turnover point in thin-film piezoelectric-on-silicon (TPoS) resonators is a function of doping concentration and orientation. Moreover, the turnover point can be adjusted by changing the thickness ratio of Si and the piezoelectric film (e.g., AlN) in the resonant structure. MEMS oscillators with controlled temperature coefficient of frequency (TCF), assembled through mixing the frequencies of two oscillators that are made of silicon micro-resonators with known and dissimilar TCF, are also introduced. Based on this method, a TPoS MEMS oscillator is assembled in which the first-order TCF is virtually cancelled resulting in a parabolic TCF curve (second-order TCF).

The frequency tuning in TPoS resonators is also reported which results show a great potential application in temperature compensated oscillators. Tuning is demonstrated through varying the termination load connected to an isolated tuning port. The dependency of frequency tuning on the design features of the resonator is studied as well.

TABLE OF CONTENTS

LIST OF TABLES

LIST OF FIGURES

CHAPTER I

INTRODUCTION

The mobile device market continues to grow at a fast pace, imposing very tight price and size margins for required components. Specially, in data and wireless communication, the clock generator is an essential building block of the system. For many years, resonators such as quartz crystals (XTALs), SAW (surface acoustic wave) and ceramic resonators have been commonly employed in clock generators. Crystal oscillators (XOs) as the de facto frequency reference have been used in almost all electronic platforms since they offer high quality factor (Q) and excellent temperature frequency stability.

However, the drawbacks of quartz resonators are their large size, hard to be batch processed and incompatibility of fabrication process. Since quartz crystals cannot be integrated into microelectronic form, it holds back the complete integration of the high-performance oscillators with the rest of electronics. Achieving that goal would enable frequency control devices with a smaller form-factor, lower cost, greater flexibility, higher reliability and many other astonishing potential benefits. Integration into microelectronic form will also be of much greater importance for realization of future generations of portable devices in which several oscillators at different frequencies are demanded in an extremely small foot print area.

One possible candidate to replace the current bulky quartz based oscillators is a high quality factor micromachined resonator, which can be fabricated on-chip. Efforts to replace quartz with

such a technology date back to the 1960's. In 1967, a transistor was presented with a mechanically resonant gate [1]. Likewise, the frequency stability of solid-state oscillators, was also investigated [2]. Those efforts were limited since the performance of frequency control devices based on these technologies was poorer than which could be achieved with quartz crystals. In 1980, silicon was presented as a feasible mechanical material [3]. As to take the advantage of silicon microelectromechanical systems (MEMS) to replace quartz for frequency reference applications, the work started in the early 1990's at UC Berkeley and then continued in early 2000's in Michigan and Georgia Tech. One of the first MEMS oscillators (MOs) was presented which utilized a folded-beam capacitive-comb transduced polysilicon micromechanical resonator [4]. The results created a variety of academic and commercial motivations in the field of MEMS resonator technology, which is gradually gaining popularity as a solution for the integration barrier and high-performance micromachined oscillators and has been presented by researchers and companies [5], [6], [7], [8], [9], [10], [11], [12].

Transduction in MEMS resonator can be done by capacitive or piezoelectric methods. To achieve high Q, capacitive micromechanical resonators should be operated in vacuum to eliminate losses due to fluidic damping (air damping) mechanisms. Also to perform the transduction they need relatively large dc-bias voltage. However, the transduction in thin-film piezoelectric-on-substrate (TPoS) MEMS resonators is performed through a thin film piezoelectric layer actuation located on top of the silicon layer substrate. It has been shown that TPoS resonators can yield superior power handling and Q (in air) due to the excellent power density and low acoustic loss of their silicon resonant body [13], [14]. Moreover, they don't need any dc-bias for transduction. With such advantages, TPoS resonators are posed as great candidates to be employed in low-noise oscillator circuits [15], [16].

Although, MEMS resonators such as TPoS devices have been successfully incorporated in low-power and low-noise oscillators, they have still limited frequency stability versus temperature. one of the most important drawbacks of MEMS resonators has been their relatively large and linear temperature coefficient of frequency (TCF) (e.g. around -30ppm/°C for Si-based [17] and -25ppm/°C for AlN-based resonators [18]). Based on such TCF values, the total frequency drift will be greater than 3700ppm and 3100ppm over -40C to 85C for Si and AlN resonators respectively. This is orders of magnitude larger than what is reported for uncompensated quartz crystals [19] (figure 7-1). Moreover, quartz resonators benefit from a turnover point at which the local TCF is zero. Therefore, very stable quartz oscillators are achievable within the industrial temperature range (-40°C to 85°C) by stabilizing the temperature of an oven-controlled crystal at its turnover point [20].

Also, methods of frequency tuning have not yet been studied extensively for such devices. Knowing these requirements, the focus of this research is on the frequency stability of TPoS oscillator. Particularly, study of the frequency stability of TPoS resonator versus temperature is the subject of this document. In this dissertation two novel temperature compensation techniques are introduced. Additionally, since the phase noise has also a great impact on the frequency stability of the oscillator, research on improving the phase noise and its dependency on the resonator characteristic is also included in this work. Two novel nonlinearity reduction techniques as well as a new frequency tuning method in TPoS resonators are also introduced in this dissertation.

This dissertation consists of 10 chapters. Chapter 1 is an introduction and motivation to the work accomplished in this work. Chapter 2 is a review of the literature on the progress of acoustic resonant devices and particularly their frequency stability. In chapter 3 the thin-film piezoelectric-on-substrate resonator and oscillator technology is overviewed. In chapter 4 the frequency stability and challenges in MEMS oscillators are reviewed and the temperature compensation

methods are discussed. The focus of chapter 5 is nonlinearity reduction in TPoS resonator where two novel methods are discussed. The dependency of TPoS resonator characteristics on short-term frequency stability (jitter and phase noise) of the oscillator is also covered in chapter 6. In chapter 7 a novel technique for temperature compensation in silicon resonators by n-type doping is introduced. Another new technique for temperature compensation in MEMS resonators by using two MEMS sub-oscillators is introduced in chapter 8. The passive tuning in TPoS resonator is also presented in chapter 9 and at the end is chapter 10 which will be the conclusion.

CHAPTER II

REVIEW OF LITERATURE

The piezoelectric effect was discovered by Jacques and Pierre Curie brothers in 1880. They found out that when a mechanical stress is applied on crystals such as tourmaline, topaz, quartz, Rochelle salt and cane sugar, electrical charge, which is proportional to the applied stress, appears on the surface of crystals. For the first time, Paul Langevin, investigated quartz resonators for utilizing in sonar systems during World War I [21]. However, the first crystal-controlled oscillator, using a crystal of Rochelle salt, was built in 1917 and patented in 1918 by Alexander M. Nicholson at Bell Telephone Laboratories [22]. In 1921, Cady built the first quartz crystal oscillator [23]. Since 1921 XOs (quartz crystal oscillators) have been expanded billions of units distributed annually [24].

Crystal oscillators are widely used as the frequency reference in almost all electronic systems because of their excellent performance regarding the quality factor and the temperature frequency stability [25], [26]. Figure 2-1 depicts one example of utilizing XTALs (Crystals) in mobile communication industry [27]. In this mobile phone mainboard there are 5 XTALs: Two 32kHz Xtals for power management and sleep mode, one 33.6 MHz Xtal for GPS application, one 24 MHz Xtal for processor/USB/Audio/Video and one 26MHz Xtal for cellular radio purpose.

As the communication technology progresses, its needs also increase. The clock generator

market as a vital technology is targeted to high frequency and very small size features which is not met by quartz crystals. The integration feasibility is another issue related to quartz, which has not been able to cope with so far.

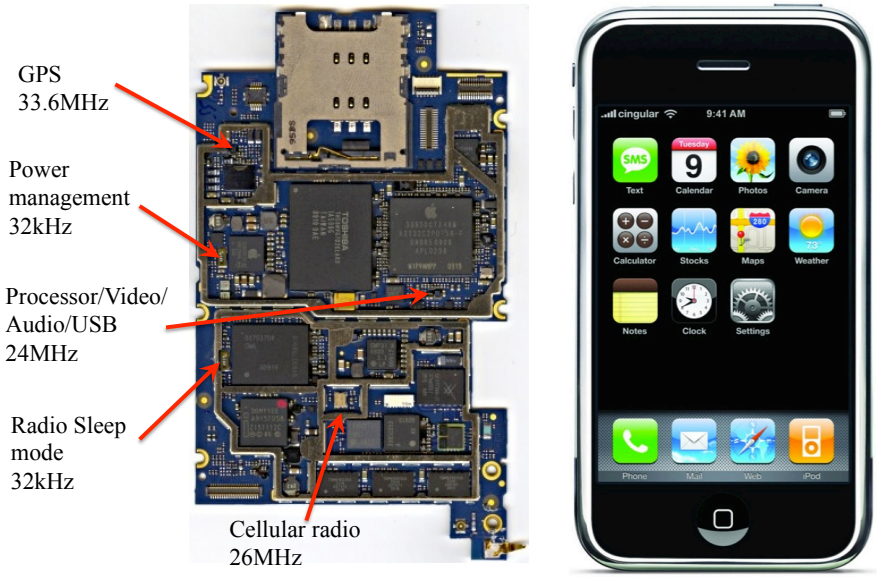

Figure 2-1. XTAL oscillators on iPhone 3GS mainboard [27]

2-1) Accuracy requirement for communication systems

Most of the pros of the quartz oscillator and cons of the silicon technology are associated with the term of "stability", so why does the stability have such an importance?

Generally, the performance of the electronic systems depends on the accuracy and stability of their frequency reference [28]. On the other hand, the frequency spectrum is a limited resource. As the number of users in radio-communication systems increases, channel spacing is narrowed, and higher-frequency spectra should be allocated to meet the demands. Smaller channel spacing and higher frequencies require tighter frequency tolerances for both the transmitters and the receivers. For example, in the past when only a few thousand commercial broadcast transmitters were in use, just 500ppm instability in the frequency was enough. However, today the oscillators

in the millions of cellular telephones operating in high frequency bands (i.e. 900 MHz for GSM900 and 1800MHz for DCS1800) must have a frequency stability of 5ppm and better. The stability requirement also highly depends on the nature of the communication system. For instance, while a mobile station needs the stability better than 5ppm, the base station stability (i.e. BTS in GSM cellular phone) should be even better than 0.1ppm [29]. Some examples of frequency accuracy requirement in commercial wired and wireless data communication systems are shown in figure 2-2.

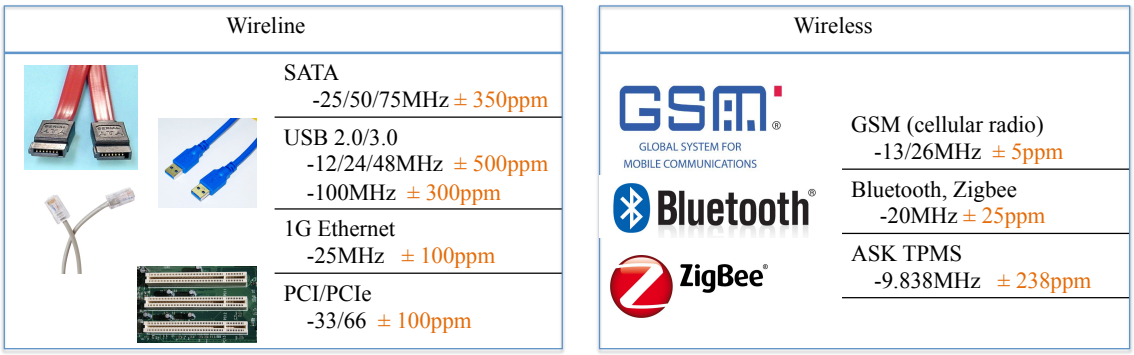

Figure 2-2. Reference frequency and accuracy requirement for wired and wireless data communication

The stability of a frequency reference circuit is a measure of the amount of variation in its output frequency as a function of environmental parameters. These include temperature, supply voltage, process tolerances, noise, etc.

2-2) Temperature dependency of the resonance frequency in quartz resonators

As mentioned, crystal resonator is the most commonly used in data communication, due to its excellent temperature stability and long-term stability. Quartz has different material and mechanical properties such as elasticity, piezoelectricity, and dielectric property according to the different directions of the crystal cut. Therefore, by slicing the quartz at various cuts with respect to its axes, it is possible to obtain a variety of crystal resonators with different temperature

characteristics. For example, as shown in figure 2-3, AT-, BT- and CT- cut quartz resonators operating in thickness shear mode have different frequency-temperature characteristics [19]. The AT-cut quartz resonator has excellent frequency stability over a wide temperature range since its first- and second-order temperature coefficients of frequency (TCF) are zero at room temperature and the frequency-temperature characteristic is only determined by a third-order function of temperature.

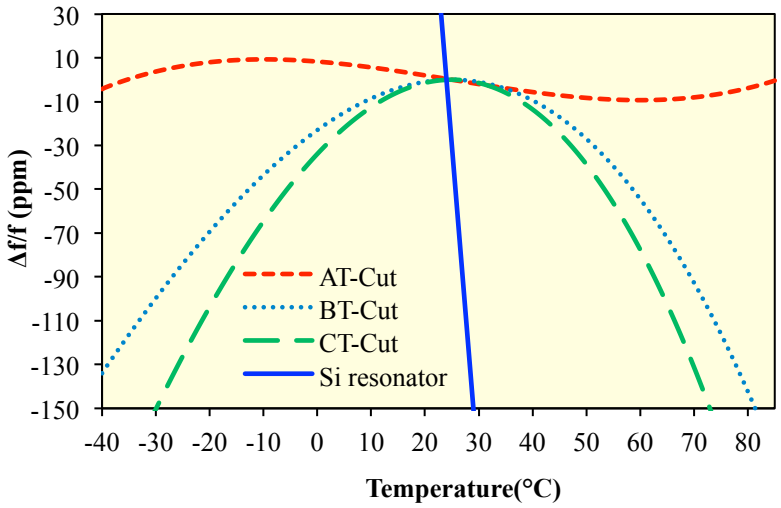

Figure 2-3. The temperature-induced frequency variation plots for different cuts of quartz and typical Si-based resonator

Quartz crystal oscillators are available with various levels of accuracy. The non-compensated (XO) and voltage compensated (VCXO) oscillators achieve stabilities in the range of 20–100 ppm, while for the temperature compensated (TCXO) case, the accuracy is in the 0.1–5 ppm range. Oven controlled (OCXO) oscillators also achieve very high stabilities: in the order of 1 ppb.

2-3) Quarts resonators' drawbacks

Apart from their high levels of accuracy, quartz crystal oscillators have some drawbacks. They occupy significant space on printed circuit boards, especially when a number of frequency sources are required within one system. They are also sensitive to mechanical shock and vibration. Fabrication limitations associated with scaling for high-frequency applications is another disadvantage of quartz crystal resonators. Furthermore, the material property of quartz limits the integration of frequency references circuits and CMOS circuits on a single chip. These drawbacks essentially affect the quartz crystal role in the future very-small-scale technology and as well as in new application.

2-4) Silicon-based MEMS oscillator era

Quartz limitations have motivated the companies and researchers to look for integrated frequency references that can achieve the same level of stability as quartz crystal oscillators. Such references regardless of their stability can be manufactured in silicon, which is why they are also referred to as silicon-based frequency references.

The resonance property of such structures was first researched in 1967, when a resonant gate transistor was presented as a micro-machined integrated frequency reference. This excitation can be of the electrostatic, piezoelectric or electromagnetic type. The resonance characteristics of the resonator such as quality factor (Q) and motional impedance (R_m) mainly determine the stability of the oscillation frequency reference. A MEMS resonator's shape and geometry determines these factors, which are typically in the range of 50,000 and 300,000 for quality factor and 50-1000,000Ω for motional impedance respectively. In terms of Q, this range is comparable to quartz crystal oscillators. In addition, since the lateral dimensions determine the resonance frequency of the MEMS resonators in lateral extensional mode, multiple frequencies can be achieved on a single chip.

In terms of the transduction, MEMS resonators can be driven with either the capacitive or piezoelectric methods. The capacitive transduced resonators using various micromechanical structures, such as cantilever beams or clamped-clamped beams, are driven by parallel-plate capacitive electrostatic forces. The capacitive transduction usually utilizes an electrostatic force across a sub-micron gap (usually smaller than 1 μm) to drive the micromechanical structure and then to sense the motional current. The Q's of the electrostatic resonant structures are very low at atmospheric pressures because of the squeeze-film air damping in a sub-micron air gap, but the Q's can be raised by orders of magnitude in vacuum. However, having a large motional resistance (R_m), makes the oscillator circuit more complicated regarding the necessary gain for oscillation. The impedance matching with other low impedance parts of the circuit is also another important problem.

In piezoelectric-transduced resonators the electrical energy is converted to mechanical energy and vise versa by using piezoelectric materials including but not limited to lithium niobate (LiNbO3), zinc oxide (ZnO), lead zirconium titanate (PZT), AlN. Due to high electromechanical coupling, the motional resistance of this kind of resonators is very low (can be lower than 100Ω). Also since the coupling is not done through capacitive method, this kind of resonators don't need to operate in vacuum, except for low frequency resonators in which the air damping is significant.

Despite their marvelous advantages, MEMS resonators have faced many challenges in delivering a cost-effective and reliable solution that could compete commercially with quartz crystals. The major challenges include the packaging, long-term stability and the frequency drift versus temperature.

2-5) Temperature dependency of the resonance frequency in MEMS resonators

As mentioned, one of the most important drawbacks of MEMS resonators has been their relatively large and linear temperature coefficient of frequency (TCF). The temperature

dependence of MEMS resonators is mainly due to the temperature coefficient of the elastic constants of the resonant body material. Most materials, such as Si, ZnO, and AlN show mechanically spring softening effect when the temperature increases. This means the temperature coefficient of elasticity (TCE) of these materials is negative. For instance, Si MEMS resonators have a first-order TCE of approximately –60 ppm/°C; results in a TCF around -30 ppm/°C [17]. AlN MEMS resonators also show a ~ –50 ppm/°C TCE which results in a TCF around -25 ppm/°C [18]. ZnO MEMS resonators exhibit a TCE and TCF around -120ppm//°C and –60 ppm/°C respectively [30]. Based on such TCF values, the total frequency drift will be greater than 3700ppm and 3100ppm over -40C to 85C for Si and AlN resonators respectively. This is orders of magnitude larger than what is reported for even uncompensated quartz crystals [19] (figure 2-3). Moreover, quartz resonators benefit from a turnover point at which the local TCF is zero. Therefore, very stable quartz oscillators are achievable within the industrial temperature range (-40°C to 85°C) by stabilizing the temperature of an oven-controlled crystal at its turnover point [20].

2-6) Temperature compensation techniques

Having high temperature-induced frequency drift, MEMS oscillators need temperature compensation in order to meet the stability criteria of specific application. There have been various structural and circuit-level techniques attempted through active and passive to reduce or correct the temperature coefficient MEMS resonators.

2-6-1) Passive Temperature Compensation

Although, aforesaid MEMS materials have negative TCE, there are some materials showing a positive TCE. For example, an amorphous SiO2 layer shows positive TCF [12], [17], [31], [32], [33]. Therefore, one possible passive method for temperature compensation will be the usage of a compensating layer of SiO2 in the composite of materials as the resonant body of the resonator.

This technique has been widely applied to various Si-based electrostatic MEMS resonators and piezoelectric resonators. By depositing a compensating thin film with an appropriate thickness, the first-order TCF can be reduced to zero at a specific temperature. However, the second-order TCF of the composite still depends on the temperature after passive temperature compensation. Another technique is temperature compensation through degenerate doping of silicon [34].

2-6-2) Active Temperature Compensation

Although AT- and ST-cut quartz resonators and temperature-compensated MEMS resonators can offer temperature stability lower than 100 ppm, it is still not enough for some reference oscillator applications (Table 1). Therefore, an additional temperature compensation technique is needed to achieve better frequency stability. One approach is to apply an electrostatic force to (in capacitive resonators) or passing a DC current through the resonator body to adjust the resonance frequency by spring softening effect. Another approach is to use a temperature sensor to detect the temperature changes and a compensation circuitry to pull up the oscillation frequency (for example, using a varactor shunt), for minimizing the temperature-induced frequency drift (named TCXO in quartz oscillators). As shown in figure 2–4, TCXO technique is done through shifting the resonance frequency by adjusting the effective capacitance via applying a voltage to a varactor diode. TCXO normally can offer excellent temperature stability with low power consumption and fast stabilization time.

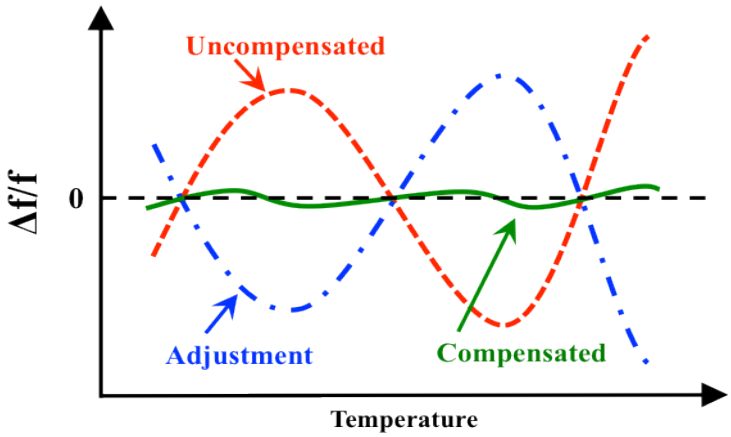

Figure 2-4. Concept of active temperature compensation in TCXO oscillators [29]

In order to achieve a better degree of stability, a more complicated circuitry is implemented in microcomputer compensated crystal oscillators (MCXOs). Also the micro-resonator can be placed in a thermally isolated micro-oven and stability is achieved by regulating the temperature (OCXOs) [35], which is typically used for the highest precision frequency applications.

Although these techniques are successful in demonstrating very low temperature-induced frequency drift, they add complexity to the fabrication process, increase power consumption or fail to offer a local zero TCF.

CHAPTER III

TPOS TECHNOLOGY

3-1) Introduction to TPoS technology

Thin-film piezoelectric-on-substrate (TPoS) technology was introduced for the first time at Integrated MEMS lab in the Georgia Institute of Technology in 2003 [36]. A TPoS resonator consists of a thin piezoelectric film (e.g. Aluminum Nitride, AlN) sandwiched between two metal electrodes (e.g. molybdenum, Mo) stacked on top of the device layer of a silicon-on-insulator (SOI) substrate (as shown in the schematic of figure 3-1) [13]. The bottom Mo is patterned to reduce the parasitic capacitor of the input and output traces. The top and bottom Mo are dry etched in SF6 and O_2 plasma to form the top electrodes and the traces while the AlN is wet etched to clear access to the bottom electrode. The resonator body is defined in a plasma-etching step. The backside handle layer silicon is etched in a deep reactive ion-etching chamber, which creates the cavity below the resonator. The final release step is done in buffered oxide etch (BOE) solution to remove the buried silicon dioxide layer and create the freestanding structure (figure 3-2). TPoS resonators can be designed in either one-port or two-port configurations. In a two-port design (figure 3-1) usually one port is used to excite the resonance and the second port is used to sense the vibration. The electrode pattern is designed to yield a minimum series impedance (maximum output current) at the mode-shape of interest. For example the pattern of figure 3-1 can be used for both fundamental and the third harmonic bulk width-extensional modes of the

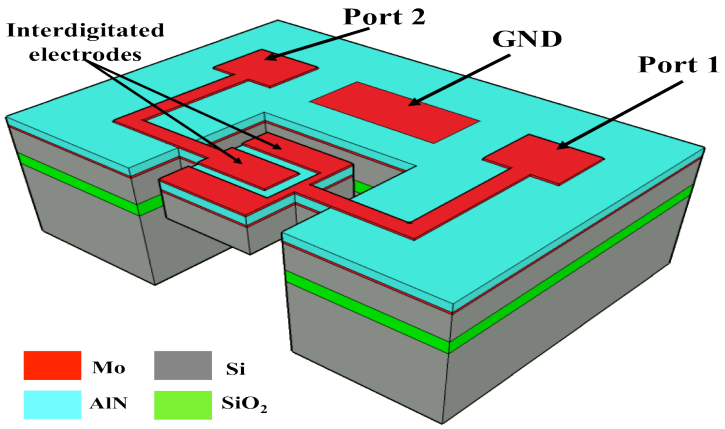

Figure 3-1. The schematic of a 27MHz TPoS resonator

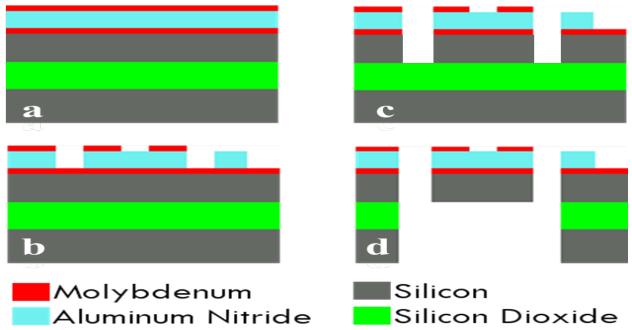

Figure 3-2. Process flow; a) a stack of Mo, AlN, and Mo is sputtered on top of the single crystalline silicon device layer of a SOI wafer. b) the top Mo layer is dry etched to form the top electrodes. Access to the bottom electrode is then gained through a wet etch of the AlN. c) The resonator body is then defined with a series of dry etches through the AlN/Mo and then through the device layer silicon. d) The handle-layer silicon is etched from the backside using a DRIE process. Finally, the structure is released with a buffered oxide etch of the buried silicon dioxide layer.

structure.

3-2) TPoS technology characteristics

Using the TPoS technology it has been successfully demonstrated a very high quality factor, low motional impedance, and high power handling in air [37], [38]. A frequency response of an optimized fundamental-mode TPoS resonator similar to the schematic picture of figure 3-1 and designed for operation at 27MHz is shown in figure 3-3. The combination of 44500 unloaded quality factor and 200Ω motional impedance in air as demonstrated in this figure is a unique

feature not reported by other technologies. Also, there are no significant spurious resonance peaks in the vicinity of the main peak as captured in the 20MHz span of figure 3-3.

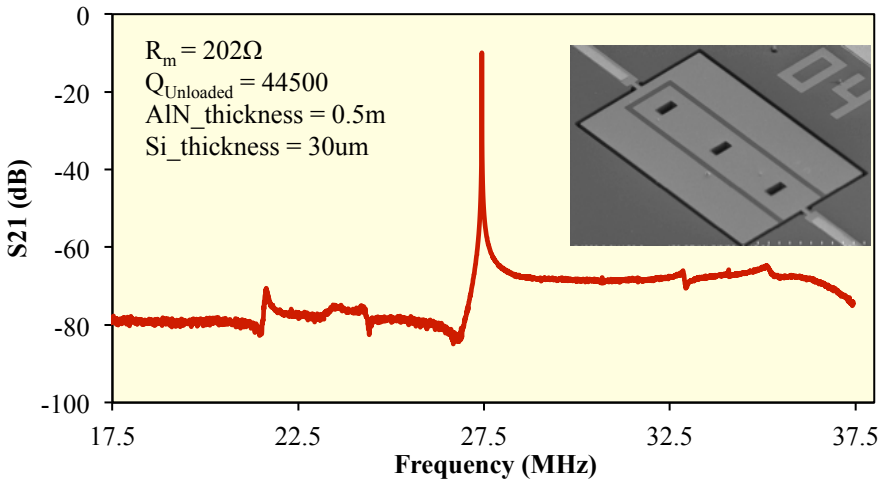

Figure 3-3. Frequency response of a typical 27MHz TPoS resonator in air

Also by taking advantage of higher order designs (as shown in the schematic of figure 3-4) benefits such as larger transduction area which results in lower motional impedance, reducing the spurious modes and consequently improving the Quality factor [39], [38], and higher power handling are achieved by this technology [14]. The frequency response as well as SEM picture of a typical 1GHz higher order mode TPoS resonator, which poses the Q around 7100 and motional impedance almost 150 Ω are shown in figure 3-5.

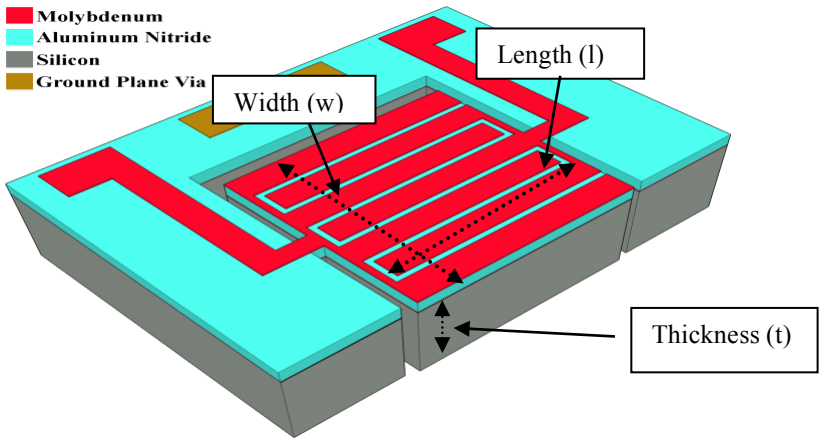

Figure 3-4. The schematic of a 7th order TPoS resonator

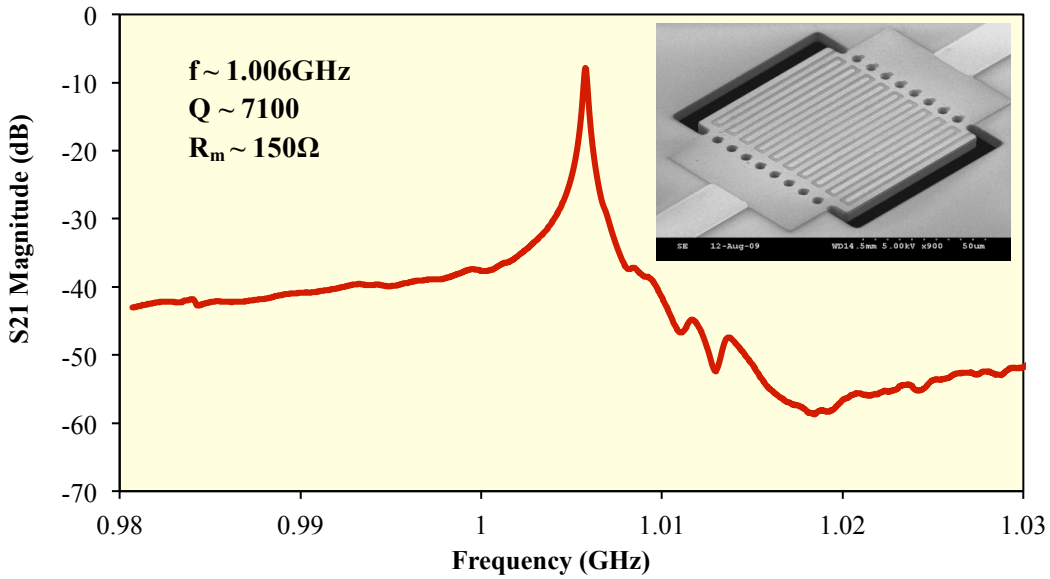

Figure 3-5. The frequency response of a typical higher order mode TPoS resonator in air

Since the electromechanical transduction is done by piezoelectric mechanism in piezoelectric resonators, in contrary with the capacitive transduction resonators, the air squeeze film damping is very small compared to capacitive resonators, particularly at high frequency where the vibration amplitude is less than in lower frequency resonators. This phenomenon makes the piezoelectric transduction resonators have excellent performance in air. However, they have to operate in a kind of vacuum level ambient to prevent the condensation in low ambient temperature, which affects the resonator performance. Measured quality factor and resonance frequency versus the ambient pressure in the range of 0.01 Torr to atmosphere are shown in figures 3-6 and 3-7 respectively. As seen from figure 3-6 and 3-7, in contrary to capacitive resonator, the performance of the TPoS resonators has not significant degradation up to the pressure of ~10 Torr (less than %2 reduction in quality factor and less than 20ppm in the resonance frequency) which lowers the vacuum cost compared to the capacitive resonators.

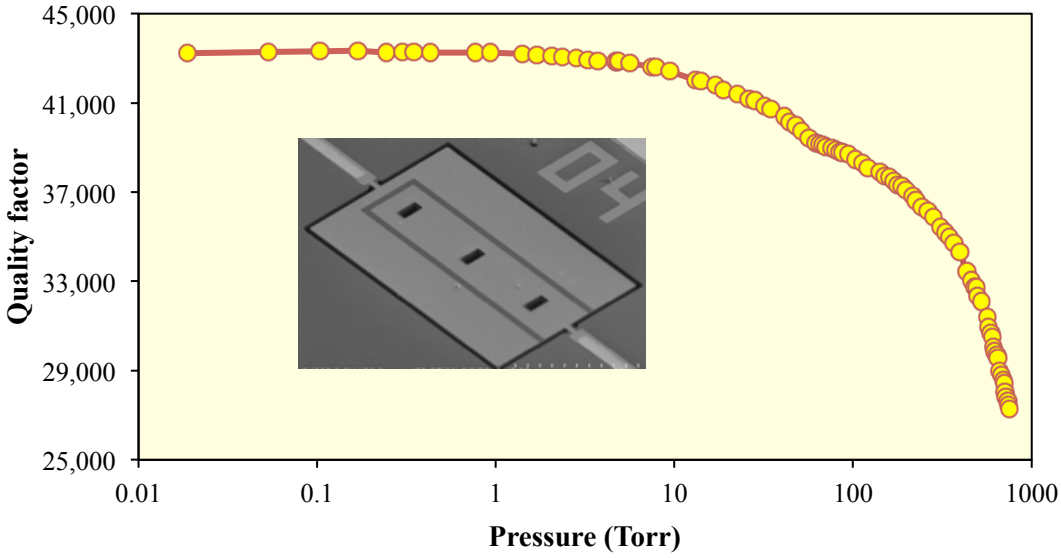

Figure 3-6. Quality factor versus pressure of a typical 1st mode 27MHz TPoS resonator

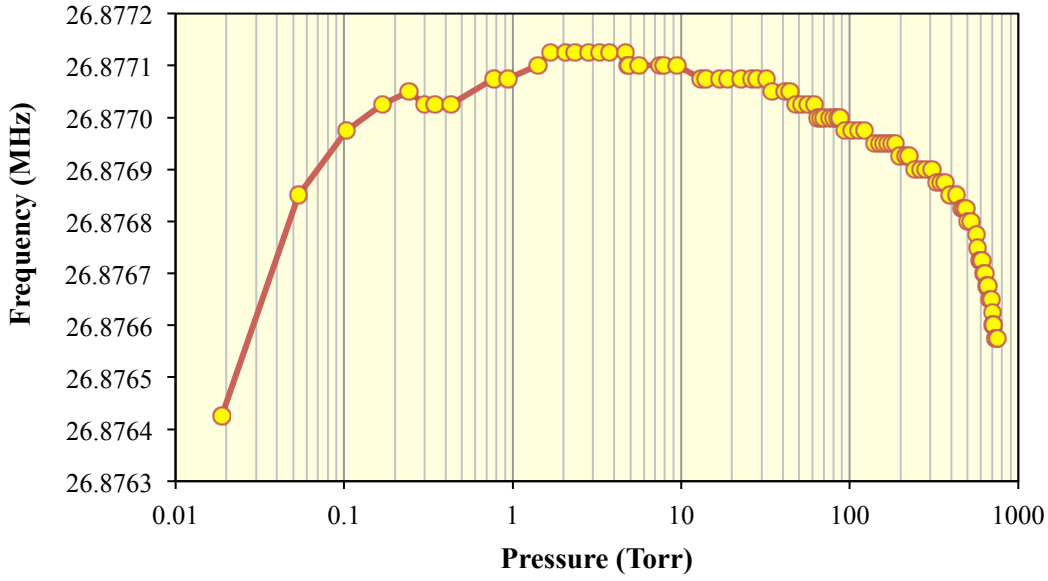

Figure 3-7. Resonance versus pressure of a typical 1st mode 27MHz TPoS resonator

CHAPTER IV

FREQUENCY STABILITY IN MEMS OSCILLATORS

Even though an oscillator is designed to operate at a specific frequency, its oscillation frequency is not sustained during the operation. Stability shows how good an oscillator can generate the same time or frequency over a specific time interval. The term “frequency stability” is defined as the ability of the oscillator to preserve a single fixed frequency over a time interval. The oscillation frequency changes either in a uniform manner or sometimes in a random fashion.

4-1) Frequency instability factors

The required output of an oscillator circuit is a well-stabilized frequency, which is determined by the resonance frequency of the resonator. The resonator frequency, yet, is determined by the geometry (e.g. width in lateral extensional mode, or thickness in thickness mode) and material properties such as density and elasticity. Since these features are influenced by time, temperature changes, and other environmental conditions such as shock, gravity, force [40], supply voltages, stray capacitances, output load etc., it is expected that these factors will influence the resonator oscillator frequency.

4-2) Time dependency

Frequency variations relative to time are indicative of oscillator stability. Stability is usually expressed as the fractional frequency change over a period of time, i.e., long-term or short-term.

4-2-1) Short-term instability (noise)

Short-term instability is fast changes in oscillator frequency over the time. Short-term frequency variations or time domain stability is a measure of the frequency or phase noise [41]. This is specified as the standard deviation of the fractional frequency variations for a specific averaging time. Short-term instability usually refers to variations over intervals less than 100s [42].

4-2-2) Long-term instability (aging)

Long-term instability is slow changes in oscillator frequency over the time [43][44] and can refer to measurement intervals greater than 100s, however, usually it refers to intervals longer than 1 day.

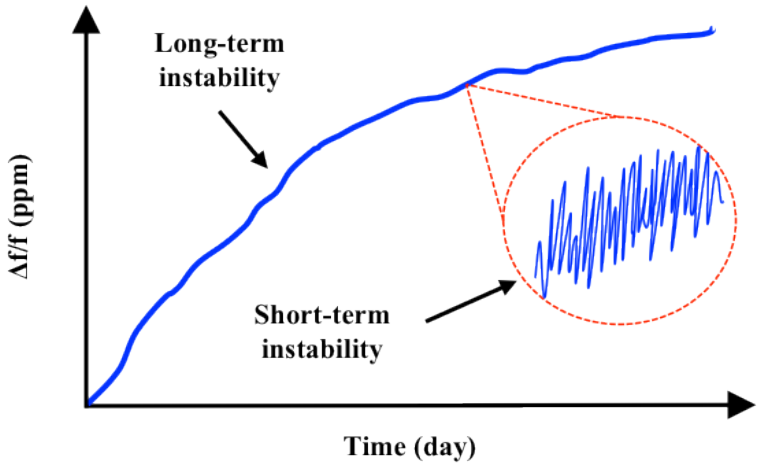

Figure 4-1. Short-term and long-term instability explanation [45]

4-3) Temperature dependency

The resonance frequency of a resonator is determined by its material properties as well as its geometry shape. Since the temperature influences these factors, the resonance frequency of the resonator is changed over the variations in temperature.

4-4) Other factors

Other environmental conditions such as shock, gravity, force, supply voltages, stray capacitances, output load etc. influence the oscillation frequency.

CHAPTER V

NONLINEARITY REDUCTION IN TPOS RESONATORS

The MEMS resonators typically have a much lower power handling capability than that of a traditional macro-resonator due to their relatively small size. As the power applied to a high-Q MEMS resonator increases, the device is driven to its nonlinear operation region, which can consequently limit the lowest noise-floor achievable using the device in an oscillation loop and can potentially affect the system level performance of the host electronic device.

Therefore, it is of great importance to understand the nature and the limits of the nonlinearity in MEMS resonant devices. Nonlinearity in resonators can be modeled using amplitude-dependent higher order terms of the material stiffness [46].

In the past, nonlinearity reduction has been engineered in flexural-mode electrostatic resonators through manipulating the amplitude-dependent stiffness terms with opposing signs, resulted from combined mechanical properties and the electrostatic transduction in capacitive resonators [47], [48], [49]. The nonlinearity due to nonlinear spring effects can also be reduced by modifying the electrode shapes or reducing the bias voltage [50]. However, capacitive coupling causes nonlinearity by producing harmonics in the motional current independent of the vibration amplitude.

TPoS resonators (a schematic representation of a TPoS resonator is presented in Figure 3-1) show superior power handling capabilities due to the large energy density that can be stored in their silicon resonant body and have shown great potential for low power and low noise oscillator applications [13], [37]. In order to further improve the near-carrier phase noise of oscillators based on TPoS resonators, the quality factor must be improved by design optimizations. For example, a TPoS resonator with unloaded Q of ~45000 at 27MHz with ~200Ω motional impedance has been already designed and reported [51]. However, the power handling and linearity of a resonator is generally compromised as the Q increases [37], which can potentially limit the noise-floor [5].

The nonlinearity in thin-film piezoelectric-on-substrate (TPoS) is dominated by the mechanical spring effect [37] and is mainly a function of the mechanical properties of silicon. It has been shown that the extensional TPoS resonators fabricated on lightly silicon substrate exhibit spring softening as they are driven by larger input powers [14].

In this chapter, two new methods for nonlinearity reduction in TPoS resonators are introduced. It is demonstrated that the nonlinearity reduction in TPoS resonators can be achieved by modifying the doping concentration and aligning the resonator to the [100] crystalline orientation. Also it can be improved by designing high-order harmonic resonant structures anchored with multiple tethers.

5-1) Nonlinearity in Micromachined resonators

Phase noise is a critical measure of the frequency stability in oscillators. Leeson's model predicts the phase noise-to-carrier ratio in an ideal oscillator as [52]:

$$L(\Delta\omega) = 10log\left[\frac{2FkT}{P_0}\left(1+\left(\frac{\omega_0}{2Q\Delta\omega}\right)^2\right)\left(1+\frac{\Delta\omega_{1/f^3}}{|\Delta\omega|}\right)\right] \quad (5\text{-}1)$$

where ω_0 is the carrier frequency, $\Delta\omega$ is the frequency offset, Q is the quality factor, P_0 is the oscillation power, k is the Boltzmann constant, T is the equivalent noise temperature and F is an empirical fitting parameter. As seen in (5-1), quality factor and oscillation power affect the phase noise. Phase noise is diminished as P_0 increases. However, the maximum P_0 that can be reached at bifurcation point decreases as the Q increases. Therefore, presuming all other parameters remain unchanged, a larger Q can limit the noise floor.

Mechanical nonlinearity in lateral-extensional TPoS resonators can be described by nonlinear engineering Young's modulus which depends on engineering strain as in (5-2):

$$Y(S) = Y_0(1 + Y_1 S + Y_2 S^2 + \cdots) \tag{5-2}$$

Engineering strain results in the nonlinear spring constant, $k(x) = k_0(1 + k_1 x + k_2 x^2 + \cdots)$, where k_1 and k_2 are the first and second order anharmonic terms and x is the vibration amplitude. The introduction of these coefficients captures the nonlinear behavior of the device and their magnitudes and polarities predicts the shift in the resonance peak either toward lower frequencies (softening) or higher frequencies (hardening) based on the sign of κ in (5-3) (as shown in figure 5-1):

$$\omega_0' = \omega_0(1 + \kappa x^2) \tag{5-3}$$

where, $\kappa = \frac{3}{8}k_2 - \frac{5}{12}k_1^2$ [46].

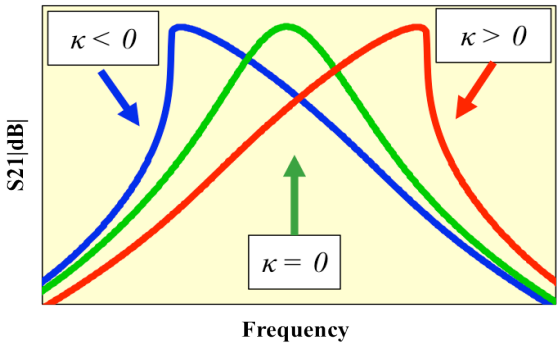

Figure 5-1. Frequency response of a resonator in linear, spring softening and spring hardening region

On the other hand, the energy stored in the device reaches its maximum when the device is pushed to hysteresis [50]:

$$E_{stored}^{max} = \frac{1}{2} k X_c^2 \quad (5\text{-}4)$$

where k is the mechanical spring stiffness and X_c is the maximum (critical) vibration amplitude at the bifurcation point. Therefore, the maximum energy stored in the device is proportional to the stiffness constant and square of the maximum vibration amplitude, X_c. In lateral-extensional fundamental mode devices, k and X_c are proportional to thickness, length, width, and quality factor as:

$$k \sim \frac{t \cdot l}{w} \quad and \quad X_c \sim \frac{w}{\sqrt{Q}} \text{ [1]} \quad (5\text{-}5)$$

where t, l, w are thickness, length, and width of the device respectively (Figure 3-1). Therefore (using equation 5-4):

$$E_{stored}^{max} \sim \frac{t \cdot l \cdot w}{Q} \quad (5\text{-}6)$$

As illustrated above, the maximum energy stored in the device is inversely proportional to the quality factor. Finally, it can be shown that the oscillation power can be written as $P_0=\omega_0.E_{stored}/Q$. In summary, power delivered to the device at X_c determines the maximum energy stored in the device before it runs into hysteresis and represents an inherent trade-off between the oscillator noise-floor and the resonator Q.

5-2) Nonlinearity reduction in silicon resonators through multi-tether high-order design

In this section it is demonstrated that quality factor (Q) and power handling, two inherently divergent characteristics of a resonator, can be improved simultaneously by designing high-order harmonic resonant structures anchored with multiple tethers by adding support tethers at the modal nodes along the width of the resonant body. These designs guarantee higher oscillation

power and consequently higher signal-to-noise ratio, hence they are suitable for implementation of high frequency low noise oscillators [8].

5-2-1) Resonator design

A schematic of a multi-tether high-order design TPoS resonator is shown in figure 5-2. The fabrication is the same as in section 3-1 and figure 3-2.

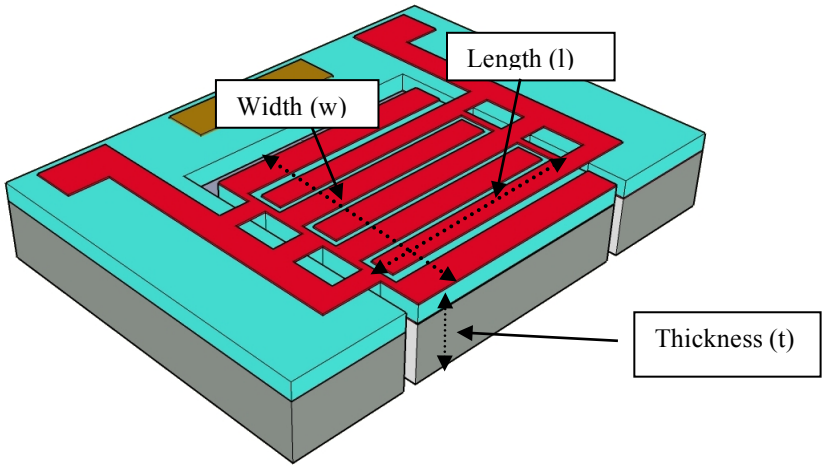

Figure 5-2. The schematic for a 7th order TPoS device with three pairs of support tethers

In order to study the effects of the quality factor on nonlinearity, identical 27MHz designs were fabricated on 20μm and 30μm SOI substrate thick wafers. In addition, two 7th order 400MHz and three 21st order 1GHz resonators were designed on a 5 μm thick SOI wafer with various numbers of tether-pairs. As seen in the 400MHz design in figure 5-2, the resonators were configured with two-port interdigitated electrodes to excite a high-order lateral-extensional mode and were oriented with the width axis aligned to the [110] direction. SEM images of fabricated 1GHz resonators are shown in figure 5-3.

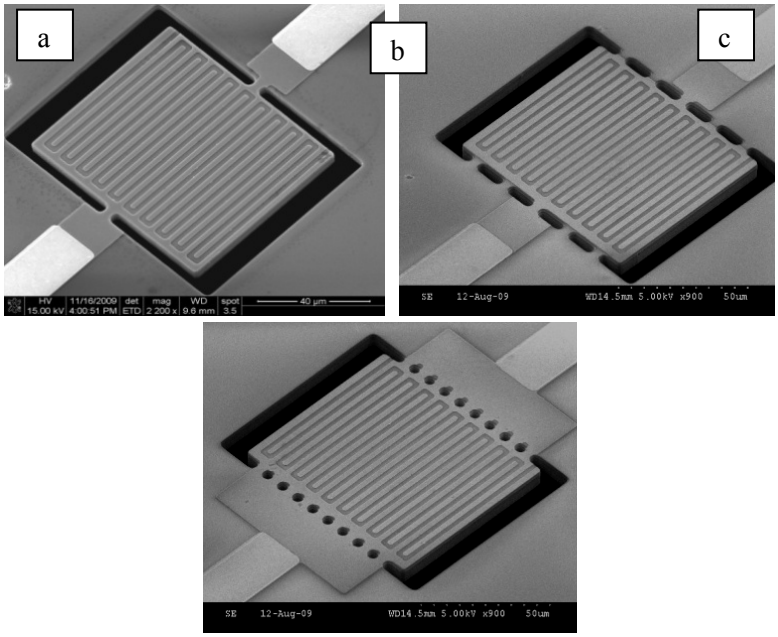

Figure 5-3. Fabricated 1GHz resonators with a) One pair b) Five pairs and c) Nine pairs of support tethers

5-2-2) Nonlinearity measurement setup

In order to study the effects of design parameters on the power handling capabilities of the resonator the power delivered to the devices must be estimated. This is necessary since the delivered power is not only dependent on the output power setting of the measurement tool (i.e. network analyzer) but also depends on the impedance of the device under test. Figure 5-4 lays out the test setup used to measure the nonlinearity effect. After measuring the transmission loss using an Agilent E8358A PNA Network Analyzer, the motional impedance and the power delivered to the device can be approximated as follows:

$$R_m = (R_{in} + R_{out}).\left(10^{\frac{-loss(dB)}{20}} - 1\right) \quad (\Omega) \tag{5-7}$$

$$Power\ delivered = \left(\frac{V_{in}}{R_m + R_{in} + R_{out}}\right)^2 \times R_m \quad (W) \tag{5-8}$$

where R_{in} and R_{out} are the network analyzer's termination impedances, nominally 50 Ω in this setup.

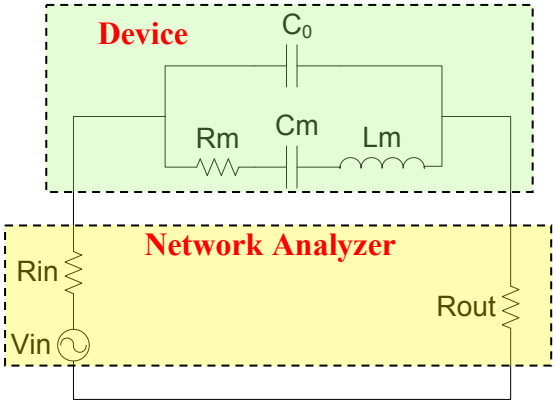

Figure 5-4. The nonlinearity measurement setup

In TPoS resonator, as the power delivered to the resonator increases, the frequency response shows a nonlinear behavior and the resonance peak frequency shifts toward the lower frequencies (Figure 5-5). In order to characterize the resonator response at different power a normalized frequency shift define as:

$$S_N = \frac{(f_c - f_s)}{f_c} \tag{5-9}$$

where S_N is a measure of relative peak frequency shift as the vibration amplitude is altered and is calculated as the difference between the shifted peak frequency (f_s) and the center frequency (f_c) at linear operation divided by f_c (figure 5-4). Therefore, S_N is zero when the peak is perfectly symmetric.

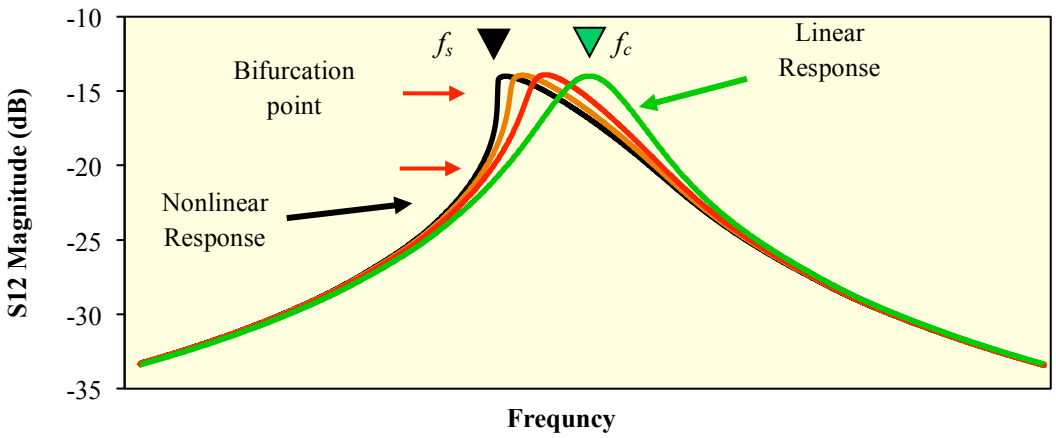

Figure 5-5. Frequency response of a typical TPoS resonator at different delivered power

5-2-3) Measurements

5-2-3-1) Effect of the device thickness on Q and power handling

Fabricated 27MHz devices on 30µm and 20µm thick SOI exhibit a maximum unloaded Q of 27200 and 11200 respectively as seen in figure 5-6. To find the resonators' critical displacement point, the power output from the network analyzer was swept from -15dBm to +15dBm. As shown in figure 5-7, the 30µm device exhibits a linear shape at low power settings but as the power increases the device is driven into nonlinearity. Furthermore, as the resonator is pushed into hysteresis, the forward and backward frequency sweeps no longer match. Through this method the critical applied power at bifurcation point is identified and the power delivered to the device was then calculated using (5-8).

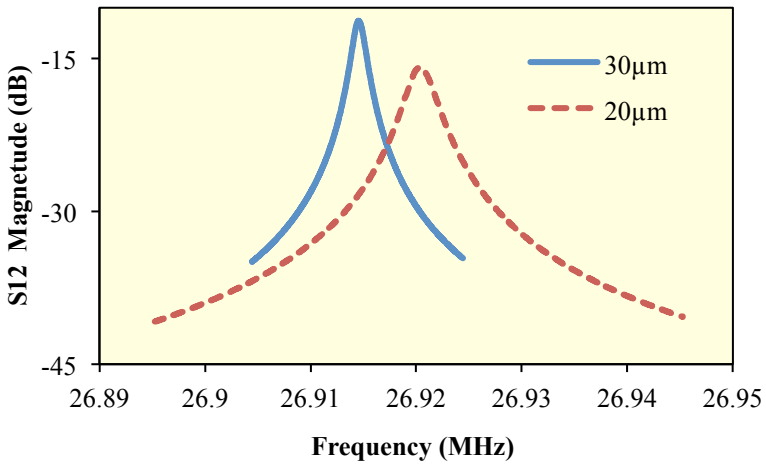

Figure 5-6. The comparison of frequency responses of the 27MHz resonators fabricated on 20 and 30µm substrates

The power handling was then compared between the two 27MHz devices. As shown in figure 5-8, S_N for the high-Q 30µm device is consistently higher than that of the low-Q device for the same power delivered. Clearly, the high-Q device becomes nonlinear at a lower delivered power and consequently, the maximum stored energy in the high-Q resonator is smaller than the low-Q resonator. Furthermore, the critical vibration amplitude, Xc, occurs at 2.53dBm for the low-Q device and -0.29dBm for the high-Q device resulting in 1.92 times greater delivered power before the device exhibits hysteresis. Using (5-6), the device thickness and the measured Q, the theoretical change in delivered power as the thickness decreases from 30µm and 20µm is calculated to be 1.62, a 30% difference from the experimental values. In summary, increasing the thickness by 34% improves the Q by a factor of nearly 2.5, but this gain compromises the power handling of the device.

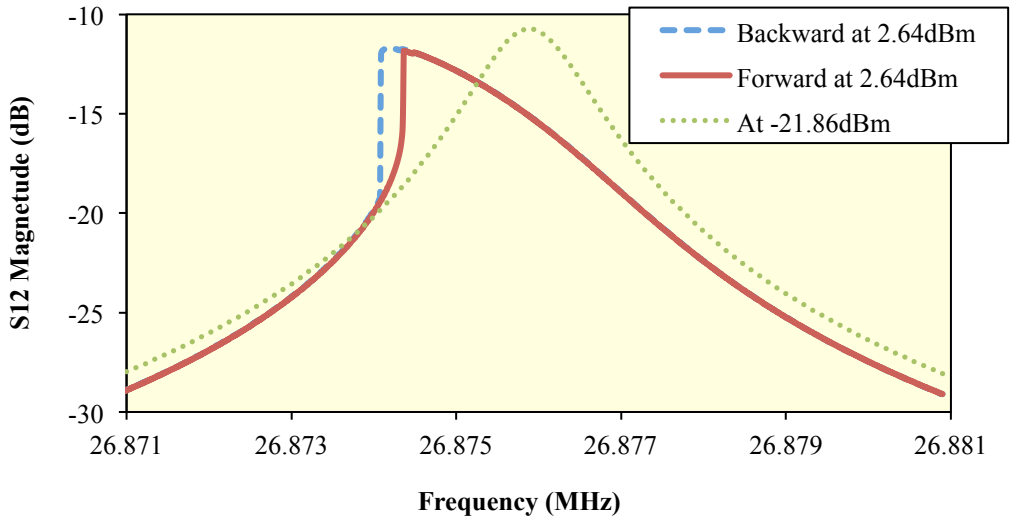

Figure 5-7. Frequency response of a 27MHz resonator at -21.86dBm (no hysteresis) and 2.64dBm (with hysteresis)

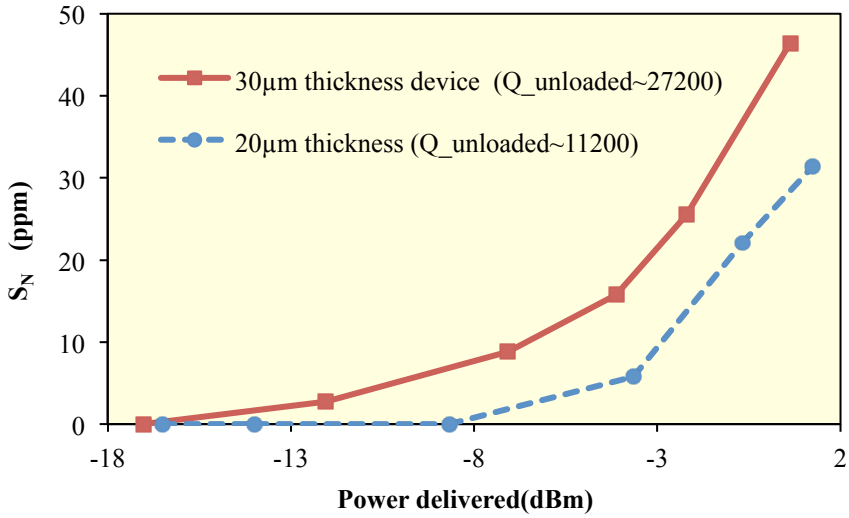

Figure 5-8. The normalized frequency shift (S_N) as a function of delivered power for 27MHz designs on 20µm and 30µm substrate

5-2-3-2) Effect of the number of supports on Q and power handling

In an effort to circumvent Q-linearity-tradeoff, 400MHz devices with one pair and two pairs of support tethers on a 5µm SOI wafer were examined. With the addition of the second pair of support tethers, the Q improves from 3500 to 4200. Although the resonators with two supports

exhibit 20% higher Q, the delivered power to the device at X_c also increases. On the device with one pair of support tethers, X_c occurs at 4.31dBm while the device with two pairs of support tethers withstands up to 6.06dBm, an increase of 1.75dBm. As highlighted in figure 5-9, the nonlinearity effect described by S_N is less for the resonator with two pairs of support tethers than that of the resonator with one pair of support tethers.

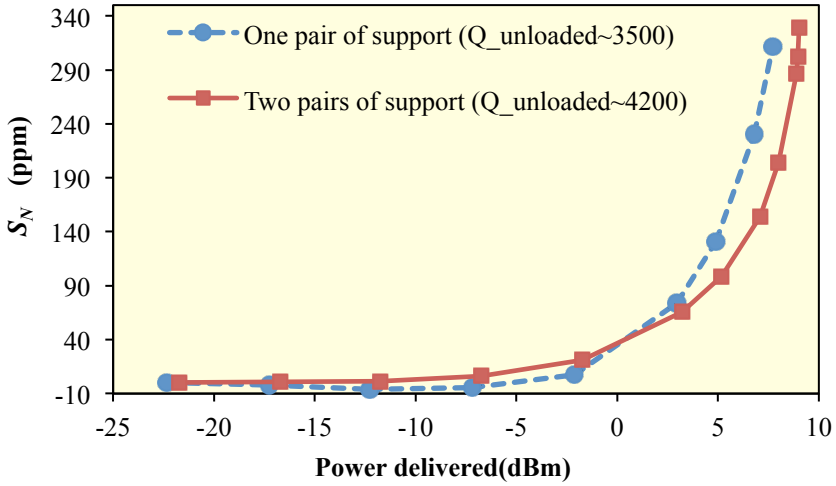

Figure 5-9. The normalized frequency shift (S_N) as a function of delivered power for 410MHz designs on 5µm SOI wafer

Likewise, 1GHz resonator designs with one, five, and nine pairs of support tethers were fabricated on a 5µm SOI wafer to further examine the dynamic between Q and power handling. The highest recorded quality factor increases as more supports are added with 4400 for one pair, 4800 for five pairs, and 6800 for nine pairs resulting in an overall increase of 55%. Xc occurs at delivered power levels of 1.91dBm, 6.78dBm and 7.09dBm for one pair, five pairs, and nine pairs of support tethers respectively. The S_N comparison for the three resonators is displayed in figure 5-10. These results further confirm the concurrence of Q and linearity enhancement using the multiple support tethers. With a 5.20dBm improvement as we move from one pair to nine pairs of support tethers, the maximum delivered power prior to hysteresis is 3.3 times greater (figure 5-11).

This is a very unique situation where the same resonator with different support configurations shows an increase in both Q and linearity. It is believed that adding support tethers to the resonant body will increase the stiffness at modal nodes along the device width. The resulting effect constrains the displacement amplitudes and reduces the strain at these points, which keeps the device elasticity in the linear regime.

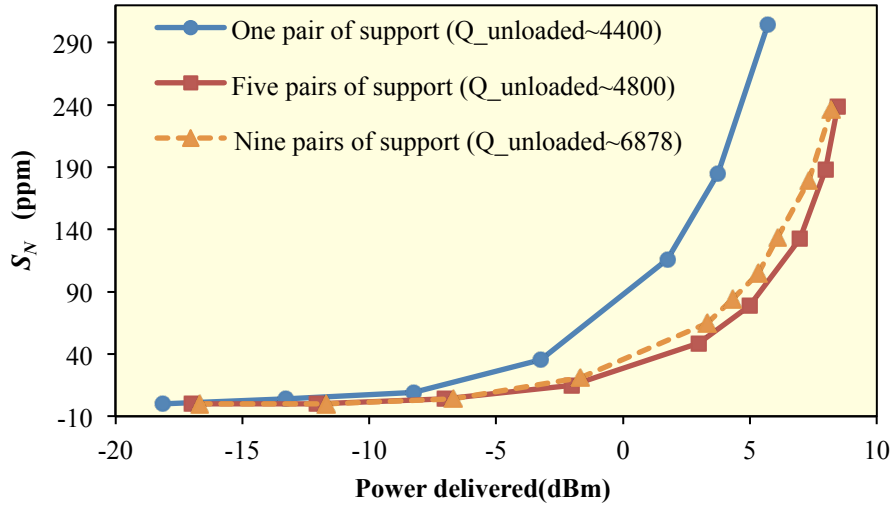

Figure 5-10. The normalized frequency shift (S_N) as a function of delivered power for 1GHz designs on 5µm SOI wafer

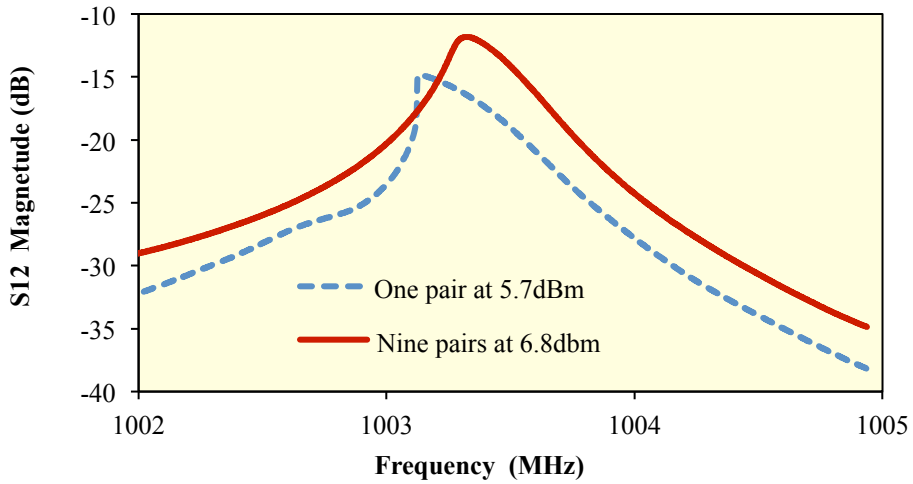

Figure 5-11. Frequency response of 1 GHz devices with one pair and nine pairs of supports at different power delivered

5-3) Nonlinearity reduction in silicon resonators by doping and re-orientation

In this section it is shown that nonlinearity in n-type doped silicon micro-resonators can be reduced by modifying the doping concentration and the resonator alignment to a different crystalline orientation. Spring hardening, a trend opposite to the commonly observed spring softening, is demonstrated in extensional resonators fabricated on a highly Phosphorus-doped ($N\sim5\times10^{19}cm^{-3}$) silicon substrate and oriented in the [100] direction. Therefore, it is hypothesized that for a specific level of doping concentration the nonlinear stiffness coefficients (k_1 and k_2) can be canceled and the device will behave linearly for a large range of input power. It is observed that devices fabricated on an Arsenic-doped substrate with lower doping concentration ($N\sim3\times10^{19}cm^{-3}$) mechanically fail before they reach bifurcation, a preliminary proof for our hypothesis.

5-3-1) The effect of N-type doping on the nonlinearity

The first and second order anharmonic terms, k_1 and k_2, depend on the resonator orientation and the second order, c_{11}, c_{12}, c_{44} and third-order elastic constants c_{111}, c_{112}, c_{123}, c_{144}, c_{166}, c_{456} [53]. These elastic constants of silicon are affected by doping [54], [55].

In the case of n-type silicon, the contribution of free electrons on the elastic constants is calculated as [55]:

$$\delta c_{11} = -\frac{2}{9} N \frac{\Xi_u^2}{E_f} X,\ \delta c_{12} = \frac{1}{9} N \frac{\Xi_u^2}{E_f} X,\quad \delta c_{44} = 0$$

$$\delta c_{111} = \frac{2}{9} N \frac{\Xi_u^3}{3E_f^2} Z,\ \delta c_{112} = -\frac{1}{9} N \frac{\Xi_u^3}{3E_f^2} Z,\ \delta c_{123} = \frac{2}{9} N \frac{\Xi_u^3}{3E_f^2} Z$$

$$\delta c_{144} = 0,\ \delta c_{166} = 0,\quad and\ \delta c_{456} = 0 \qquad (5\text{-}10)$$

where N is the electron concentration, Ξ_u is the uniaxial deformation potential constant and X and Z are defined as:

$$X = \eta F_{1/2}^{'}(\eta) / F_{1/2}(\eta) \ , \quad Z = \eta^2 F_{1/2}^{''}(\eta) / F_{1/2}(\eta) \tag{5-11}$$

where F is the Fermi integral, η is E_f/kT, *and* E_f is the Fermi energy relative to the band edge.

Using (6-3), the contribution of doping levels on the elastic constants, c_{11}, c_{12}, c_{44}, c_{111}, c_{112}, c_{123}, c_{144}, c_{166}, and c_{456} can be calculated. These values could then be utilized to compute the nonlinear engineering Young's modulus and the nonlinear spring constants, k_1 and k_2, versus doping level for different crystalline orientations. It is predicted that κ (equation 6-2) is negative for lightly doped [110]- and [100]-oriented silicon resonators which results in spring softening effect. We will show that, κ is also negative for highly doped [110]-oriented silicon resonators while it changes polarity for highly doped [100]-oriented silicon resonators (spring hardening effect).

5-3-2) Design and fabrication

To show the effect of doping concentration and alignment to different crystalline planes on nonlinearity, resonators were fabricated on a 10µm lightly Boron doped (B-Doped) (N~1×10^{16}cm^{-3}), a 15µm highly B-doped (N~1×10^{20}cm^{-3}), an 8µm highly Phosphorus-doped (P-doped) (N~5×10^{19}cm^{-3}), and a 15µm highly Arsenic-doped (As-doped) (N~3×10^{19}cm^{-3}) SOI wafer (Table 5-1).

Table 5-1. The device silicon properties for the utilized SOI wafers.

Thickness (µm)	**Dopant**	**Resistivity (Ω cm)**	**Doping Concentration (cm^{-3})**
10	Boron	~1.45	~1×10^{16}
15	Boron	~0.001	~1×10^{20}
8	Phosphorus	~0.0015	~5×10^{19}
15	Arsenic	~0.0024	~3×10^{19}

Similar resonators are fabricated on each of these wafers aligned to two different crystalline planes; [110] and [100]. Note that the starting substrate in all of our experiments is [100] SOI

wafers. Therefore, resonators aligned to the wafer flat are oriented in the [110] plane. By rotating the resonator 45° in-plane the device will be aligned to [100] plane (figure 5-12). A 0.5μm film of sputtered AlN is sandwiched between two metal layers and stacked on top of the SOI substrate. The lateral-extensional mode TPoS resonators are fabricated with a five-mask process. The process flow is the same as in figure 3-2. The fabricated [110]- and [100]-oriented resonators at 27MHz and 500MHz are shown figure 5-13.

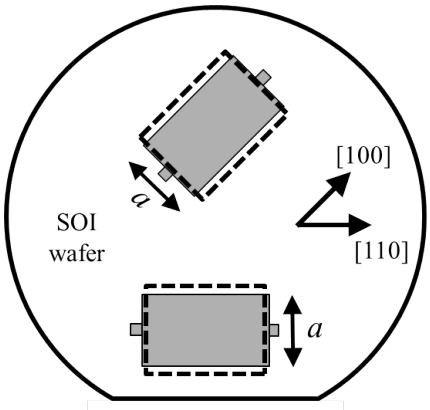

Figure 5-12. The schematic of [110]- and [100]-oriented TPoS designs in SOI wafer

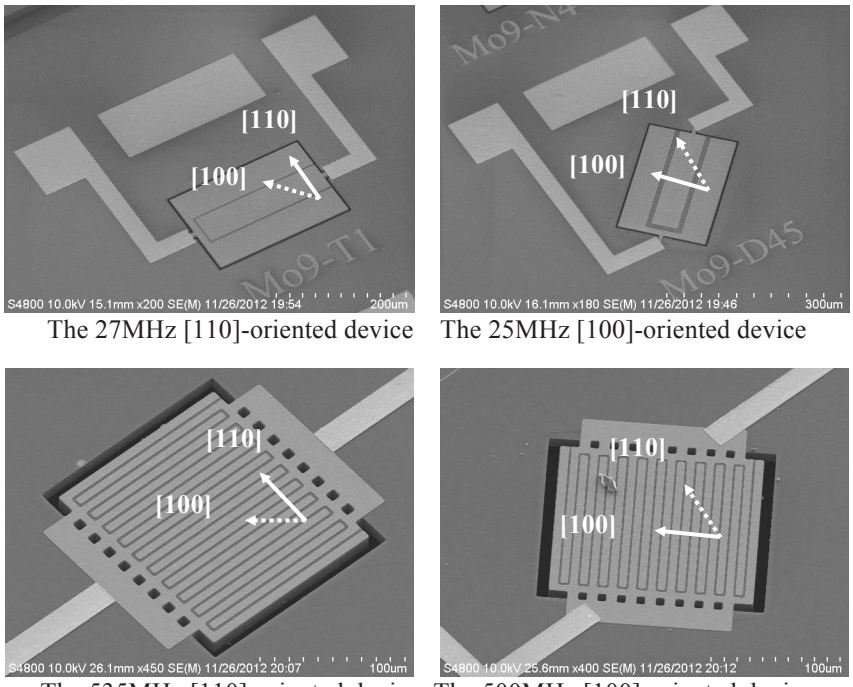

The 27MHz [110]-oriented device The 25MHz [100]-oriented device

The 535MHz [110]-oriented device The 500MHz [100]-oriented device

Figure 5-13. The SEM of fabricated TPoS resonators

5-3-3) Measurement results

Fabricated extensional-mode resonators in [110] and [100] (45º rotated) orientations were tested using a high frequency response measurement set-up. The frequency responses at different level of applied power were measured for both orientations. Resonators on lightly B-doped wafer are driven to nonlinearity and both show the spring softening effect (figures 5-14 and 5-15). It should be noted that the layout fabricated on this wafer was different than the other three wafers and the resonators operate at a different frequency range.

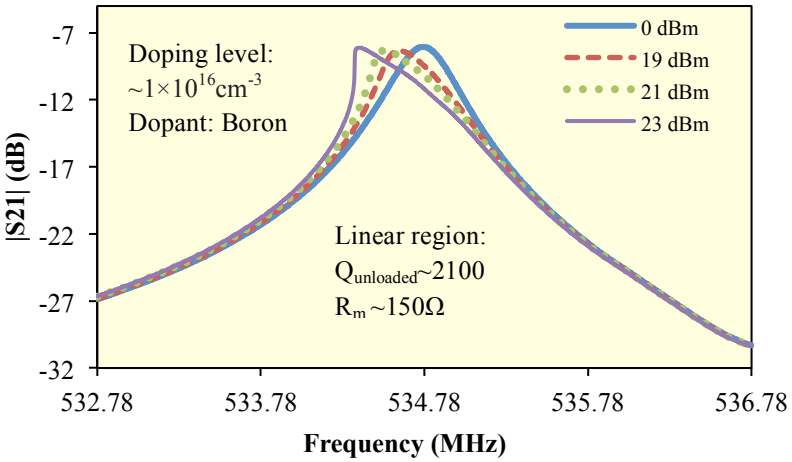

Figure 5-14. The frequency response of ~535MHz lightly B-doped [110]-oriented device for varying applied power

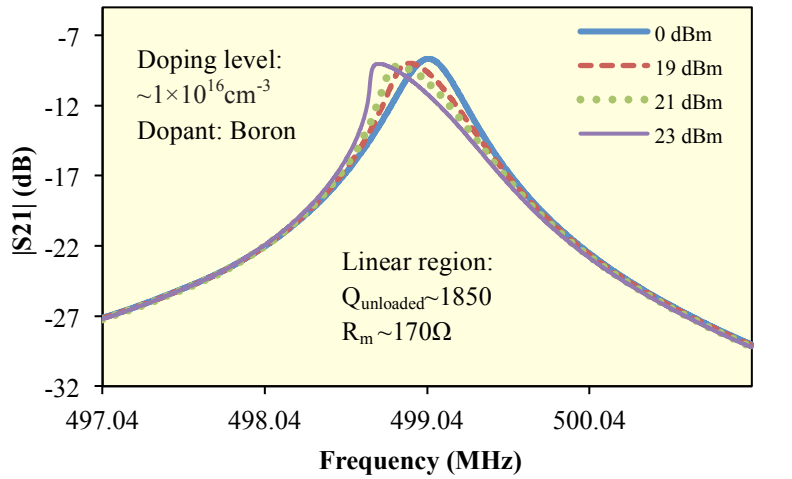

Figure 5-15. The frequency response of ~500MHz lightly B-doped [100]-oriented device for varying applied power

However, the nature of nonlinearity in extensional resonators is not frequency dependent. Resonators in both orientations on highly B-doped wafer are also driven to nonlinearity and both show the spring softening effect (figures 5-16 and 5-17). These results imply that the nature of nonlinearity in p-type doped silicon resonator (lightly and highly doped) is spring softening for both orientations.

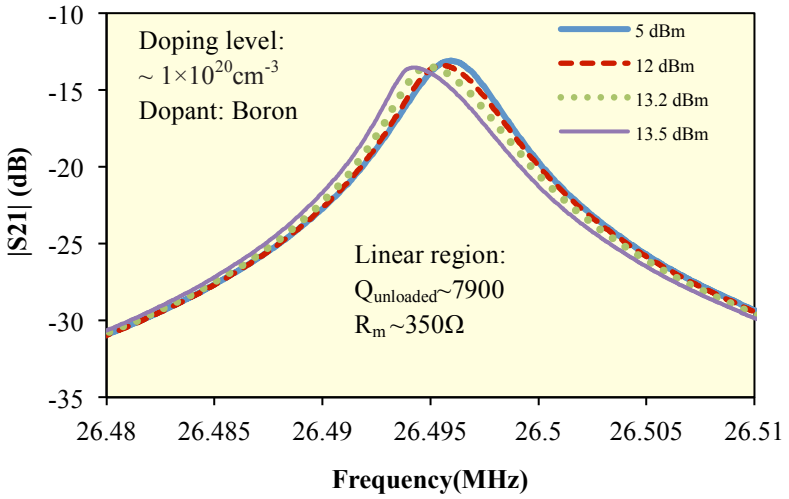

Figure 5-16. The frequency response of ~26.5MHz highly B-doped [110]-oriented device at varying applied power

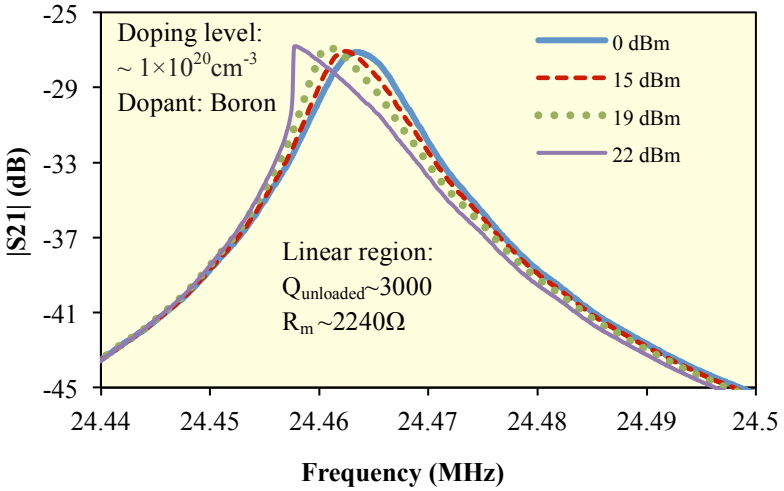

Figure 5-17. The frequency response of ~24.5MHz highly B-doped [100]-oriented device for varying applied power

The [110]-oriented resonators on highly P-doped wafer also show spring softening (figure 5-18). However, it is observed that [100]-oriented resonators on highly P-doped wafer exhibit spring hardening (figure 5-19). The same trends are observed for As-doped resonators (figures 5-20 and 5-21). Moreover, by comparing the figures 6-19 and 6-21, it is clear that the device with lower doping level is less susceptible to be driven to nonlinearity compared to higher doped device. In fact the device on the As-doped wafer mechanically failed (i.e. fractured) at 10dBm input power before ever reaching to its bifurcation point.

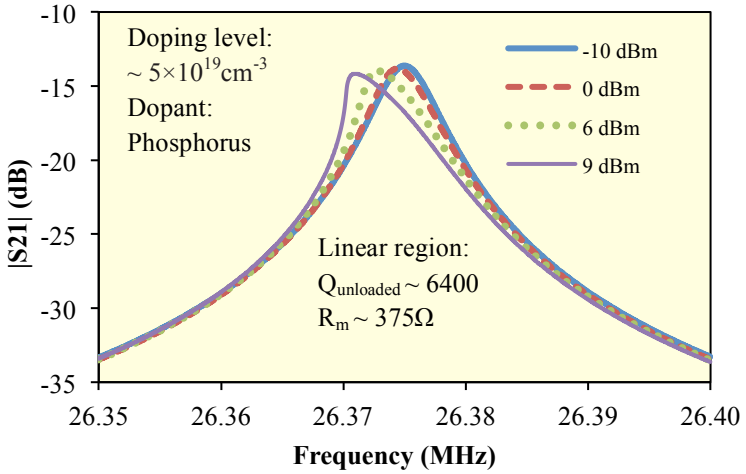

Figure 5-18. The frequency response of ~26.5MHz highly P-doped [110]-oriented device at varying applied power

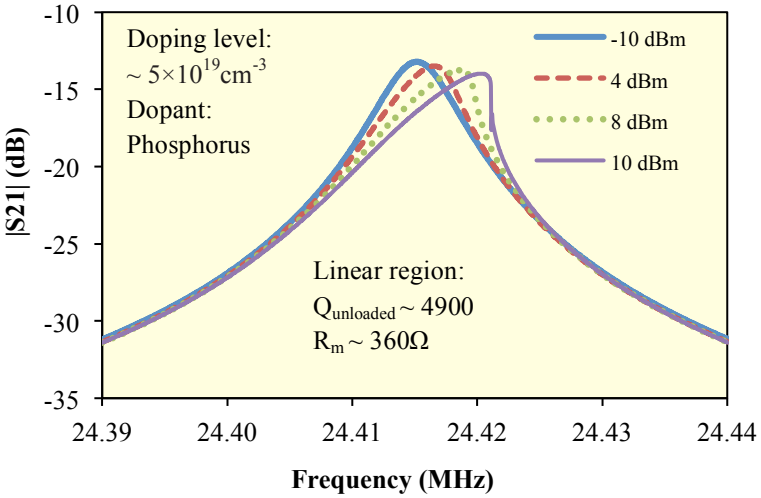

Figure 5-19. The frequency response of ~24.5MHz highly P-doped [100]-oriented device at varying applied power

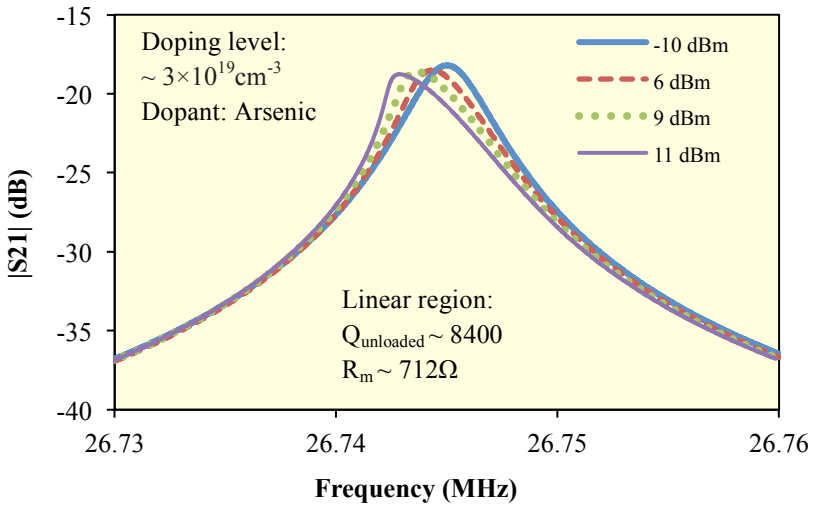

Figure 5-20. The frequency response of ~26.7MHz highly As-doped [110]-oriented device at varying applied power

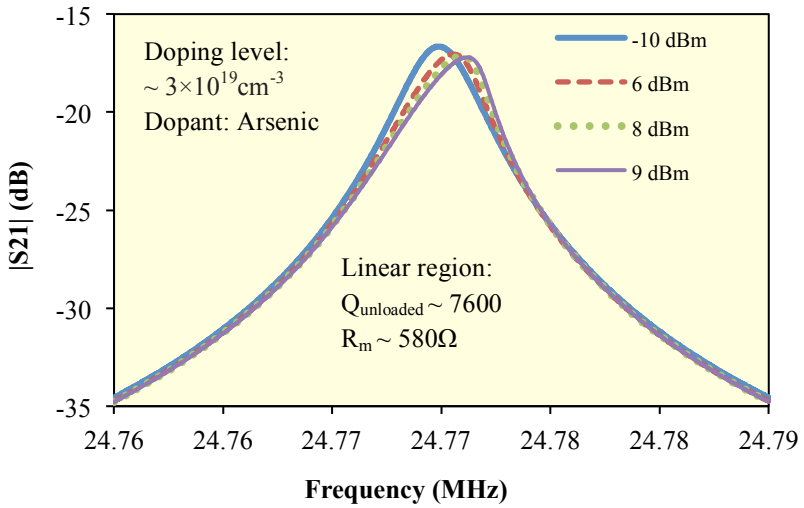

Figure 5-21. The frequency response of ~24.7MHz highly As-doped [100]-oriented device at varying applied power

5-3-4) Nonlinearity comparison

In order to compare the nonlinearity of highly P- and As-doped [100]-oriented silicon resonators, normalized frequency shift is utilized, which is a measure of relative peak frequency shift at variable vibration amplitude [14]. The stored energy density in the resonators at different applied

power is also calculated by taking advantage of the measured S-parameters of the devices and resonator modeling using ADS software [56]. The normalized frequency shift versus stored energy density is calculated for highly P- and As-doped [100]-oriented devices and is shown in figure 5-22. As it is seen As-doped device is less susceptible to be driven into nonlinearity operation region rather than the P-doped device. For instance, at the stored energy density of ~0.2×10^6 J/m^3 the frequency shifts of As-doped device is half of that of the P-doped resonator, which shows ~100% improvement in linearity for the As-doped device.

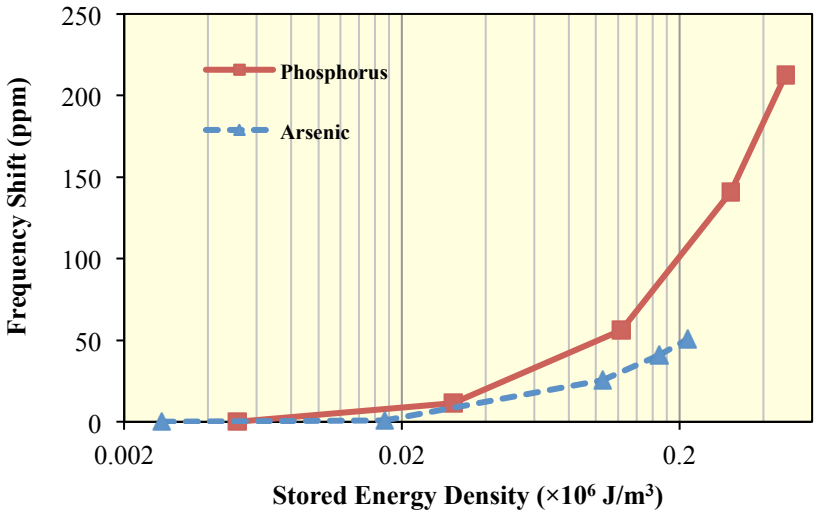

Figure 5-22. The normalized frequency shift versus applied power for highly As- and P- doped [100]-oriented devices

It is envisioned that the doping concentration for n-type doped [100]-oriented resonators can be appropriately selected to result in k_1 and k_2 cancelling each other. In such a device the resonator will behave very linear all the way to the point it fractures under extreme stress levels.

In this chapter the effect of the quality factor on nonlinearity of the thin-film piezoelectric-on-substrate (TPoS) resonators was investigated. It was showed that in thin-film piezoelectric-on-substrate (TPoS) resonators, the quality factor is significantly altered by varying the thickness of the resonator, but the power handling of the resonator is often traded off for the higher Q. Quality

factors measured from TPoS resonators fabricated on a 30µm thick silicon substrate are up to 3 times higher than the values measured for devices on 20µm thick substrate while maximum deliverable power (at the point of bifurcation) to the same device is reduced from 2.5dBm to -0.3dBm. Therefore, measurements confirmed that an increase in quality factor results in lower deliverable power to the device at bifurcation. However, by adding multiple supports at modal nodes along the device width a concurrent enhancement in quality factor and power handling can be achieved. It was observed that the maximum deliverable power in a multi-tether ~1GHz resonator is enhanced by more than 5dBm compared to an identical single-pair tethered resonator (7dBm versus 1.9dBm) and the quality factor is also increased by 55%.

It was also shown for the first time that nonlinearity in n-type doped silicon micro-resonators can be reduced by modifying the doping concentration and the resonator alignment to a different crystalline orientation. Spring hardening, a trend opposite to the commonly-observed spring softening, is demonstrated in extensional [100]-oriented resonators fabricated on highly phosphorus- and Arsenic-doped silicon substrate. By choosing the right doping concentration, the overall effect of amplitude-dependent stiffness coefficients can be reduced to near zero, which results in superior linearity in resonators.

CHAPTER VI

SHORT TERM FREQUENCY INSTABILITY IN TPOS OSCILLATOR

Phase noise is a critical measure of the short-term frequency stability in oscillators and it is associated with the frequency domain representation of random fluctuations in the phase of the oscillation waveform. Poor phase noise performance of the oscillator limits the maximum bitrate in data communication systems. Phase noise in an oscillator, due to the contribution of the resonator, depends on the resonator characteristics such as quality factor and power handling capability.

The MEMS resonators typically have a much lower power handling capability than that of a traditional macro-resonator due to their relatively small size. As the power applied to a high-Q MEMS resonator increases, the device is driven to its nonlinear operation region, which can consequently limit the lowest noise-floor achievable using the device in an oscillation loop.

Increasing the power delivered to a mechanical resonator will eventually increase the vibration amplitude to an extent that the small high-order elastic constants of the material can't be neglected (onset of nonlinearity). This will introduce a shift in the resonance peak toward lower (spring softening) or higher frequencies (spring hardening). At large vibration amplitudes (relative to the resonator size) the resonator reaches to a point beyond which multi-stable vibration amplitudes exist for a single frequency (Duffing bifurcation point).

It is traditionally believed that the oscillation power in an oscillator loop is limited by the maximum stored energy in the resonator at bifurcation point. A chaotic change in the frequency is expected at bifurcation and consequently the phase-noise performance is degraded [5]. This issue is of great concern in MEMS resonators because they can store less energy compared to bulky crystal resonator as a result of their very small size. On the other hand, there exists a body of theoretical work on the topic of nonlinear oscillators that suggests operation of the mechanical resonator at bifurcation yields improved overall oscillator circuit noise [57].

In this chapter the dependency of the phase noise and jitter on the resonator characteristics (i.e. quality factor and motional impedance) and oscillation power are studied. Particularly a 27MHz oscillator is reported with very low cycle-to-cycle jitter based on a TPoS resonator driven beyond the bifurcation point. For the first time, the results seem to provide experimental validation for the speculated suppression of overall oscillator circuit noise through the operation of the resonator beyond the bifurcation. In this research a phase-noise as low as -130dBc/Hz @ 1kHz offset from carrier is measured for these TPoS oscillators, which is comparable with the results, reported for quartz oscillators.

The measurement confirms that the oscillator jitter is scaled down after the TPoS resonator reaches the bifurcation and the close-to-carrier phase-noise of the oscillator doesn't seem to deteriorate. Also, it is shown that the jitter in the 27MHz oscillator based on TPoS resonator at any oscillation amplitude is lower for a device with lower motional impedance.

6-1) Overview of Oscillator characteristics

An oscillator in general can be model by the block diagram as shown in figure 5-1. Oscillation is achieved by feeding back enough electrical energy that is delayed by $2\pi n$ radian such that the total gain of the loop (loop gain) is unity. Barkhausen‘s Criterion expresses the necessary conditions for steady state oscillation as:

$$|A(\omega)|.|F(\omega)| = 1 \qquad \text{Amplitude condition}$$

$$\varphi_A(\omega) + \varphi_F(\omega) = 2\pi n \quad n \in 0, 1, 2, \ldots \qquad \text{Phase condition}$$

where $A(\omega)$ is the transfer function of the amplifier that pumps enough energy to the loop in order to keep the oscillation, $F(\omega)$ is the transfer function of the feedback element, and ω is the oscillation angular frequency ($\omega = 2\pi f$).

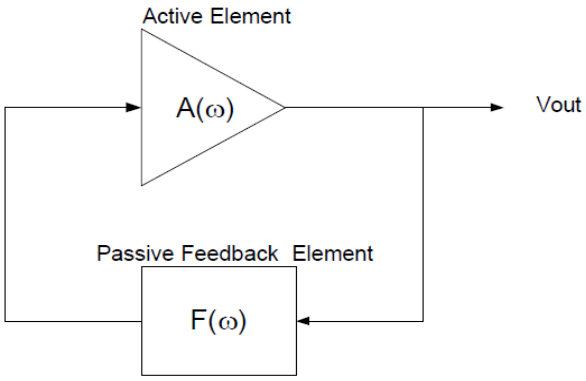

Figure 6-1. A general oscillator block diagram

6-2) Phase noise

Noise in an oscillator is commonly characterized either in frequency domain (phase-noise) or time (jitter).

$$v(t) = V_0 \sin(\omega_0 t) \qquad \text{Ideal oscillator}$$

$$v_n(t) = \big(V_0 + \epsilon(t)\big)\sin(\omega_0 t + \phi(t)) \qquad \text{Noisy oscillator}$$

Phase noise is the frequency domain representation of rapid, short-term, random fluctuations in the phase of a waveform and is a critical measure of the frequency stability in oscillators. Figure

5-2 depicts the effect of the phase noise on power spectral density of ideal and non-ideal oscillator.

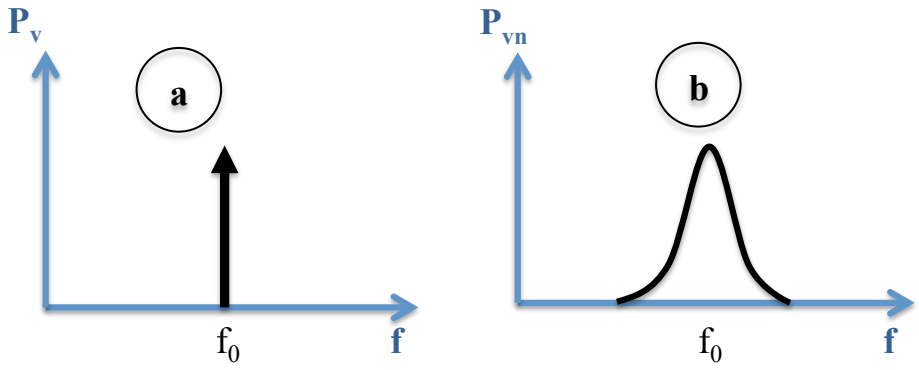

Figure 6-2. Phase noise of a) ideal b) non-ideal oscillator

$$L(f_m - f_o) = 10log(S_\phi(f_m)/S_\phi(f_0)) \quad \text{in dBc/Hz}$$

where $S_\phi(f)$ is the spectral density of phase fluctuation.

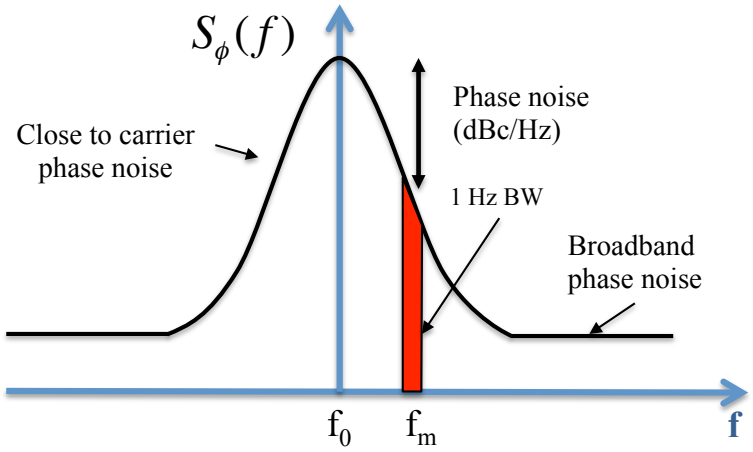

Figure 6-3. Oscillator power spectrum, $S_\phi(f)$, in existing the phase noise

It is usual to characterize an oscillator in terms of its single-sideband phase noise as shown in figure 5-4, where the phase noise in dBc/Hz is plotted as a function of frequency offset, fm, with the frequency axis on a log scale. Note that the actual curve is approximated by a number of

regions, each having a slope of $1/f_n$, where n = 0 corresponds to the "white" phase noise region or noise floor (slope = 0 dB/decade), and n = 1 corresponds to the "flicker" phase noise region (slope = –20 dB/decade). There are also regions with n = 2, 3, 4, ... where occur progressively closer to the carrier frequency.

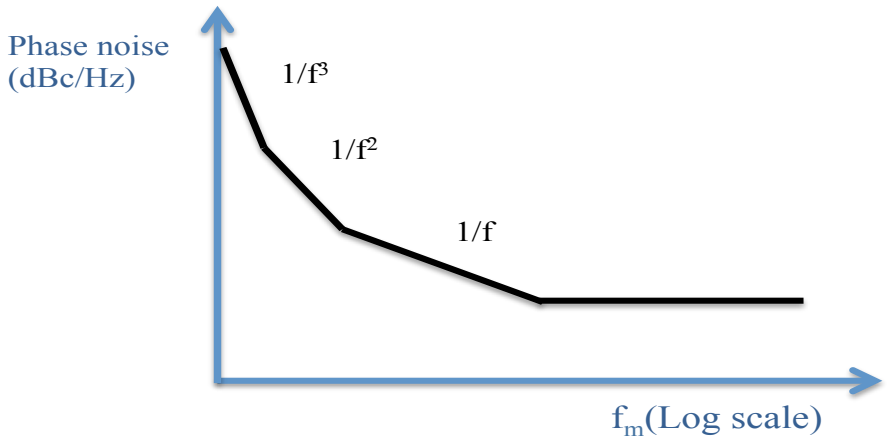

Figure 6-4. Oscillator phase noise versus frequency offset

Leeson's model predicts the phase noise-to-carrier ratio in an oscillator as [58]:

$$L(\Delta\omega) = 10\log\left[\frac{2FkT}{P_0}\left(1+\left(\frac{\omega_0}{2Q\Delta\omega}\right)^2\right)\left(1+\frac{\Delta\omega_{1/f^3}}{|\Delta\omega|}\right)\right] \qquad (6-1)$$

where ω_0 is the carrier frequency, $\Delta\omega$ is the frequency offset, Q is the quality factor of the resonator, P_0 is the oscillation power, k is the Boltzmann constant, T is the equivalent noise temperature and F is an empirical fitting parameter. Based on this model, the phase noise in an oscillator is inversely proportional to the oscillation power.

6-3) Jitter

Jitter is the time variation of a periodic signal in electronics and data communications (figure 6-5). The presence of jitter in oscillators introduces sampling error, which confines the bit rate in the communication systems.

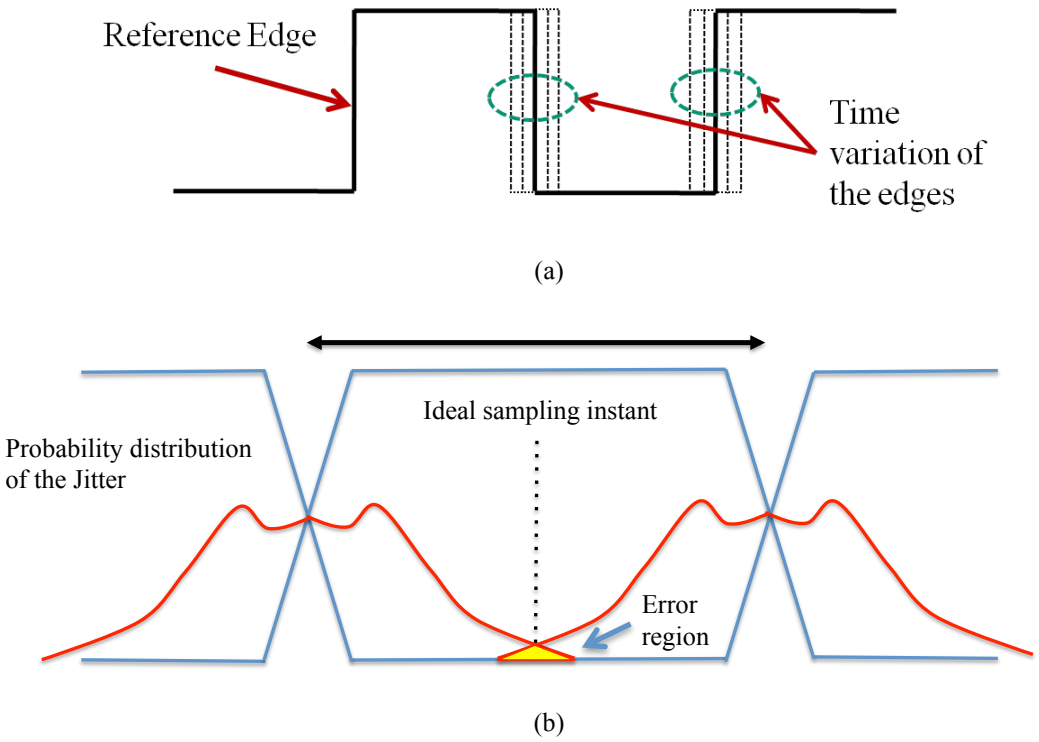

Figure 6-5. Phase Noise Integration to determine a) time variation of the edges b)The probability of occurring an error

Period jitter compares the length of each period to the average period of an ideal clock at the long-term average frequency of the signal (figure 6-6). Cycle-to-cycle jitter compares the difference in the period length of adjacent cycles. (figure 6-6).

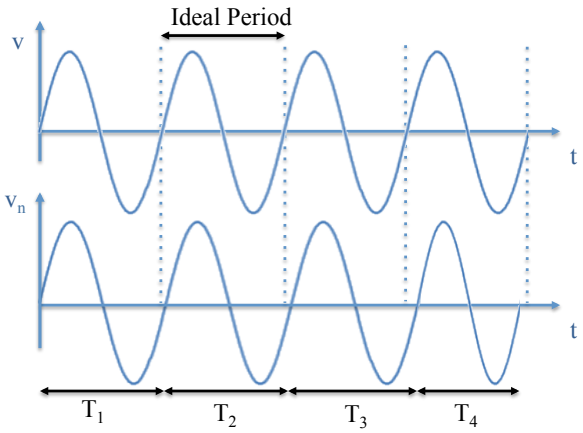

Period jitter: The standard deviation of the period

$$\sigma_T = \sqrt{\mathrm{var}(T_k)}$$

Cycle-to-cycle: The standard deviation of the difference adjacent cycles

$$\sigma_{\Delta T} = \sqrt{\mathrm{var}(T_{k+1} - T_k)}$$

Figure 6-6. Period and cycle-to-cycle jitter definition

6-4) Jitter dependency on the phase noise

For many communications applications, the total noise power over a specific range of frequencies as shown in figure 6-7 is important. In order to determine the power over the frequency range (bandwidth), the time domain signal should be analyzed in the frequency domain, and then reconstructed in the time domain into an rms value with the unwanted frequencies excluded. This may be done by converting $L(\Delta\omega)$ back to $S_\phi(f)$ over the bandwidth, integrating and performing some additional calculations. The result is an rms value for $\phi(t)$ and is expressed seconds. This value represents 1 standard deviation of phase jitter associated with the noise in the defined bandwidth. The common integration bandwidth is from 12kHz to 20MHz.

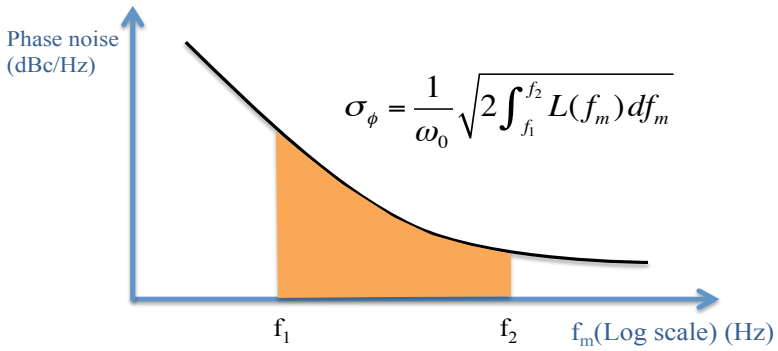

Figure 6-7. Phase Noise Integration to determine bandwidth limited (500 to 10000 Hz) phase jitter

6-5) Resonator characterization

By varying the design features such as top electrode pattern, TPoS resonators with different characteristics can be fabricated at similar frequency. Three ~27MHz TPoS resonators with a range of various characteristics (Table 6-1) are fabricated and chosen to be used in the oscillators in order to enable investigation of the effect of resonator characteristics on the oscillator performance. Frequency responses of each device as well as their SEM pictures are shown in figure 6-8 (All measured quality factors are in air).

Table 6-1. Devices characteristics

	Quality factor	Motional Impedance (Ω)
Device A	16041	400
Device B	28819	430
Device C	28904	1073

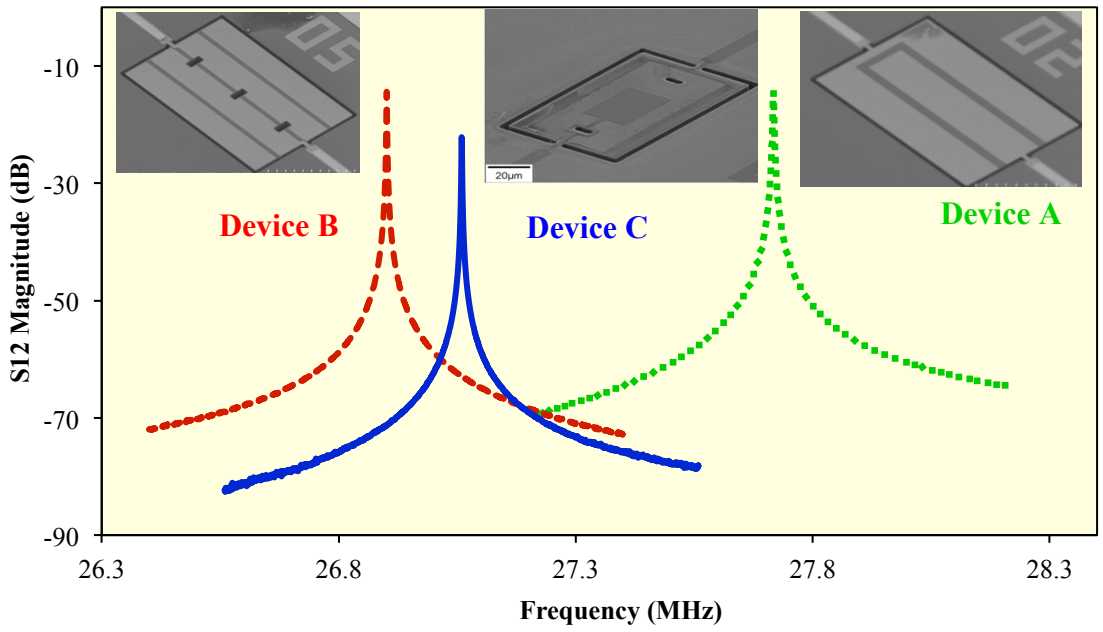

Figure 6-8. Frequency response and SEM's of three different 27MHz resonators

To study the nonlinearity in these resonators, the frequency responses of the resonators are measured at different delivered power to the resonator using Agilent E8358A PNA network analyzer. The normalized frequency shift is calculated and shown in figure 6-10.

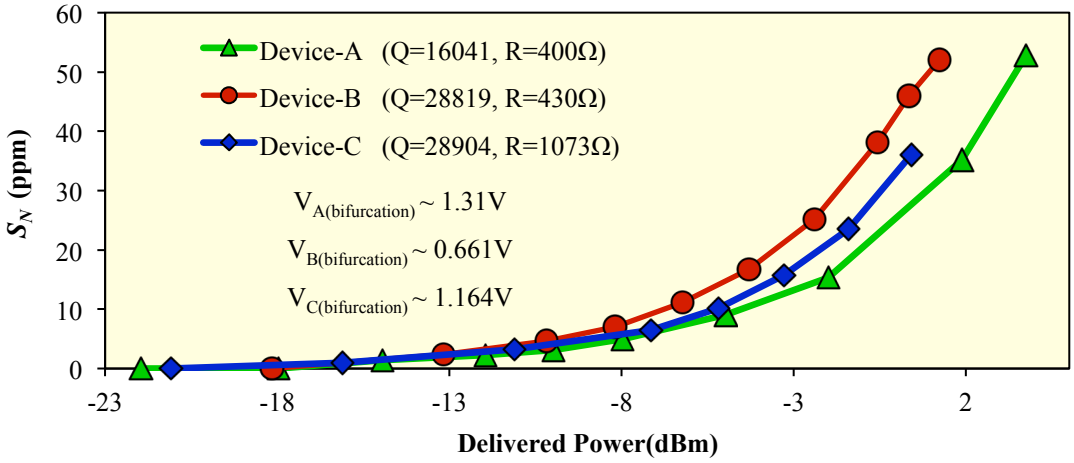

Figure 6-10. Nonlinearity measurement of three different 27MHz resonators

As it is clear from this figure, between resonators A and B with almost the same motional impedance, resonator B with higher Q is more nonlinear. Also, between resonators B and C with almost the same Q, the resonator with smaller motional impedance is more nonlinear. These observations are expected since both higher Q and lower impedance result in a larger portion of the delivered power to be absorbed by the resonator. Considering similarity in the size of all three resonators, larger amount of absorbed energy will cause the resonator to behave nonlinearly at a lower onset.

In order to find the value of the applied voltage to the device at bifurcation, upward and downward frequency sweeps are examined around the resonant peak. The bifurcation is detected at a point the two corresponding frequency responses begin to deviate from each other (figure 6-11).

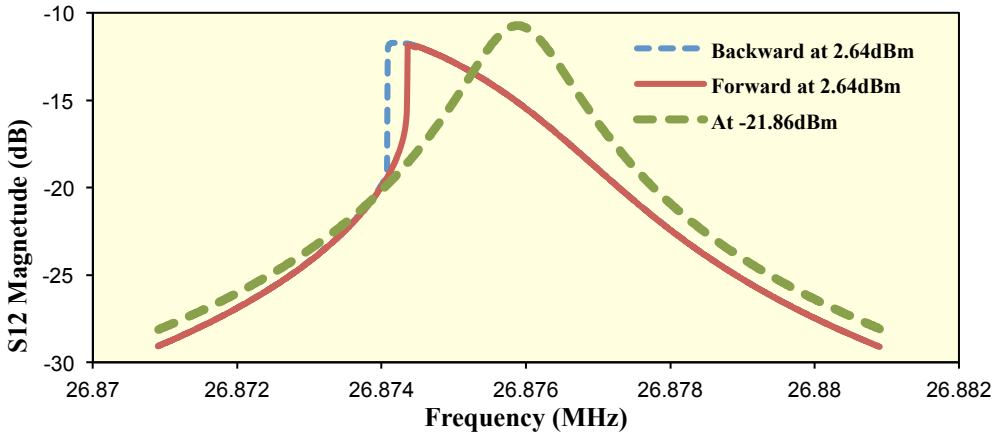

Figure 6-11. Frequency response of a 27MHz resonator at different delivered

6-6) TPOS oscillator

The schematic of the oscillator circuit used in this research is shown in figure 6-12a. This circuit consists of a trans-impedance amplifier (SA5211), which provides the gain, and a comparator (TVL3501), which is used to produce a square waveform (figure 6-12b). The comparator, which is a highly nonlinear component, is included in the oscillation loop in order to create simple means to control the applied voltage to the resonator over a very wide range. In this circuit the amplitude of the applied voltage to the resonator is adjusted by the potentiometer R5. The duty cycle of the waveform is also tuned to 50% by potentiometer R2 before collecting jitter at each applied voltage. The assembled oscillator circuit utilizing a TPoS resonator is shown in figure 6-13.

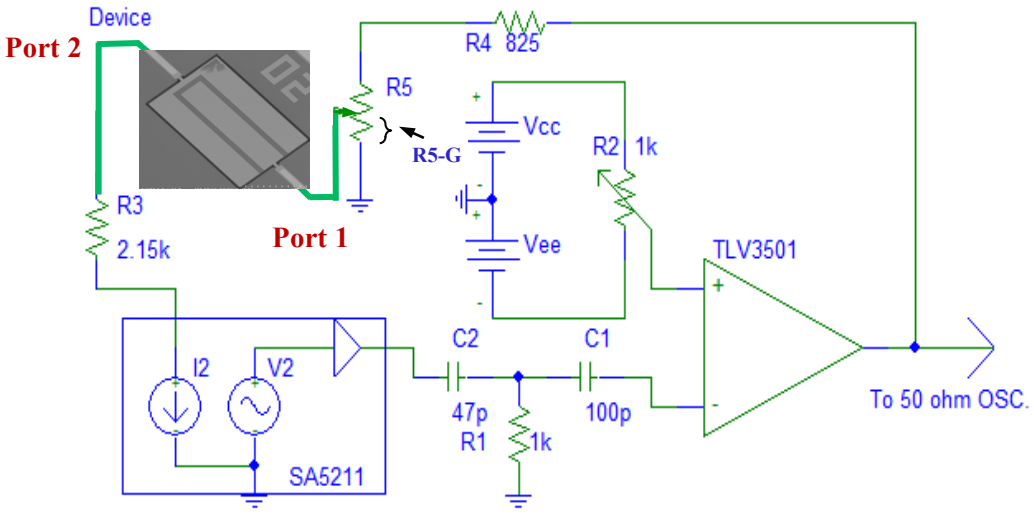

(a)

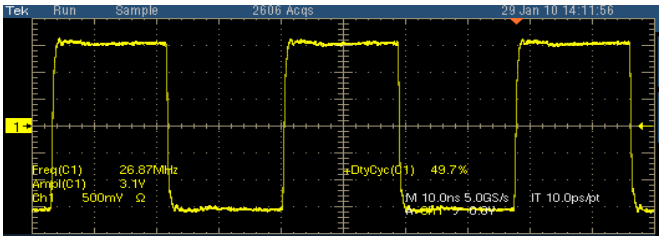

(b)

Figure 6-12. a) The schematic of the oscillator circuit, b) Output waveform

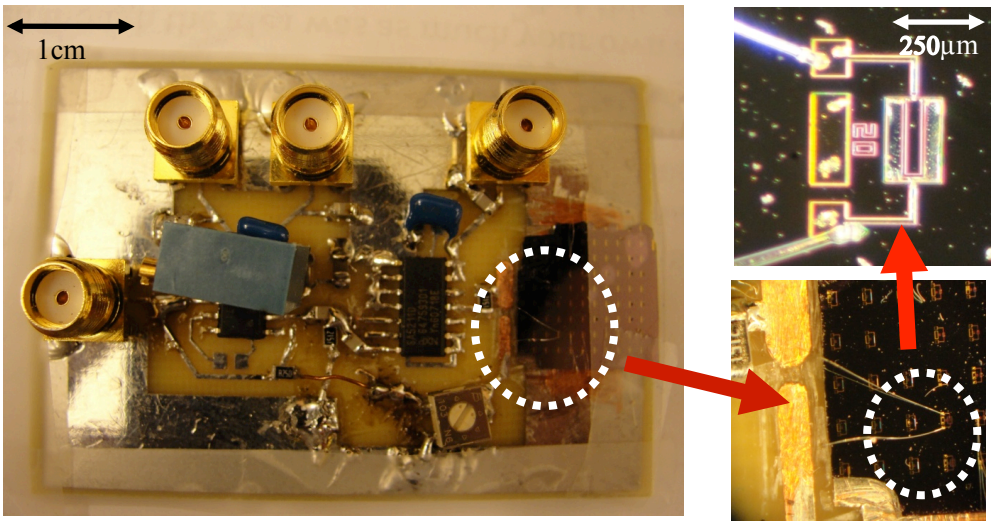

Figure 6-13. The assembled oscillator circuit

6-7) Oscillator characterization

Three oscillator boards were assembled using the aforesaid resonators. The oscillator jitter is measured using a Tektronix oscilloscope model TDS5104B. The measured standard deviation (STD) of the cycle-to-cycle jitter as a function of the voltage amplitude applied to the device is plotted for the three oscillators in figure 6-14.

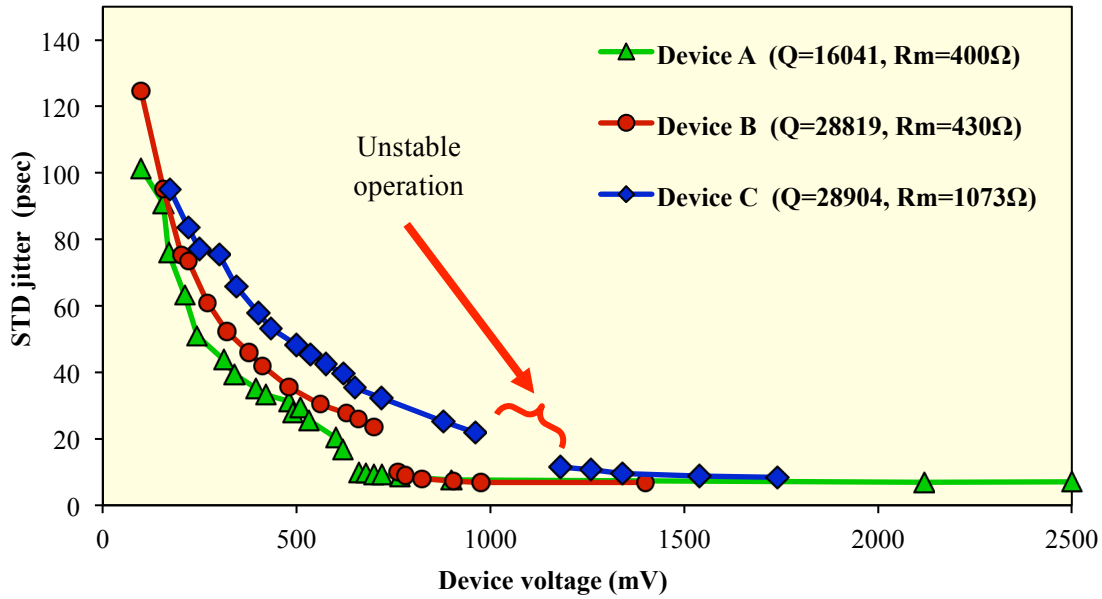

Figure 6-14. Jitter versus device voltage for three different 27MHz Oscillators

It is observed that in all three oscillators the jitter gradually decreases as the amplitude of the resonator input voltage increases. This trend is disrupted at a specific voltage at which a chaotic behavior in the oscillator is triggered. There is a range of fractional resistances (labeled as R5-G in figure 6-12a) at which the oscillator is not stable and the measured jitter is extremely high (Nano seconds range). However, as R5-G is further increased the oscillator stabilizes again yielding a scaled down jitter value compared to the last stable point. Further increasing the applied voltage beyond this point will only cause slight improvement in the cycle-to-cycle jitter and the minimum value for all three resonators are very close (~7 psec STD). It was observed that at any applied voltage, the oscillator built based on the resonator with the lowest motional impedance yields the lowest measured jitter.

In order to better understand the nature of discontinuity in the jitter vs. voltage curves, the experiment was repeated at more data points around the discontinuity region for the oscillator based on device B (figure 6-15).

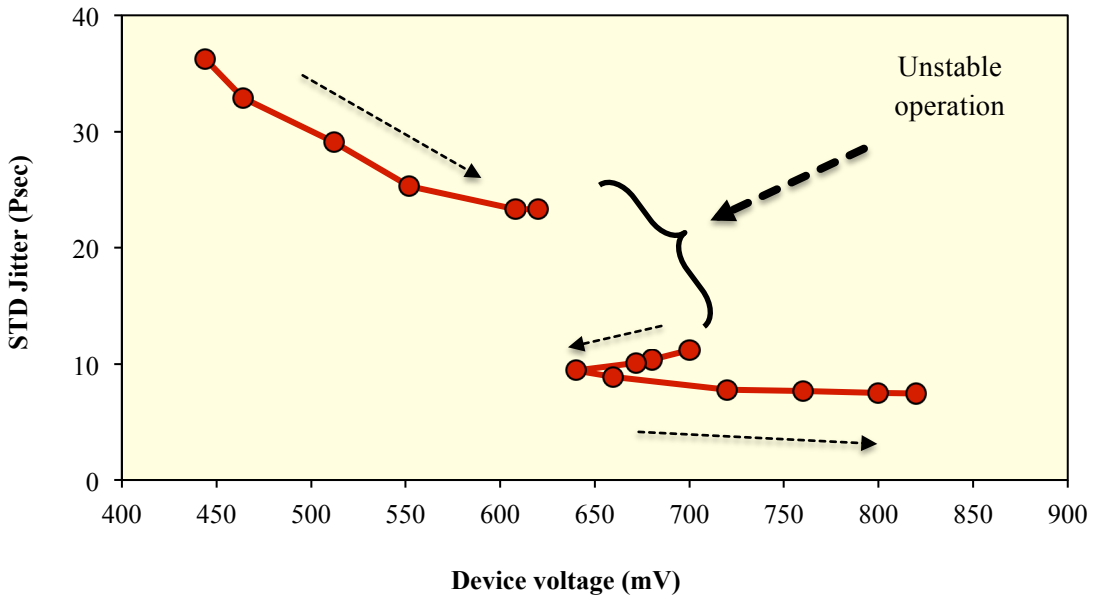

Figure 6-15. Jitter versus device voltage for for oscillator utilizing device B in a closer view

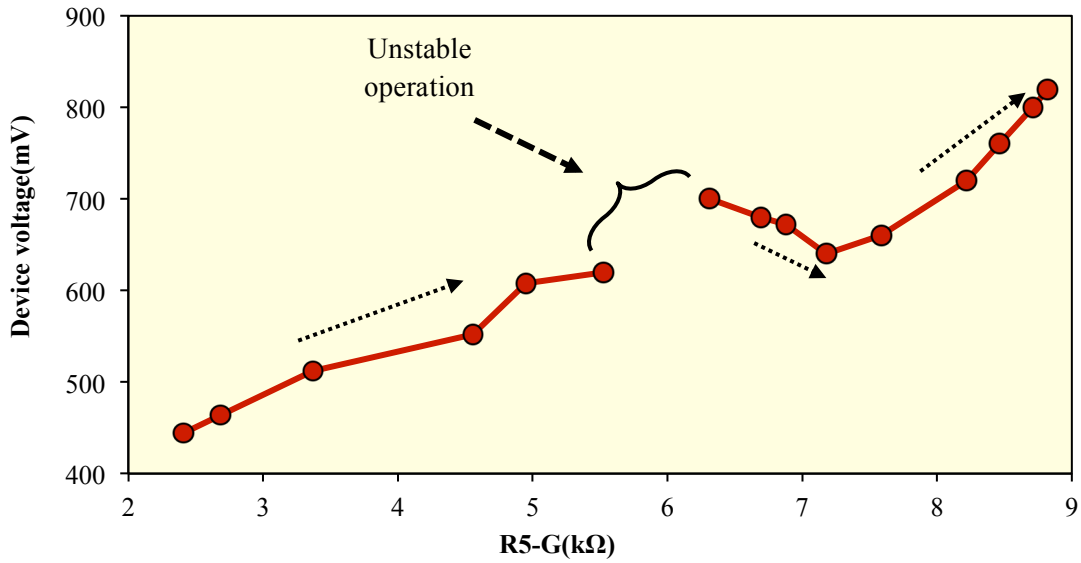

Figure 6-16. Device voltage versus fractional resistance R5-G for oscillator utilizing device B

Results interestingly show (figure 6-16) that for a small range of R5-G, the applied voltage trend is reversed (i.e. voltage decreases as R5-G increases). This means that for this range the equivalent impedance seen from the input of the device is reducing. This change in the input impedance can be attributed to a sudden shift in the vibration amplitude occurring right at the bifurcation in the resonator.

Using the collected data, output (port 2) current of the resonator versus the input (port 1) current is drawn in figure 6-17. It is interesting to see that the data show two segment trend lines with different slopes for values before and after instability. This observation is the promising evidence that the resonator might be switching to new stable point in frequency response of the resonator. Figure 6-18 also depicts the output voltage versus input voltage of the resonator. This observation might be a clue that the oscillator amplitude is passing the Duffing bifurcation point of the resonator.

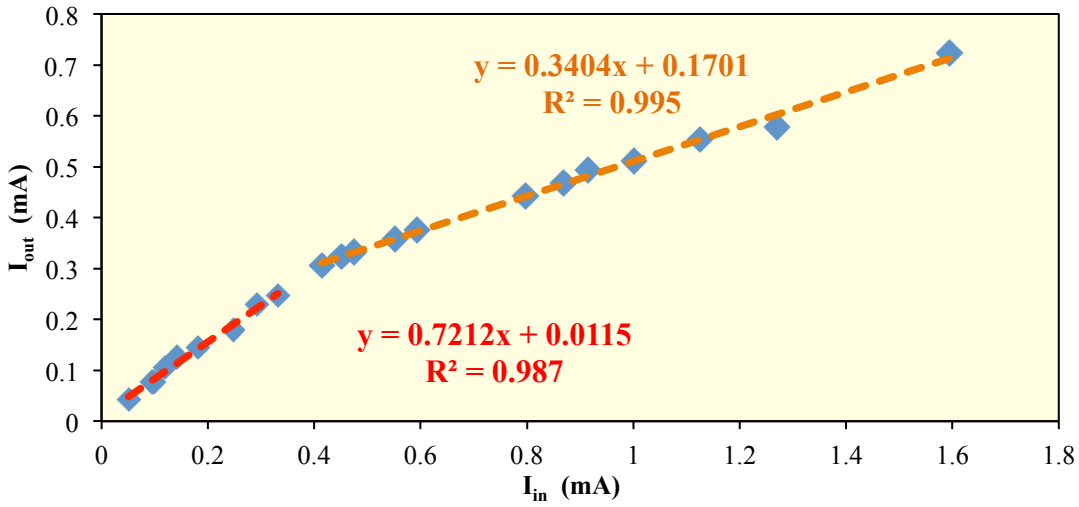

Figure 6-17. Output current versus input current while changing R5-G

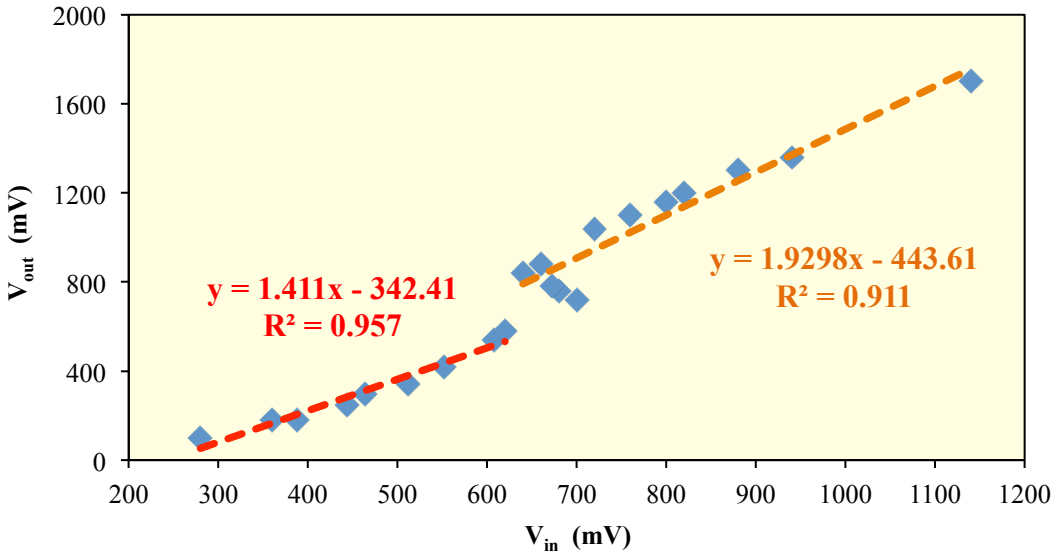

Figure 6-18. Output voltage versus input voltage while changing R5-G

It is also observed that the oscillation frequency is changing as the input voltage of the device increases (figure 6-19). Indeed, increasing in input voltage is a result of changing the R5-G. Although frequency varying is not much in this case, it is the beginning of the research on frequency tuning in TPoS oscillator, which is the subject of the next chapter.

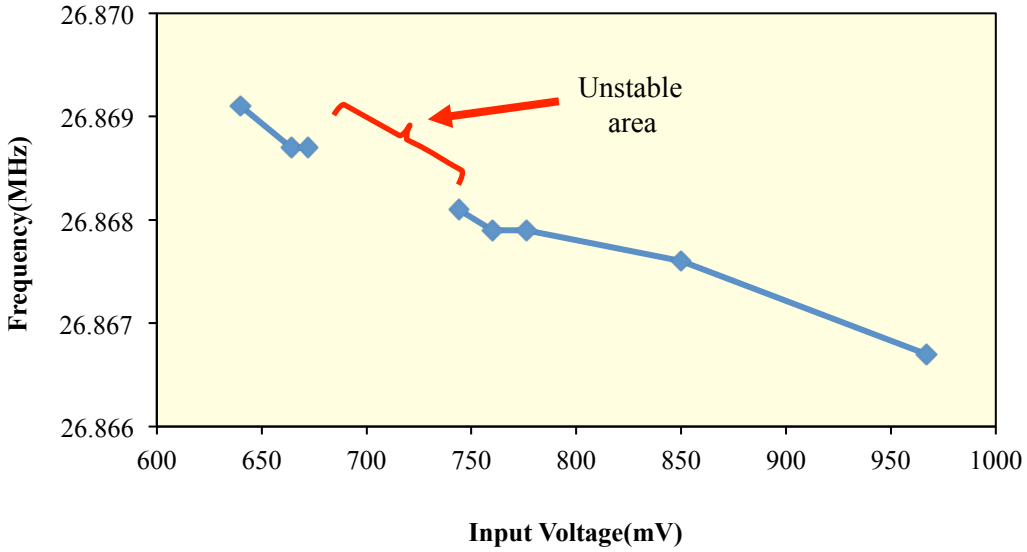

Figure 6-19. Output voltage versus input voltage while changing R5-G

Phase noise for these three oscillators is also measured and overlapped in figure 6-20. These measurements are taken at similar applied voltages (~455mV) to ensure operation of the resonators below the unstable region (which is believed to correspond to the bifurcation point of the resonator). As it is clear, the oscillator with the lowest motional impedance device (device A) exhibits the lowest noise floor, which agrees with the jitter measurement results. The maximum peak-to-peak and cycle-to-cycle jitters are also recorded for these oscillators (inset table of figure 6-20) and they confirm similar superiority for the device with the lowest motional impedance.

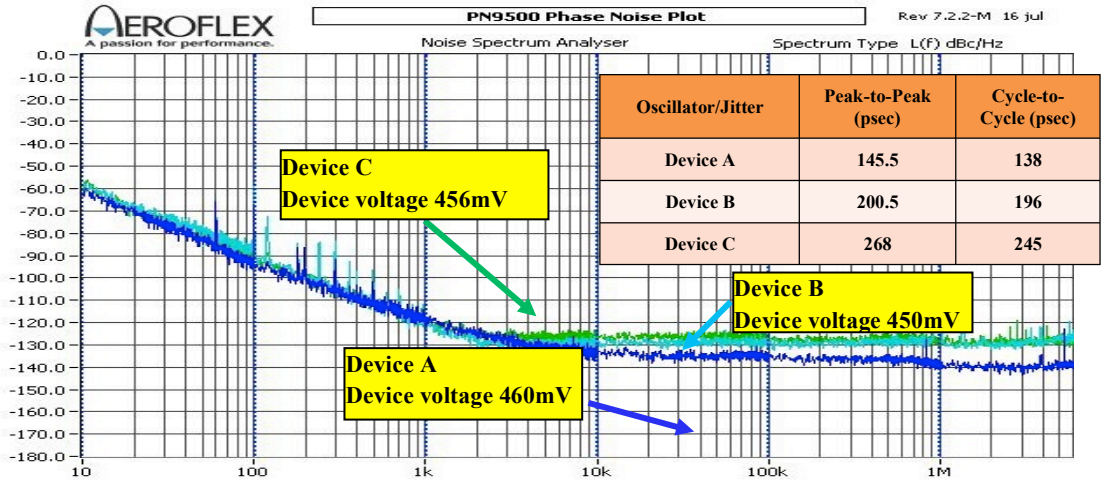

Figure 6-20. Phase noise measurement of device A, B and C

Finally, a similar oscillator using a resonator with very low motional impedance (~267Ω) was assembled. This time the device voltage amplitude was intentionally set beyond the unstable region of the jitter vs. voltage curve and the phase noise measurement was repeated (figure 6-21). This curve shows improvement in both close-to-carrier and noise floor compared to the oscillators tested in figure 6-21. It should be noticed that the recorded standard deviation for the cycle-to-cycle jitter in this oscillator is also the same as those recorded for the other three oscillators beyond the unstable region and therefore, similar noise floors are expected for all of these oscillators. The measured phase noise of -130dBc/Hz at 1kHz offset from carrier for this oscillator is very promising for MEMS oscillators and is comparable with the results reported for quartz oscillators.

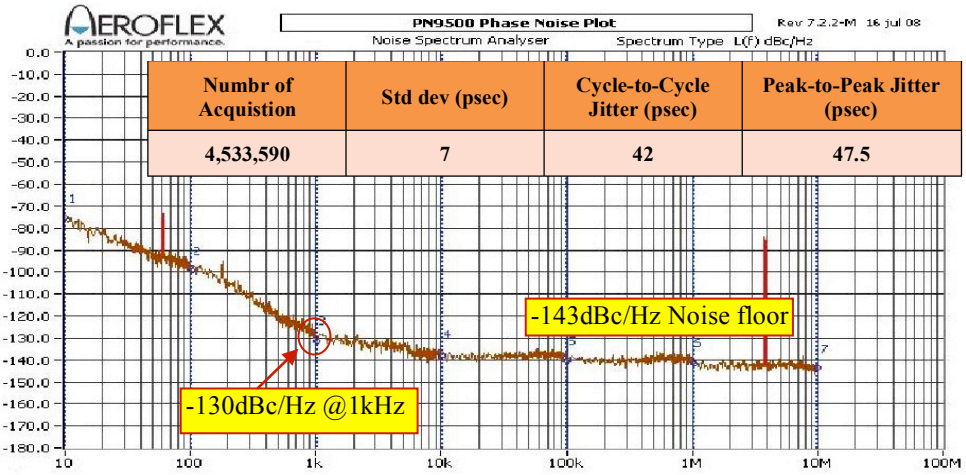

Figure 6-21. Phase noise measurement of device A

In this research, the evidence of suppressed overall noise in a MEMS-based oscillator is shown as a result of operating the resonator beyond the bifurcation point. If solidly proven through ongoing in-depth investigations, this is the first time that such experimental proof for this speculated result is observed. Meanwhile, the motional impedance of the thin-film piezoelectric-on-substrate (TPoS) resonator was shown to have a dominant effect on the oscillator jitter. Resonators with lower motional impedance seem to yield lower jitter at any given oscillation amplitude. However,

cycle-to-cycle jitter for all oscillators assembled based on different TPoS resonators converged to the same level of ~7psec standard deviation at very large device applied voltages.

CHAPTER VII

TEMPERATURE COMPENSATION IN TPOS RESONATORS BY N-TYPE DOPING

In this chapter, we introduce a passive temperature compensation technique for silicon-based lateral extensional microresonators, which is based on properly orienting an extensional-mode resonator on a highly doped n-type silicon substrate. We show that the TCF sign is changed from positive to negative (turnover point) within the industrial temperature range (−40C−85C). This is a very simple technique that does not require any modification to the fabrication process. We have chosen thin-film piezoelectric-on-substrate (TPoS) resonator as a platform to analyze the effect of doping con- centration and crystal alignment on TCF [59], [60], [61]. A similar approach has been recently taken in capacitive square-shaped silicon resonators [62] .

7-1) Theory

Assuming a 2D approximation, the resonance frequency of a bulk extensional-mode micro-resonator is given by:

$$f = \frac{1}{2a}\sqrt{\frac{E}{\rho}} \tag{7-1}$$

where ρ is the resonator material density, a is the frequency-defining feature size (i.e. dimension in the direction of mechanical vibration for a first harmonic resonance mode), and E is the effective Young's modulus of the resonant structure in the acoustic wave propagation direction.

In single crystalline silicon, the Young's modulus depends on the elastic constants and the orientation. For example, in [100] and [110] planes, E is calculated as follows:

$$E_{[100]} = c_{11} - 2\frac{c_{12}^2}{c_{11} + c_{12}} \tag{7-2}$$

$$E_{[110]} = 4\frac{(c_{11}^2 + c_{12}c_{11} - 2c_{12}^2)c_{44}}{2c_{44}c_{11} + c_{11}^2 + c_{12}c_{11} - 2c_{12}^2} \tag{7-3}$$

where c_{ij} are elastic constants. As a result, the temperature-induced frequency variation depends on the direction and the variation of the elastic constants vs. temperature.

In single crystalline silicon, induced strain shifts the energy levels of equivalent conduction bands. Consequently, the electrons in valleys whose energy levels are raised by strain transfer to lower energy valleys such that the total free energy in the crystal is minimized. Since these energy levels vary with the introduction of doping impurities in the crystal, the total free energy of the system also changes. This change in the free energy consequently affects the elastic constants of the material because the elastic constants are the strain derivatives of the free energy according to (7-4), where G is the Gibbs free energy, V_0 is the volume of non-deformed crystal and S is the strain [62], [55].

$$c_{ij} = \frac{1}{V_0}\frac{\partial^2 G}{\partial S_i \partial S_j} \tag{7-4}$$

For free electrons, the electronic contributions to the elastic constants can be predicted from Keyes' theory [54]. In the case of n-type silicon, the contribution of free electrons on the elastic constants is calculated as [55]:

$$\delta c_{11} = -\frac{2}{9}N\frac{\Xi_u^2}{E_f}X,\ \ \delta c_{12} = \frac{1}{9}N\frac{\Xi_u^2}{E_f}X,\ and\ \ \delta c_{44} = 0 \tag{7-5}$$

where N is the electron concentration, Ξ_u is the uniaxial deformation potential constant and X is defined as:

$$X = \eta F'_{1/2}(\eta) / F_{1/2}(\eta) \tag{7-6}$$

where F is the Fermi integral, η is E_f/kT, *and* E_f is the Fermi energy relative to the band edge.

Using (7-5), the contribution of doping levels on the elastic constants, c_{11}, c_{12} and c_{44} (i.e. δc_{11}, δc_{12} and δc_{44}) at any temperature is calculated. These values as well as the temperature dependent elastic constants of pure silicon [63] are then utilized to compute the elastic coefficients of doped silicon at each temperature as in (7-7).

$$c_{ij}(T) = c_{ij,pure}(T) + \delta c_{ij}(T) \tag{7-7}$$

where,

$$\frac{1}{c_{ij,pure}}\frac{dc_{ij,pure}}{dT} = \alpha_{ij} \quad \{ij\} = \{11, 12, 44\}$$

$$\alpha_{11} = -75.3\times10^{-6}\ \mathrm{K}^{-1}$$
$$\alpha_{12} = -24.5\times10^{-6}\ \mathrm{K}^{-1}$$
$$\alpha_{44} = -55.5\times10^{-6}\ \mathrm{K}^{-1}$$

The calculated elastic constants versus temperature using Keyes' theory for doping concentrations of N = 4×10^{19} cm^{-3} and N = 4.75×10^{19} cm^{-3} are shown in the figure 7-2. The calculated elastic constants versus doping level for two typical temperature points are also shown in this figure.

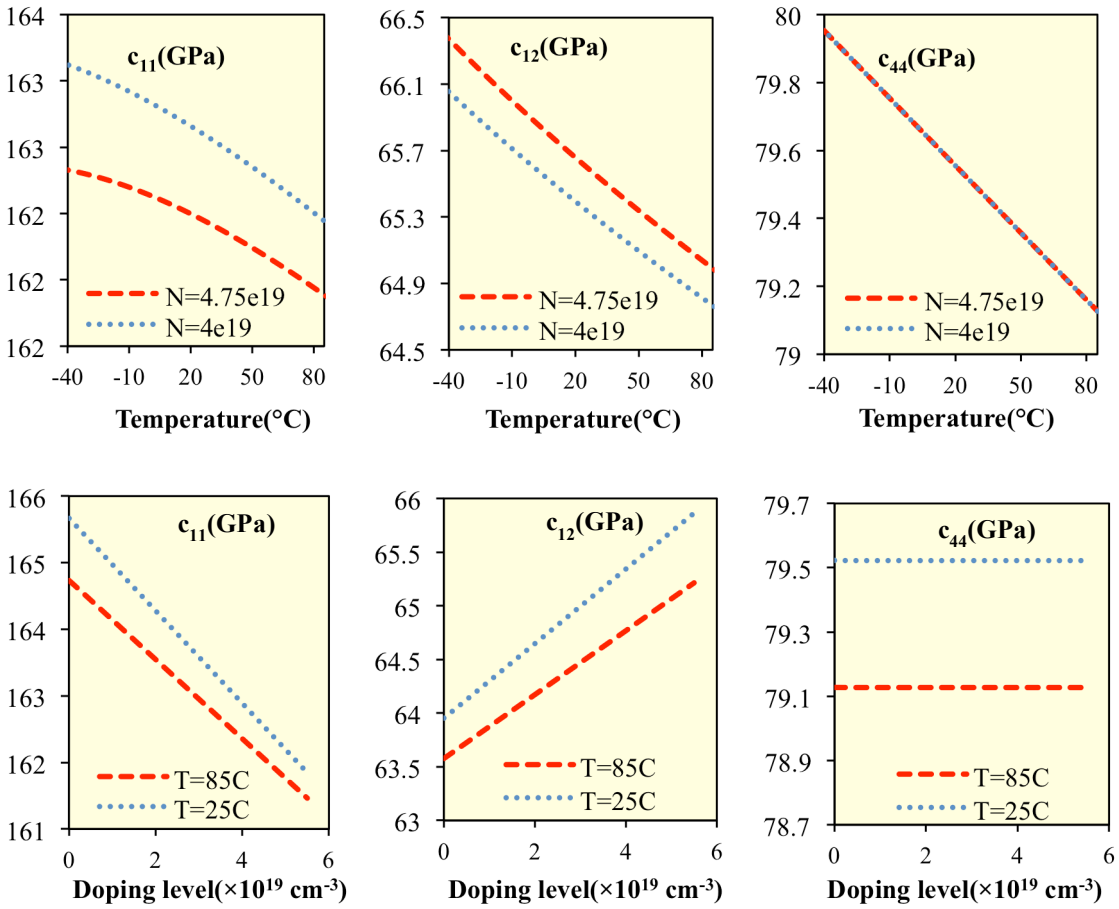

Figure 7-2. The calculated elastic constants vs. temperature for two doping levels (Top) and vs. doping level at two temperatures (Bottom) using Keyes' theory

Using these values and equations (7-1), (7-2) and (7-3), the frequency drift versus temperature is plotted in the figure 7-3 for resonator aligned to both [100] and [110] planes. As it is seen the frequency drift in both planes resembles a parabolic trend showing a turnover point. In addition, the turnover point shifts towards higher temperatures by increasing the doping concentrations. The turnover point is also predicted to occur at much higher temperatures for [100]-aligned resonators.

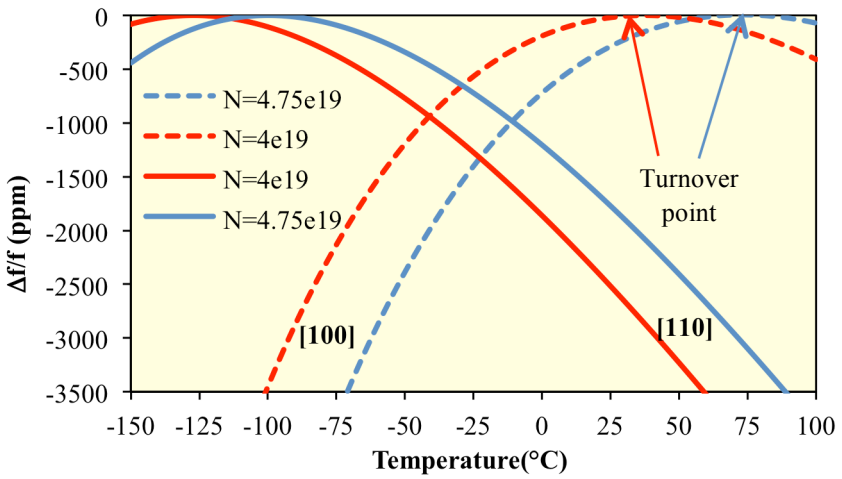

Figure 7-3. The Theoretical temperature-induced frequency variation in resonators aligned to [110] and [100] planes plotted using the predicted elastic constants

7-2) Finite Element Analysis

In order to better predict the frequency drift versus temperature in TPoS resonators a 3D finite element Eigen-frequency simulation is utilized in COMSOL. The simulated structure is made of an 8µm single crystalline silicon slab with 1µm AlN on top. The length and the width of this slab (231µm × 156µm) and the thickness of AlN (1µm) are kept constant throughout this work unless stated otherwise. The elastic constants of n-type doped silicon calculated in the previous section as well as the variation of the Young's modulus vs. temperature in AlN [64] are exploited in this simulation to capture the temperature-induced variation of frequency. The simulated mode-shapes for the same geometry aligned to [110] and [100] crystalline planes for doping concentration of N = 4.75×10^{19} cm^{-3} are shown in figure 7-4.

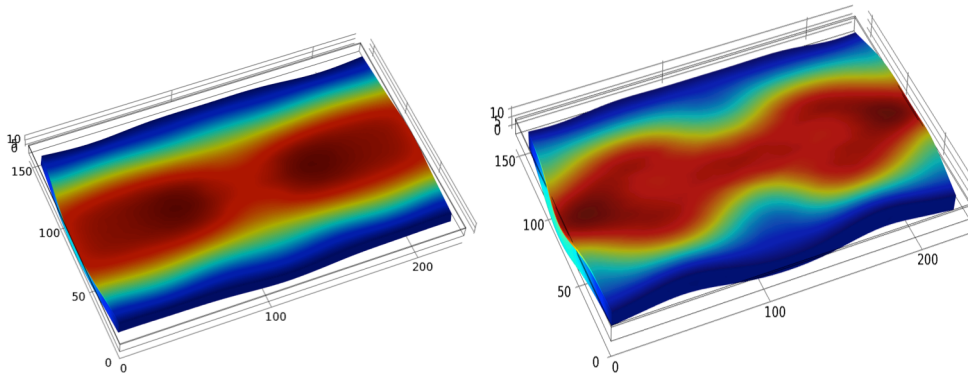

(a) (b)

Figure 7-4. The COMSOL-simulated mode shapes of resonators aligned to (a) [100] and (b) [110] planes for doping concentration of N = $4.75\times10^{19}cm^{-3}$

7-2-1) Effect of doping concentration on TCF

The simulated frequency drift vs. temperature is shown in figure 7-5 for highly doped n-type silicon with doping concentration of N=$4.75\times10^{19}cm^{-3}$ in [100] and [110] planes. The simulated frequency drift vs. temperature for pure silicon is also shown. As it is seen for [110]-aligned devices, the trend is almost linear with an approximately constant TCF of -28ppm/°C and -20ppm/°C for pure and highly doped silicon respectively in the simulated range. On the contrary, for [100]-aligned device the simulated results resemble a parabolic trend with a turnover point. The simulated frequency drift vs. temperature is also shown in figure 7-6 for three different doping concentrations, N=$3.4\times10^{19}cm^{-3}$, $4\times10^{19}cm^{-3}$, and $4.75\times10^{19}cm^{-3}$. The simulation results show that the turnover point shifts to higher temperature as doping concentration increases. Results in figure 7-6 also show that for the targeted silicon and AlN thicknesses, N ~ $4.75\times10^{19}cm^{-3}$ provides the minimum total frequency drift in the temperature range of -40°C to 85°C, where turnover point occurs at the middle of the range. It is interesting to note that the simulated data for the [110] device predicts a closer fit to linear trend compared to the pure theoretical data presented earlier, which is in better agreement with data reported in the following sections.

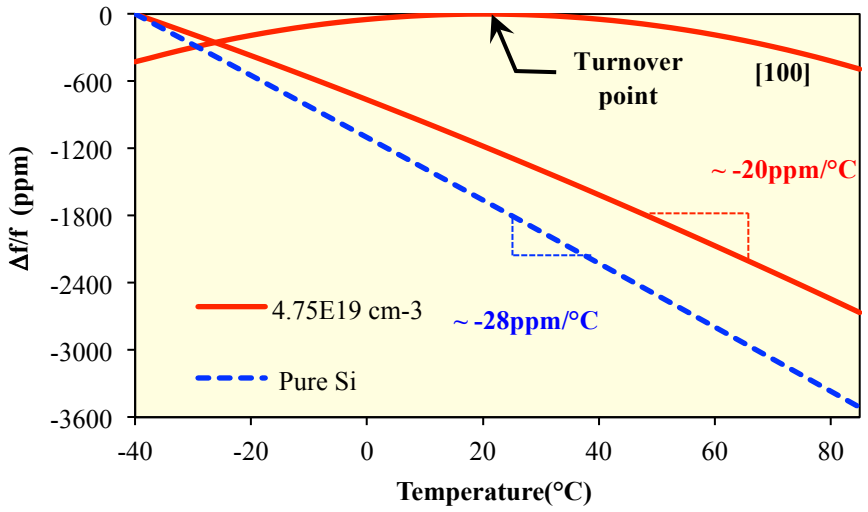

Figure 7-5. The simulated resonance frequency drift versus temperature for TPoS resonators made of pure silicon aligned to [110] plane and n-type doped silicon (N= $4.75\times10^{19}cm^{-3}$) aligned to [110] and [100] planes

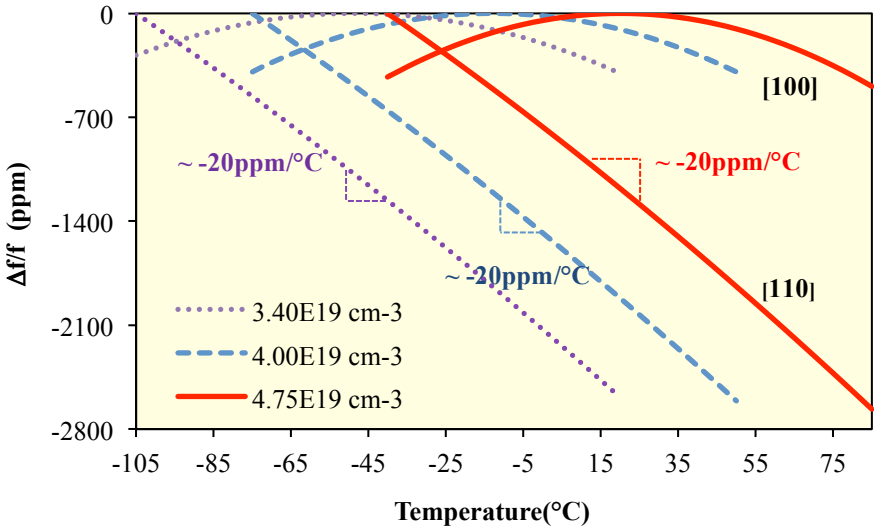

Figure 7-6. The simulated resonance frequency drift versus temperature for n-type doped silicon TPoS resonators aligned to [110] and [100] planes with doping levels of N=3.4×10^{19}, 4×10^{19} and $4.75\times10^{19}cm^{-3}$

The turnover point in devices aligned to [100] silicon plane is calculated and plotted in figure 7-7 for a range of doping levels. As it is seen the turnover point is less sensitive to the doping level at

higher concentrations, which is important in terms of improved manufacturability. Considering this and the fact that for oven-controlled oscillators the turnover point has to be designed at temperatures higher than 90ºC, therefore a doping concentration of N~10^{20} cm^{-3} is desired for such applications. In this work the selected doping levels are imposed by the availability of such substrates and are less than the desired value.

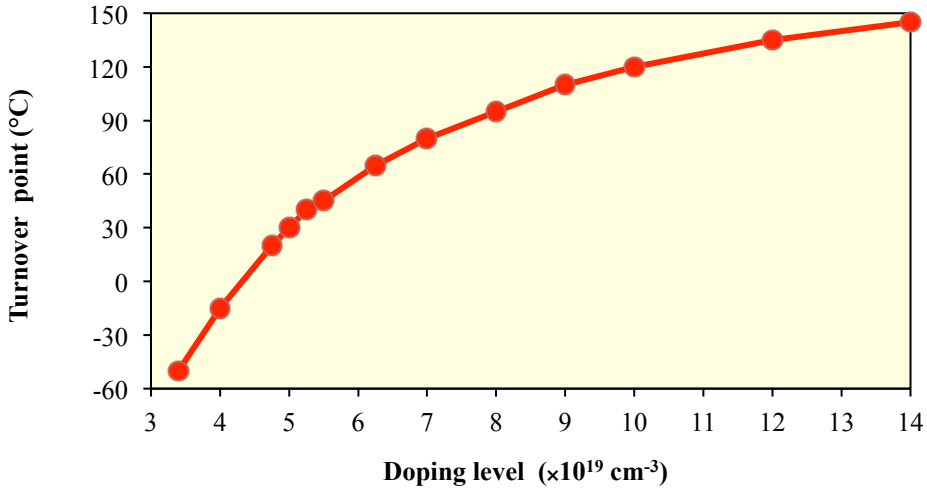

Figure 7-7. The simulated turnover point versus doping level for n-type doped TPoS resonator aligned to [100] plane

7-2-2) Effect of AlN on TCF

The temperature-induced frequency drift for a resonator comprised of 8µm of n-type doped [100]-aligned silicon (N = $4.75\times10^{19}cm^{-3}$) and a resonator comprised of 1µm of AlN are simulated using COMSOL. The results are depicted in figure 7-8 and are compared to a resonator consisting of both films stated above. It is observed that the turnover point for the silicon resonator is around 40°C. On the other hand, frequency variation versus temperature is linear for AlN resonator with a TCF of ~ -18.3ppm/°C. As it is seen the AlN stack shifts the turnover point of AlN-on-silicon resonator down to ~20°C.

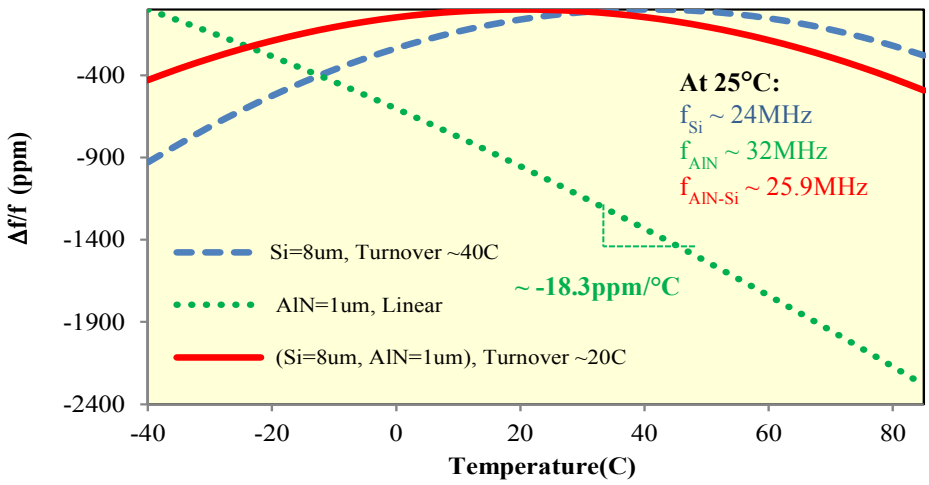

Figure 7-8. The simulated resonance frequency drift versus temperature for [100] -aligned only–silicon (N=4.75×$10^{19}$$cm^{-3}$), only-AlN, and AlN-on-silicon (N=4.75×$10^{19}$$cm^{-3}$) resonators

7-2-3) Effect of silicon thickness on TCF

In order to investigate the effect of the silicon thickness on TCF, the finite element simulation was repeated for an AlN-on-silicon resonator aligned to [110] and [100] planes with three different silicon thickness without changing the AlN thickness (1µm) and doping concentration (figure 7-9, figure 7-10). Results (figure 7-10) show that the turnover point shifts to higher temperature when the silicon thickness increases. These results are consistent with the simulation results of figure 7-8 in which the addition of AlN caused the turnover point to shift downward (the thicker the silicon the closer the turnover point to the value simulated for pure silicon).

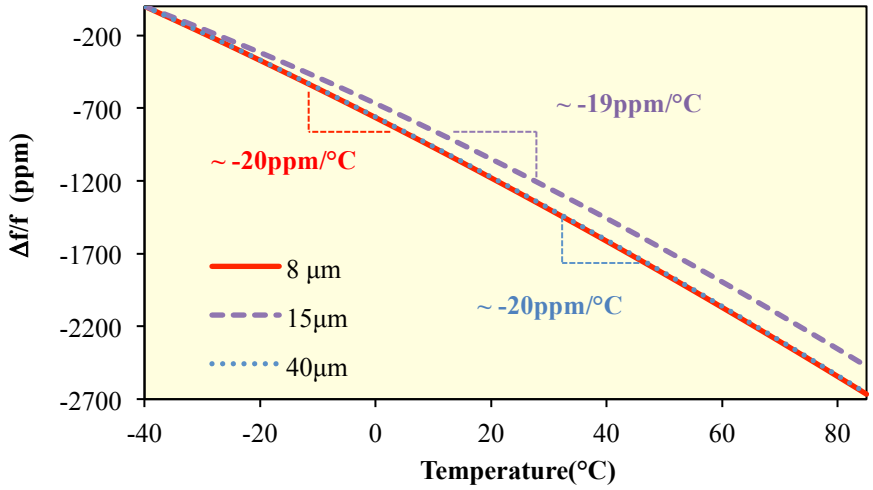

Figure 7-9. The simulated resonance frequency drift vs. temperature of a resonator aligned to [110] plane with different silicon thickness (doping level N=4.75×$10^{19}$$cm^{-3}$)

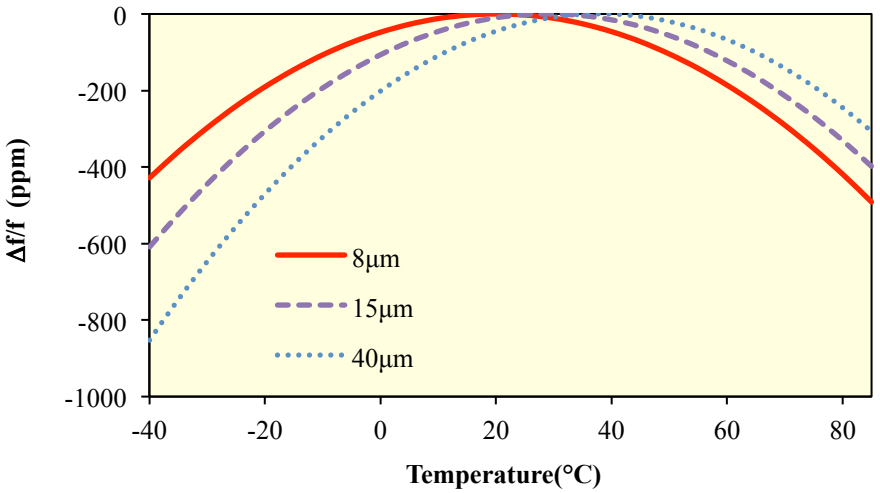

Figure 7-10. The simulated frequency drift vs. temperature of TPoS resonator aligned to [100] plane with different silicon thickness (doping level N=4.75×$10^{19}$$cm^{-3}$)

Moreover, we extend our study to higher order resonance modes. In figure 7-11 we are presenting the temperature-induced frequency drifts for the first- and third-order modes of the studied resonator. The resonance frequencies are at 25.9MHz and 77MHz respectively. Furthermore, a second resonator with the same resonant structure is designed to have a first order resonance at approximately 77MHz (the width of the device is scaled down by a third).

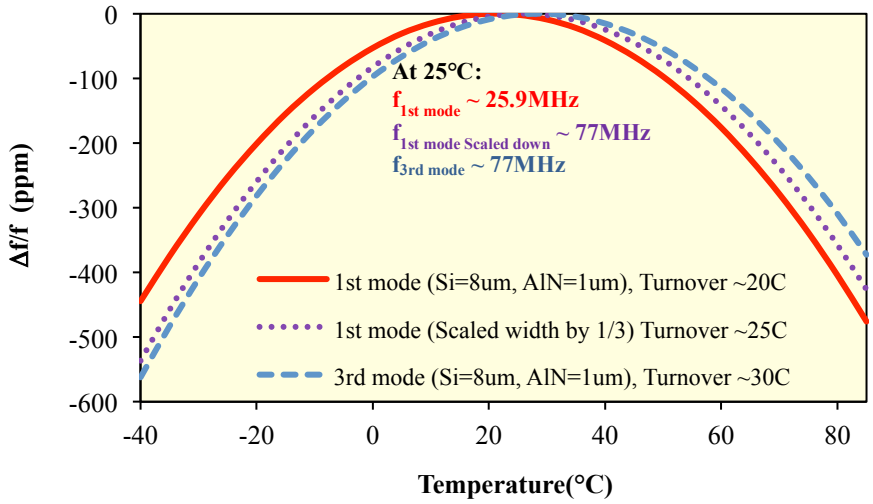

Figure 7-11. The simulated resonance frequency drift vs. temperature of 1st and 3rd modes for TPoS resonator aligned to [100] plane with doping level of $N=4.75\times10^{19}cm^{-3}$

As it is seen, the turnover point for the third harmonic is higher than that of the first harmonic. It is also higher than the turnover point for the scaled first harmonic device. This suggests that for a target resonance frequency the turnover temperature can be varied not only by changing the thickness of the silicon substrate but also the resonance mode number.

7-3) Design and fabrication

In order to experimentally validate the predictions, three [100] SOI wafers with different device thicknesses, dopant types, and doping concentrations were used in this work (Table I). Similar resonators are fabricated on each of these wafers oriented in two different crystalline planes; [110] and [100]. Note that the starting substrate in all of our experiments is [100] SOI wafers. Therefore resonators aligned to the wafer flat are oriented in the [110] plane. By rotating the resonator 45° in-plane the device will be aligned to [100] plane (figure 7-12).

Table 7-1. The device silicon properties for the utilized SOI wafers.

Thickness (μm)	Dopant(n-type)	Resistivity (Ω cm)	Doping Concentration (cm^{-3})
8	P	~0.0015	$\sim5\times10^{19}$
15	As	~0.0024	$\sim3.4\times10^{19}$
40	P	~0.0015	$\sim5\times10^{19}$

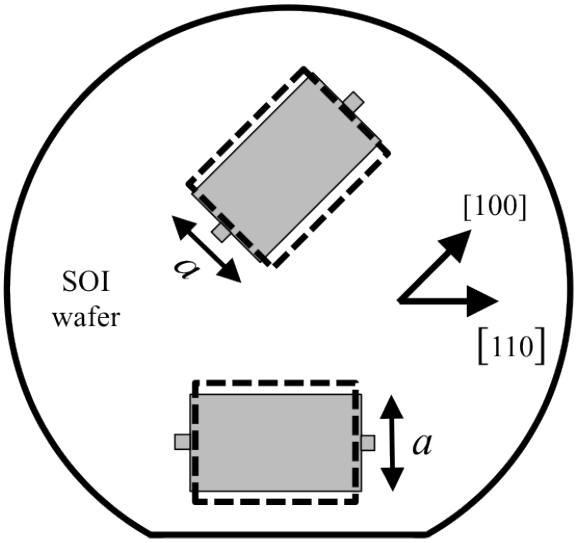

Figure 7-12. The schematic of TPoS designs aligned to [110] and [100] planes in SOI wafer

7-4) Measurement

The lateral-extensional mode TPoS resonators are fabricated using a five-mask process flow briefly described before. A more detailed discussion of the processing steps can be found in [18].

7-4-1) Measurement setup

The TCF measurement is conducted in a Janis cryogenic vacuum probe station (vacuum required to prevent the condensation at low temperatures) using high-frequency probes and Agilent E5061A ENA network analyzer (figure 7-13). The sample holder is cooled by liquid nitrogen and heated with a resistive heater and the temperature is controlled by a PID controller within ±0.05°C.

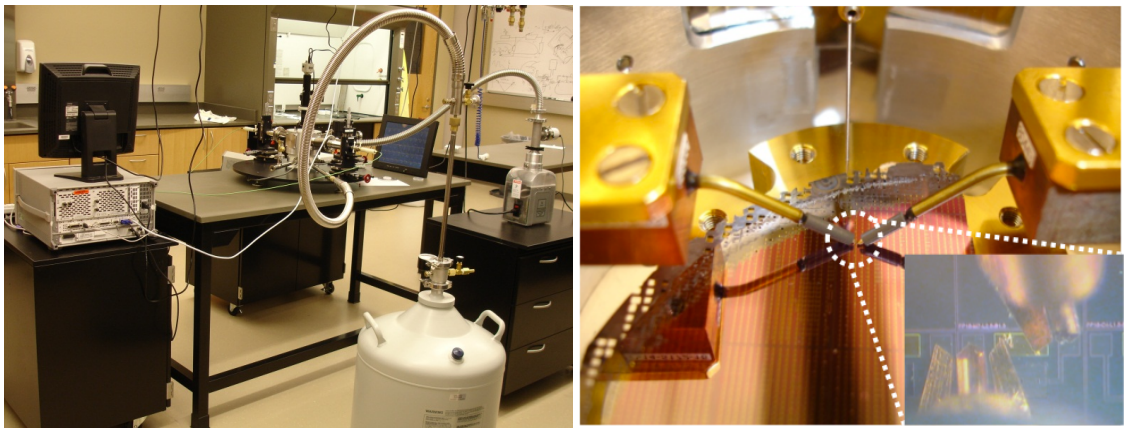

(a) (b)

Figure 7-13. a) TCF measurement setup; b) Contacted probes on the device pads inside the chamber

7-4-2) Results

7-4-2-1) Effect of doping concentration and design orientation on TCF

The frequency responses of the fabricated devices comprising 8µm Phosphorous doped silicon and 1µm AlN were measured in air (figure 7-14). Resonance frequency in [100]-aligned devices is lower than the [110]-aligned resonators as expected due to the lower Young's modulus (~130GPa vs. ~170GPa) and as it is seen the quality factor and motional impedances are comparable.

Temperature characterization of frequency was conducted in Janis cryogenic vacuum probe station. The measured ppm variations of resonance frequency versus temperature for three different resonators with similar geometrical designs are compared in figure 7-15. The effect of orientation and increased doping concentration is clearly observed and is in good agreement with our predictions. As it is seen, the TCF measured for [110]-aligned resonators is approximately constant and is almost -17ppm/°C compared to -28.6ppm/°C for the lightly doped (less than $1\times10^{16}cm^{-3}$) silicon resonator, which shows 40% improvement. However, the more important measurement result is seen for the highly doped [100]-aligned device where a parabolic trend is observed with a turnover point at ~20°C which is in good agreement with our predictions. The

overall frequency variation over the range of -40°C to 85°C for the [100]-aligned device on highly-doped silicon is less than 245ppm which shows 8 times reduction compared to overall frequency variation of around 2000ppm for the [110]-aligned device. Although, this is still higher than the total frequency drift of AT-cut quartz resonator, it's a 15 times reduction compared to a more than 3550ppm frequency drift reported for a conventional [110]-aligned silicon resonator.

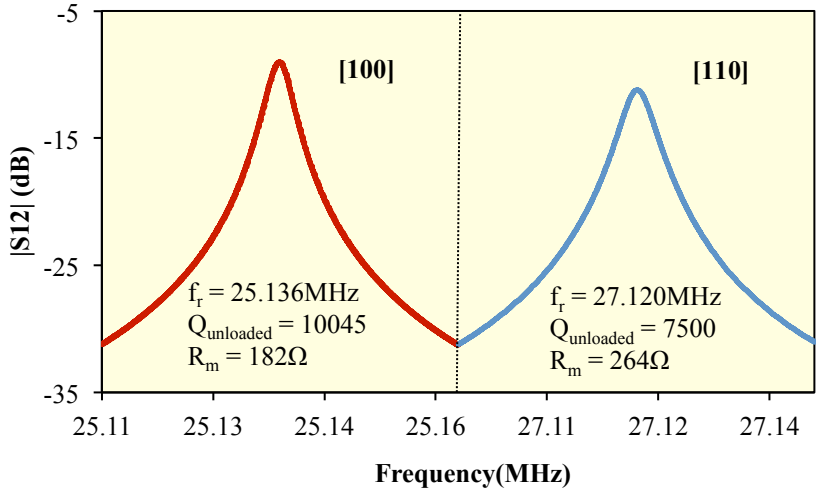

Figure 7-14. The measured frequency response for devices aligned to [100] and [110] planes (8µm Phosphorous doped silicon and 1µm AlN)

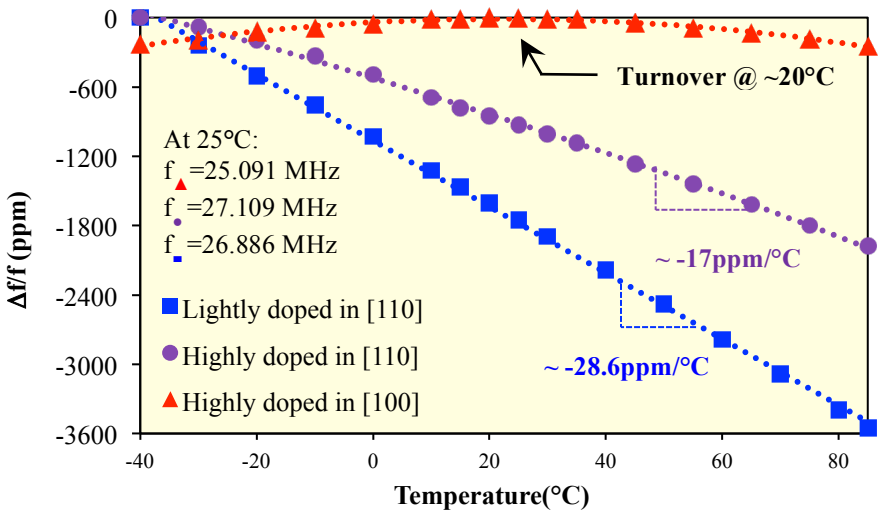

Figure 7-15. The measured resonance frequency drift vs. temperature for TPoS resonators with pure silicon aligned to [110] plane and n-type doped silicon (N= $4.75\times10^{19}cm^{-3}$) aligned to [110] and [100] planes

The measured ppm variations of resonance frequency versus temperature for 8µm Phosphorous and 15µm Arsenic doped device aligned to [110] and [100] planes are also shown in figures 7-16 and 7-17. As it is seen from figure 7-16, the TCF measured for [110]-aligned resonators is approximately constant and is almost -17ppm/°C and in good agreement with our prediction. It is also seen from figure 7-17 that fitted curves are parabolic for [100] plane. Moreover, the turnover point of the As-doped device is around -45°C while it is around 20°C for P-doped device. This is also in agreement with the theoretical prediction.

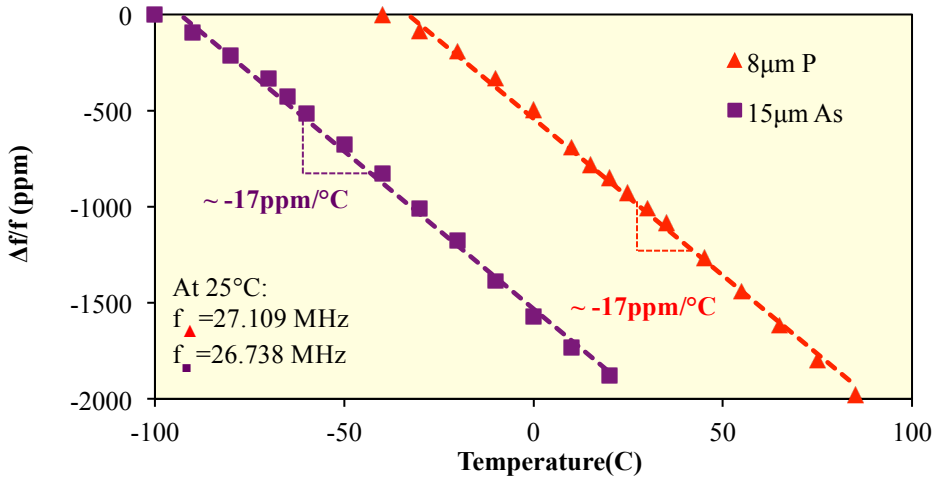

Figure 7-16. The measured resonance frequency drifts vs. temperature for P-doped and As-doped TPoS resonators aligned to [110] plane

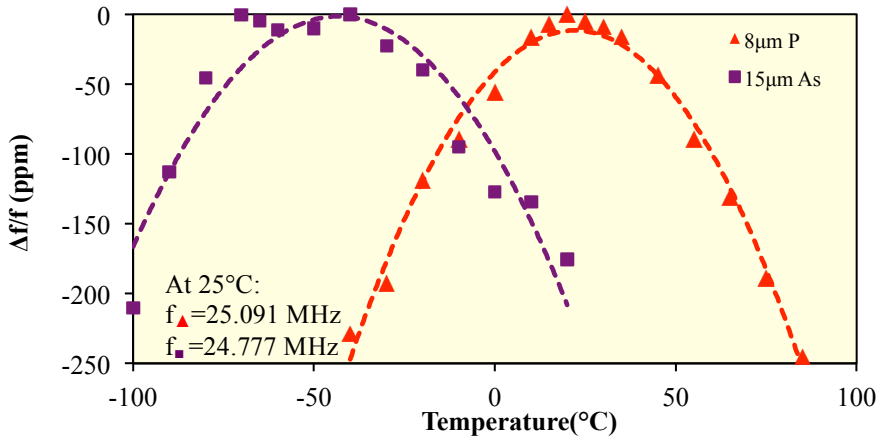

Figure 7-17. The measured resonance frequency drifts vs. temperature for P-doped and As-doped TPoS resonators aligned to [100] plane

7-4-2-2) Effect of silicon thickness

The resonance frequency is measured over the temperature range of -40 to 85°C for the devices fabricated on 8µm and 40µm substrates and aligned to both [110] and [100] planes. The results are plotted in figures 7-18 and 7-19. The difference between the turnover points of the [100]-aligned 8µm resonator (20ºC) and the 40µm device (35ºC) is believed to be a result of the thickness difference. Therefore, the prediction in figure 7-10 is experimentally validated by the data presented in figure 7-19. Results validates that the turnover point shifts to the right as the device thickness and the doping concentration increases.

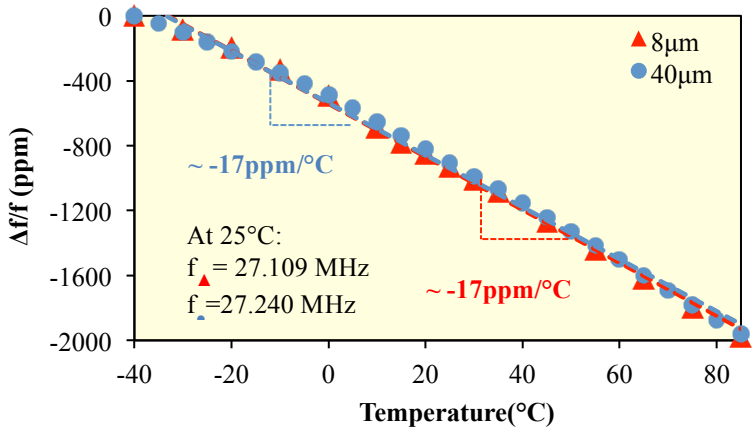

Figure 7-18. The measured resonance frequency drifts versus temperature for TPoS resonators aligned to [110] plane with varying thicknesses

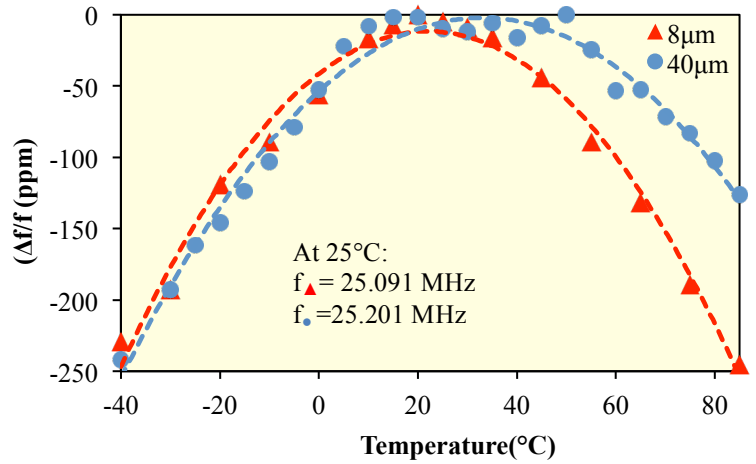

Figure 7-19. The measured resonance frequency drifts vs. temperature for TPoS resonators aligned to [100] plane with varying thicknesses

Also the ppm variations of resonance frequency versus temperature are measured for 1st and 3rd modes over the range of -40 to 85ºC (figure 7-20). The difference between the turnover points of the 1st mode [100]-aligned 8µm resonator (~20ºC) and the 3rd mode (30ºC) is in agreement with the trend predicted by the simulation (figure 7-11). This is believed to be a result of the difference in the contribution of silicon thickness in the resonance mode as the acoustic wavelength varies for the 3rd harmonic compared to the 1st harmonic.

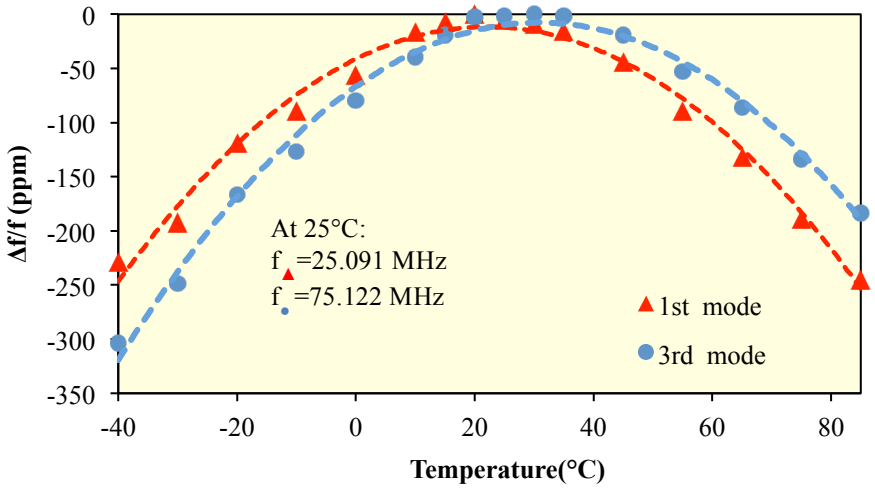

Figure 7-20. The measured resonance frequency drifts vs. temperature of 1st and 3rd modes of TPoS resonators aligned to [100] plane

The first and second order temperature coefficients of frequency for all of the characterized devices in this work are shown in table 7-2.

Table 7-2. The first and second order temperature coefficients of frequency of characterized devices

Device/mode	Plane	First order (ppm/°C)	Second order (ppb/°C^2)
Si=8 µm (P-doped),1st mode	[110]	-16.3	-24.5
Si=8 µm (P-doped),1st mode	[100]	-	-61
Si=8 µm (P-doped),3rd mode	[100]	-	-62
Si=15 µm (As-doped),1st mode	[110]	-16.4	-30
Si=15 µm (As-doped),1st mode	[100]	-	-51
Si=40 µm (P-doped),1st mode	[110]	-16.2	-31
Si=40 µm (P-doped),1st mode	[100]	-	-48

CHAPTER VIII

TEMPERATURE COMPENSATION IN MIXER-ENABLED MEMS OSCILLATORS

In this chapter, MEMS oscillators with controlled temperature coefficient of frequency (TCF) are introduced through mixing the frequencies of two oscillators that are made of silicon micro-resonators with known and dissimilar TCF. Based on this method, a ~6MHz oscillator is assembled in which the first-order TCF is virtually cancelled resulting in a parabolic TCF curve yielding less than 90ppm frequency shift over 25-85°C.

As it was mentioned before, the temperature compensation of silicon-based oscillators has been attempted through active (e.g. frequency correction) and passive techniques (e.g. altering the TCF of silicon through doping or inclusion of oxide). Although these techniques successfully enable low temperature-induced frequency drift, they either require an accurate measurement of temperature or add complexity to the fabrication process. In contrast, the technique proposed in this work, is a simple circuit-level method that takes advantage of the adjustable TCF and frequency in silicon resonators.

The general concept is shown in the block diagram of figure 8-1 where two resonators with different TCF are incorporated into two oscillators, their outputs are mixed after multiplying by a scale factor (N and M), and the output is properly filtered to remove undesirable harmonics. It can

be shown that the first-order TCF of the output (f: desired frequency) can be derived in terms of the first-order TCFs' and the oscillation frequencies of the sub-oscillators from the equation below (Appendix I):

$$TCF_f = \frac{N \times TCF_{f1} \times f_{1@T0} \pm M \times TCF_{f2} \times f_{2@T0}}{N \times f_{1@T0} \pm M \times f_{2@T0}} \qquad \text{where, } f = Nf_1 \pm Mf_2 \text{ and } T0 \text{ is the reference temperature}$$

Therefore, the TCF of the output can be designed by properly choosing the oscillation frequency and the TCF of the two sub-oscillators as well as the N and M scaling factors. For example, an oscillator with virtually zero first-order TCF can be assembled by designing the numerator of the above equation to be zero.

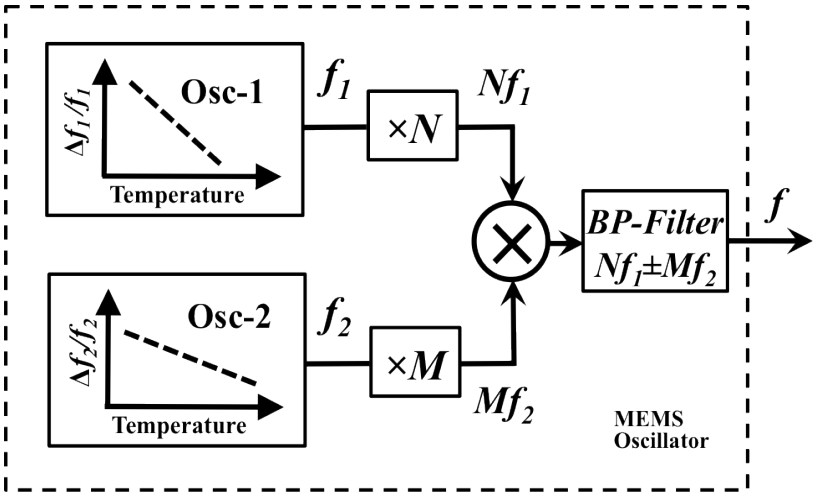

Figure 8-1. Block diagram of the proposed controlled-TCF MEMS oscillator

Thin-film piezoelectric-on-silicon (TPoS) resonators (figure 8-2) are used in this configuration to demonstrate the proposed idea. As it was mentioned in chapter 3, the frequency of the lateral-extensional TPoS resonators can be designed by varying the device width. Also, by varying the doping type/concentration of silicon the TCF of the resonator can be altered (chapter 7). For instance, the TCF in n-type-doped silicon resonators are simulated at 4 different doping concentrations in a finite element software package (COMSOL) and plotted in figure 8-3. In this

study, three resonators are utilized. A 26.2MHz resonator comprised of a 30μm lightly p-type-doped Si layer (figure 8-4), a 32.48MHz resonator comprised of a 5μm moderately p-type-doped Si layer (figure 8-5), and a 25.8MHz resonator comprised of a 8μm highly n-type-doped Si layer oriented in [110] direction (figure 8-6). TCFs of these resonators are characterized to be around -30.7ppm/°C, -24.8ppm/°C, and -17.6ppm/°C respectively. These resonators are used as one port device in three separate oscillators based on the schematic in figure 8-7. The schematic in figure 1 is implemented by utilizing the assembled oscillators, a passive mixer (ZS05-2-S from Mini-Circuits), and proper filter. The temperature dependency of the oscillation frequency is measured in the environmental chamber (figure 8-7).

Using two 32.48MHz and 26.2MHz MEMS oscillators (N=M=1), a 6.28MHz frequency with a linear TCF of ~+0.3ppm/°C is obtained at the output (figure 8-8). The measured total frequency drift is less than 90ppm over 25-85°C. With this oscillator there is no need to actively measure the temperature and tune the frequency, which are practiced in the majority of today's temperature-stable oscillators. Moreover, using the 26.2MHz and 25.8MHz MEMS oscillators a 400kHz waveform with a linear TCF of ~ -850ppm/°C is obtained at the output (figure 8-9). This amount is equal to ~ 340Hz/°C, which is suitable for a very accurate temperature sensor.

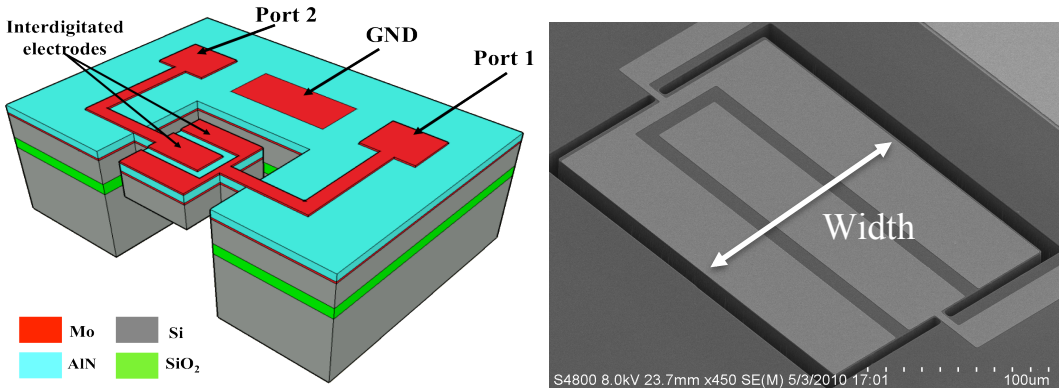

a) b)

Figure 8-2. a) Schematic and b) SEM of a TPoS resonator

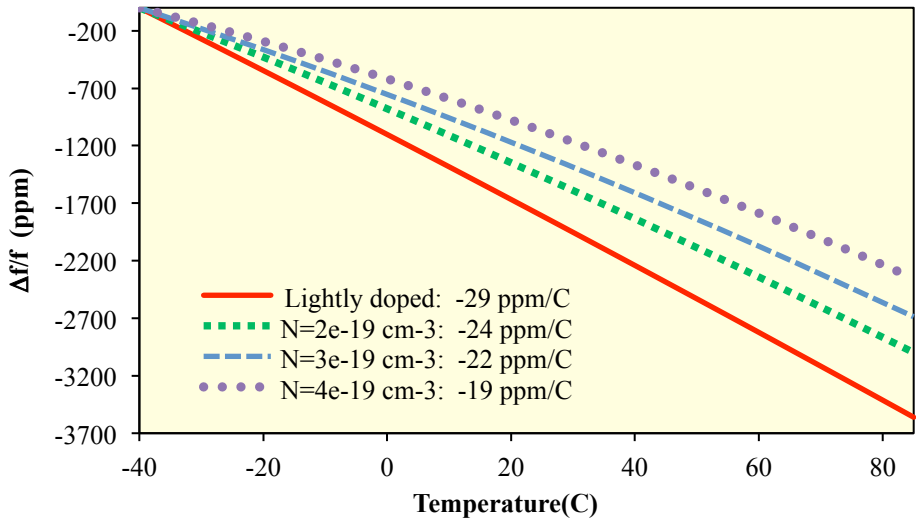

Figure 8-3. Simulated TCF of n-type-doped silicon resonators for 4 different doping concentrations using COMSOL

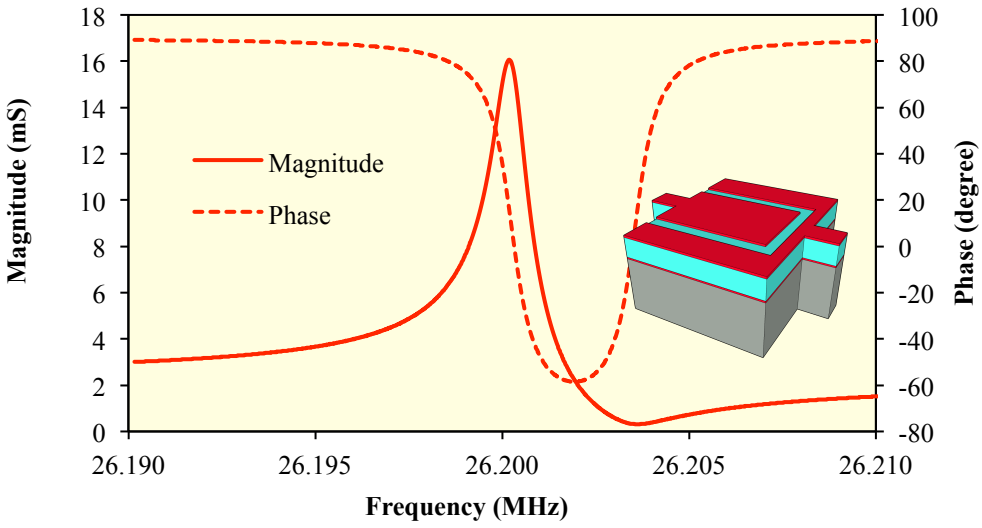

Figure 8-4. A-f response of the 30 μm p-type-doped Si TPoS resonator; R_m~62Ω, Q~26900

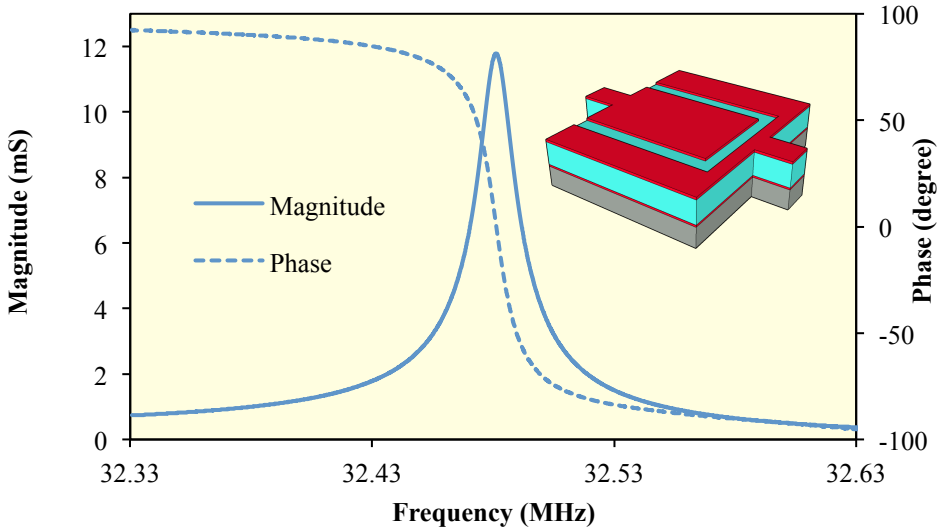

Figure 8-5. A-f response of the 5 μm p-type-doped Si TPoS resonator; R_m~85Ω, Q~2100

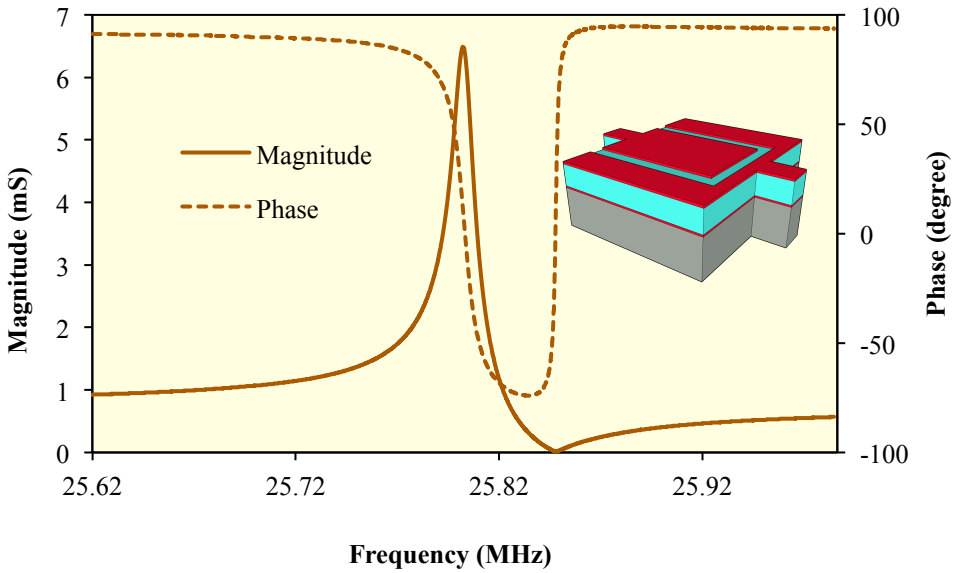

Figure 8-6. A-f response of the 8 μm n-type-doped Si TPoS resonator; R_m~154Ω, Q~1900

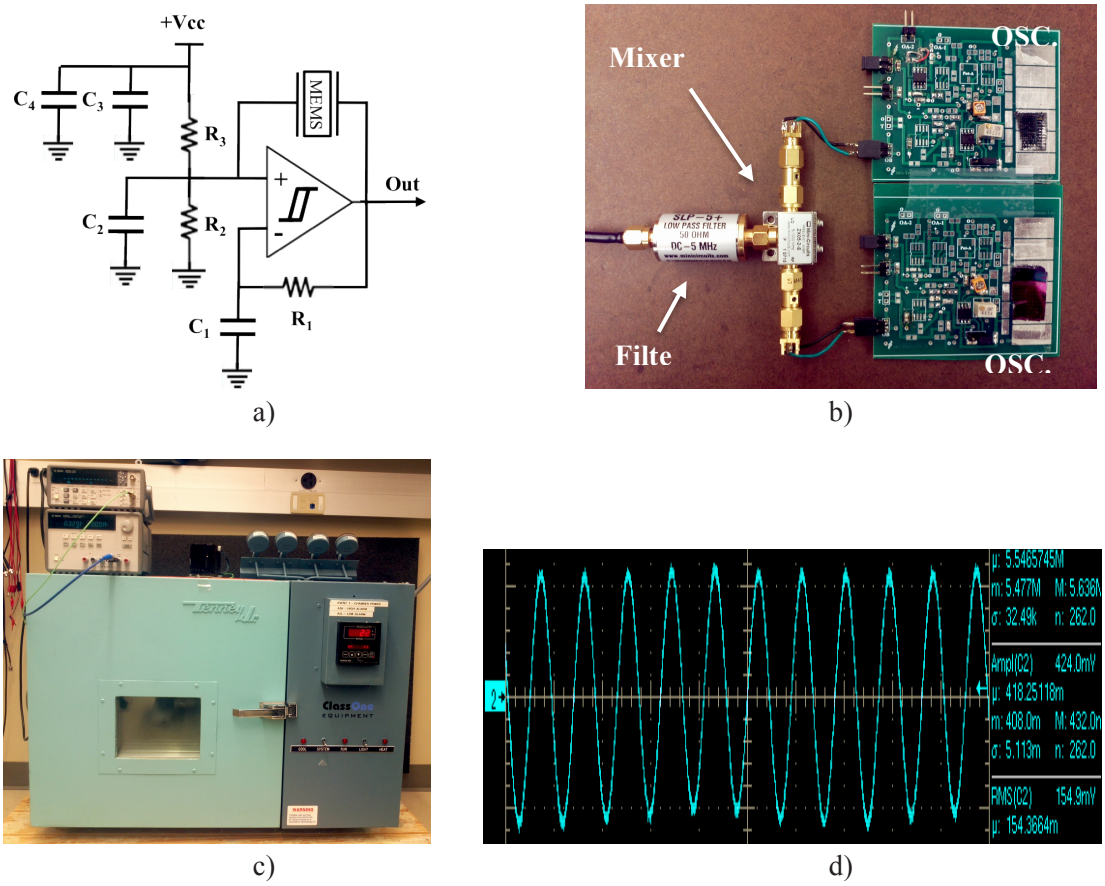

Figure 8-7. a) Circuit schematic, b) Assembled oscillator, c) Environmental chamber, and d) Output waveform for the ~ 6MHz oscillator

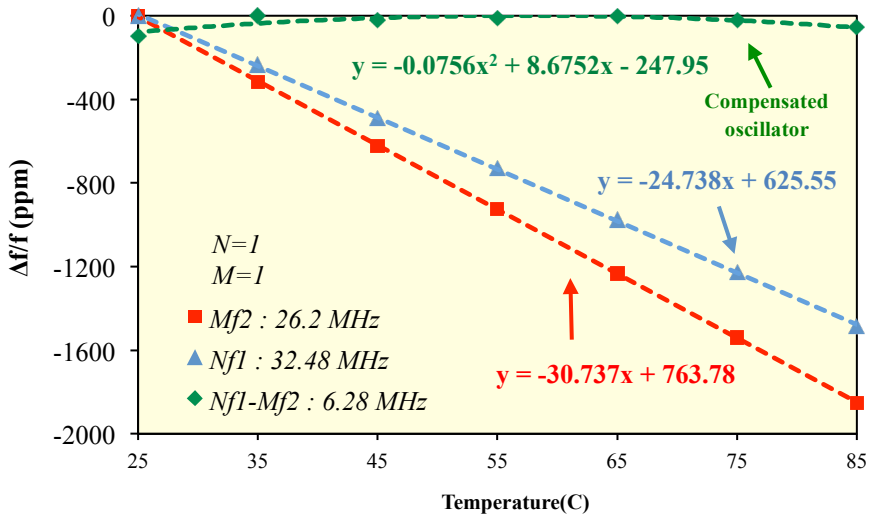

Figure 8-8. Measured resonance frequency drift vs. temperature of two MEMS oscillators and the temperature compensated output

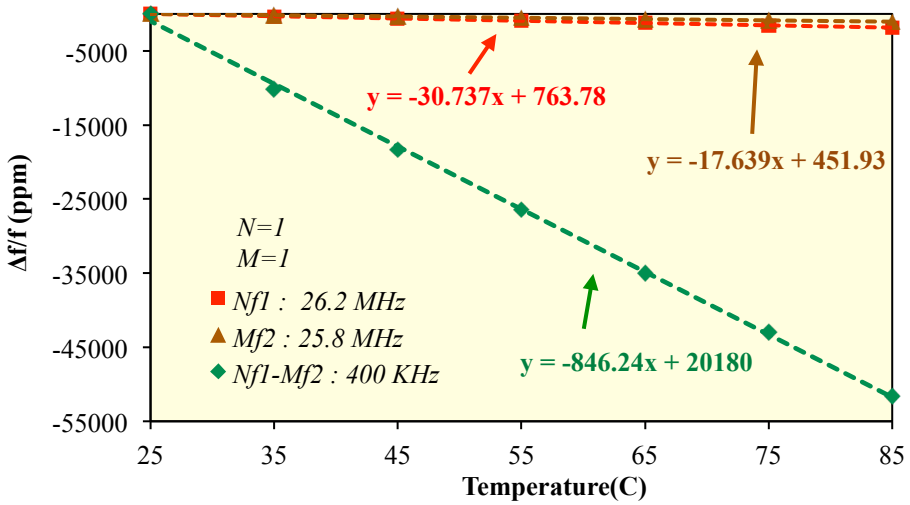

Figure 8-9. Measured resonance frequency drift vs. temperature of two MEMS oscillators, and the output designed for the temperature sensor application

CHAPTER IX

PASSIVE TUNING IN TPOS RESONATORS

Resonance frequency of a resonator is subject to change by several causes and factors. These factors consist of fabrication process, aging, temperature dependency and other environmental conditions. Generally, MEMS resonator tuning techniques are classified into two major categories: technics, which tune the resonators frequency as one-time by permanent changes in the device, and those, which perform the tuning temporarily based on the necessaries. Permanent tuning can be done by drilling or laser trimming. However, the tuning in the second category is performed by altering temporarily the resonator characteristics, which determine the resonance frequency and varies in different technologies.

In capacitive resonators, frequency tuning is usually pursued through altering the effective stiffness of the resonator by varying the bias voltage across the parallel plate capacitive transducer [49], [65]. In these resonators effective tuning at high frequencies (10's of MHz and above) is only achievable with very small transduction gaps and large tuning voltages, rendering the technique impractical. Tuning based on heating the resonant structure has also been studied in the past [66], [67]. The drawback is that although the frequency stability achieved in such scheme can be considerable, but the large power consumption is prohibitive for all battery-powered applications.

Although, lateral-mode piezoelectric resonators such as TPoS devices have been successfully incorporated in low-power and low-noise oscillators, they have limited frequency stability versus temperature (relatively large temperature coefficient of frequency, TCF). Also, methods of frequency tuning have not yet been studied extensively for such devices. Simple and effective tuning schemes can be exploited in temperature compensated oscillators.

In this chapter the well-known concept of altering the mechanical stiffness of a vibrating piezoelectric film through varying the electrical impedance connected to the conducting electrodes is used for TPoS resonator tuning. By changing the mechanical stiffness resonance frequency is changed. The novelty of this idea is in separating the tuning port from the signal port, which will be included in the oscillation loop. This way the termination impedance can be altered to the extremes (open and short) without largely affecting the oscillation loop and therefore the tuning range is expanded. The effect of the resonator design features such as tuning electrode position, relative electrode sizes, and relative thicknesses of the layers in the resonant structure on the maximum achievable frequency tuning is experimentally investigated.

The dependency of frequency tuning on the design features of the resonator is studied as well. The potential application of the tuning technique in temperature compensated oscillators is also demonstrated.

9-1) Theory of passive frequency tuning in TPoS resonators

It is known that the effective modulus of a piezoelectric layer (and consequently the resonance frequency) can be altered by varying the shunt impedance connected to a pair of conductive electrodes that cover the surfaces of the film [68] [69] . As shown in figure 9-1 the modulus will change between a minimum at short termination and a maximum at open termination as the parallel impedance is varied. For a short termination the effective modulus (E_{Short} in figure 9-1) depends only on the material compliance (S^E) while for other terminations it is a function of not

only the material compliance but also the piezoelectric properties and the shunt impedance (d, ε_p , Z_T and Z_p). In figure 9-1, E is the effective modulus, d is piezoelectric constant, ε_p is the permittivity of piezoelectric material and Z_T and Z_p are shunt impedance and the capacitive impedance of conductive electrodes respectively.

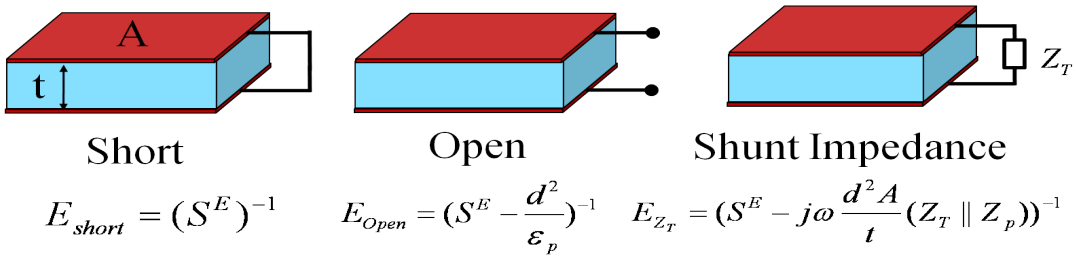

Figure 9-1. Dependency of the effective modulus of a metalized piezoelectric film on the electrical termination

This concept is exploited in the lateral-mode TPoS resonators. The proposed configuration for the frequency tuning purpose is shown in figure 9-2. One of the two terminals in the two-port resonator (port 2) is designated to tuning. Varying the shunt impedance (Z_T) connected to this port changes the effective modulus of the resonant body and the minimum and maximum impedance determines the resonance frequency limits. The other port (port 1) will then be connected to the oscillator circuit. To investigate the tuning range the reflection S-parameters (S11) are measured from port one as the second port is either floating (creating open termination) or connected to a 50Ω terminated probe (mimicking close to a short termination). The resonator impedance is then calculated from the measured S11 data.

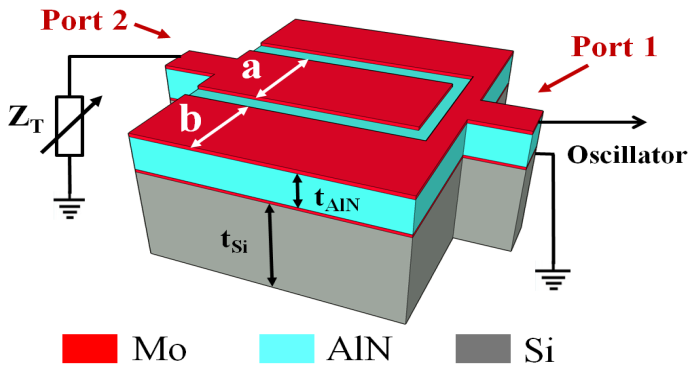

Figure 9-2. The proposed TPoS resonator electrode configuration for passive tuning purposes

9-2) Design and measurement results

9-2-1) Tuning in TPoS Resonators

TPoS resonators with various electrode pattern were fabricated on SOI wafers with different silicon thicknesses for characterization of the tuning range. Two sets of pure AlN devices [18] were also fabricated on bare silicon wafers with 1.5 and 2µm thick AlN film for comparison. The frequency response of a 29MHz fundamental-mode resonator is shown in figure 9-3. This design is fabricated on a SOI wafer with 5µm silicon and 2µm AlN. The impedance vs. frequency plot is calculated from the measured reflection S-parameter (S11). Measurement is repeated for two cases; 50Ω (close to short) and open termination at port two. The results are plotted in figure 9-4. As seen in this figure the resonance frequency is shifting more than 116kHz at ~29MHz (4000ppm) between short and open case. It is observed that the attributes of the measured frequency response other than the resonance frequency are also affected by the termination on the tuning port (e.g. the Q is higher for the open termination). However, the change is not significant to an extent that could disrupt the operation of an oscillator circuit.

As it will be discussed in the next few sections the maximum achievable tuning range is a function of electrode position, electrode size and relative Silicon to AlN thickness.

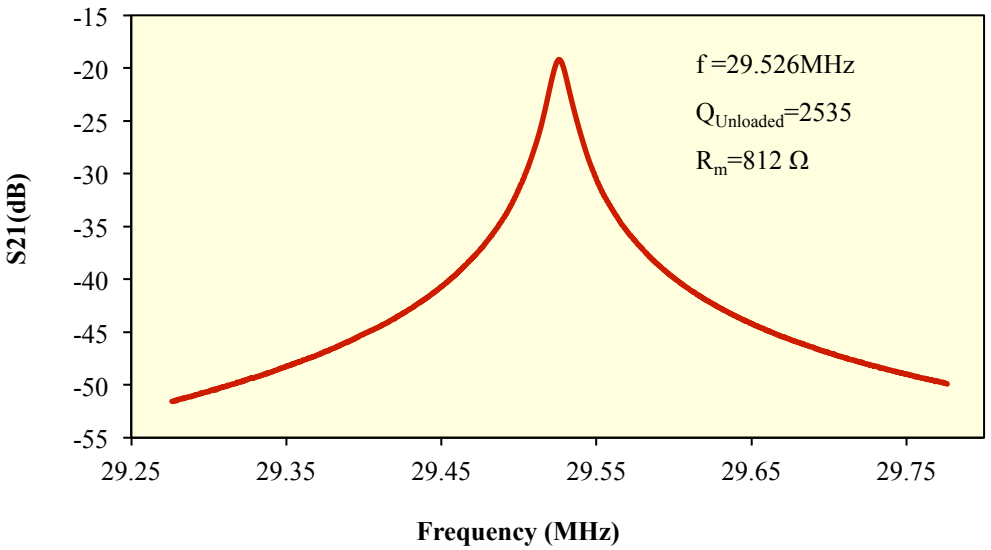

Figure 9-3. Measured frequency response of a TPoS resonators with a/b=4, Silicon thickness = 5µm, AlN thickness= 2µm

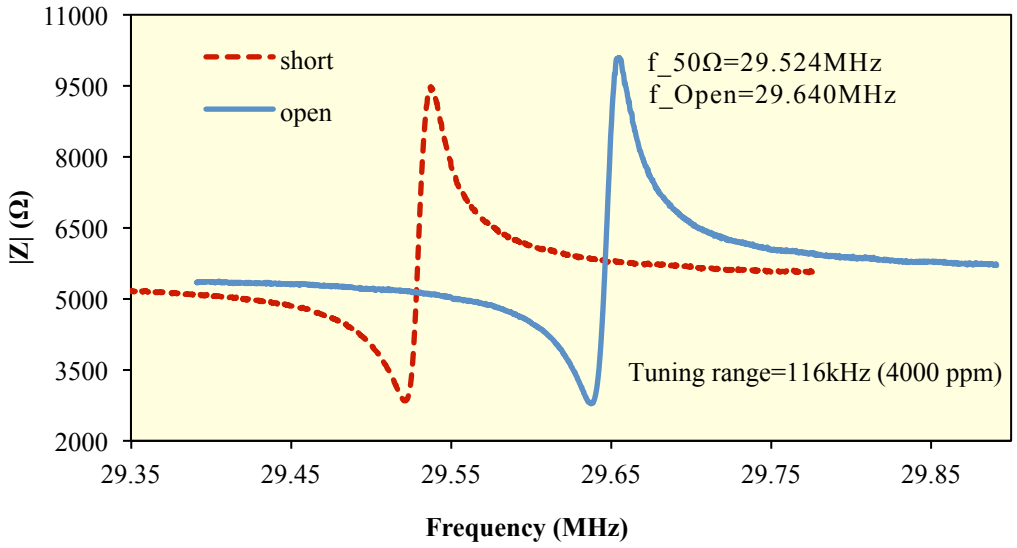

Figure 9-4. The measured frequency shift for the device above on probe station

9-2-1-1) Effect of electrode position

The effect of the electrode position on tuning range is studied by measuring the tuning range for two cases. First; port two is used as tuning and S11 measurement is done at port one and next; the

configuration is reversed. It is observed that a larger frequency shift is achieved by utilizing the center electrode (port two) for tuning versus port one. For example the tuning results for the device tested above are shown in Table 9-1. This observation can be explained by the fact that the center electrode covers the area that undergoes the maximum stress in fundamental mode as shown in the simulated mode-shape of figure 9-5. Therefore the contribution of the center area on the overall effective modulus of the structure is larger.

Table 9-1. Measured frequency tuning of a TPoS resonators with a/b=4, Silicon thickness = 5µm, AlN thickness= 2µm

		Frequency(MHz)	**Tuning Range(ppm)**
Tuning Port: 2	Short	29.524	4000
	Open	29.640	
Tuning Port: 1	Short	29.524	340
	Open	29.534	

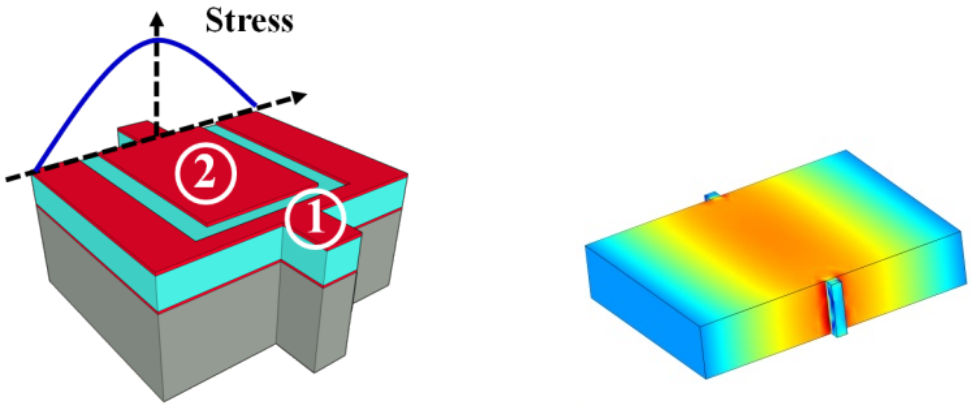

a) b)

Figure 9-5. a) Schematic and b) COMSOL simulation result of the stress profile along the width of a fundamental-mode resonator

9-2-1-2) Effect of electrode size

Several TPoS resonators with different ratios of the center electrode to the side electrode width (a/b) were fabricated and tested. Results show that the frequency tuning range increases as this ratio increases. As it is depicted in figure 9-6 it varies from 1000ppm to 4300ppm for "a/b" ratio of 0.7 to 10.8.

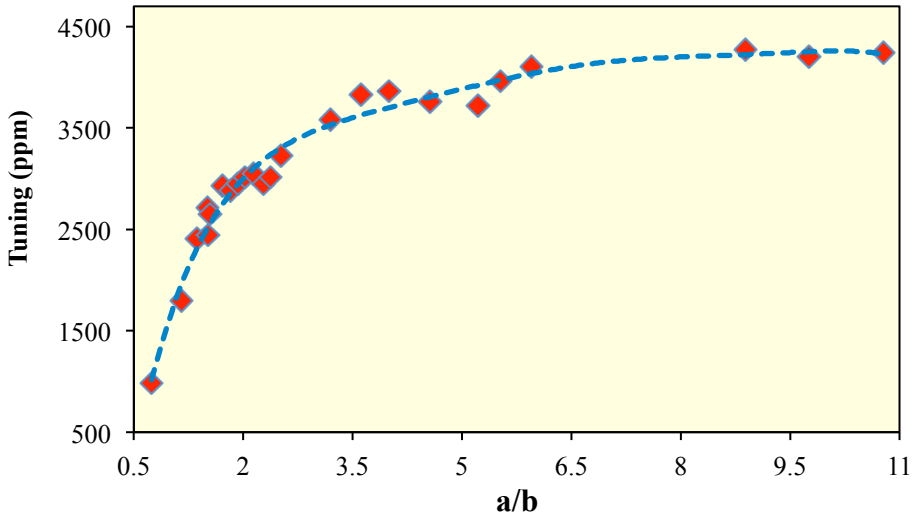

Figure 9-6. Maximum frequency shift as a function of a/b for TPoS resonators with Silicon thickness= 5µm and AlN thickness= 2µm

9-2-1-3) Effect of relative Silicon to AlN thickness

Several devices on different wafers were fabricated and tested in order to study the effect of the relative silicon to AlN thickness on tuning range. It is observed from figure 9-7 that the tuning range increases as the ratio of t_{Si}/t_{AlN} decreases. Table 9-2 also shows the tuning range for the same design which is fabricated on two wafers with different AlN thickness. The maximum 4300ppm tuning range at 29MHz is measured for the device with AlN thickness of 2 µm.

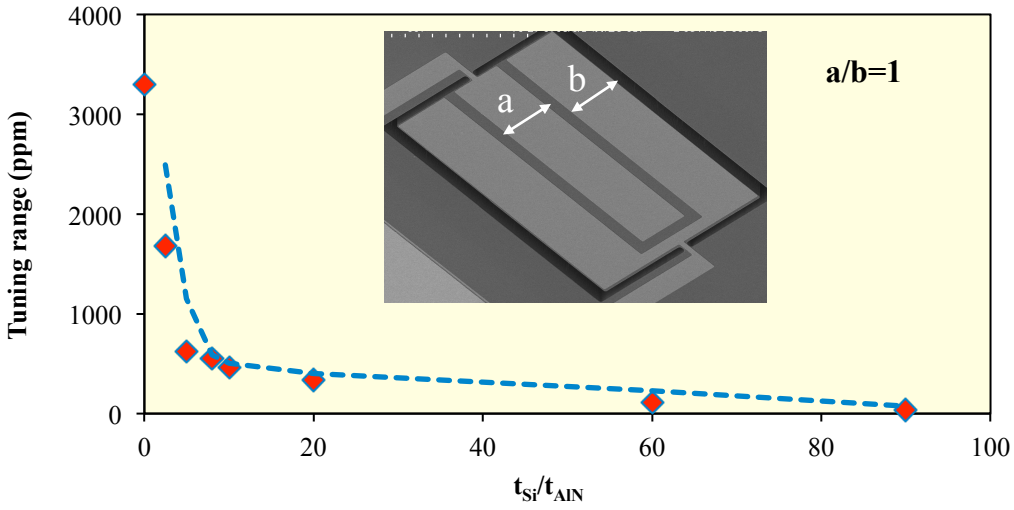

Figure 9-7. Maximum frequency shift as a function of t_{Si}/t_{AlN} for resonators with a/b=1

Table 9-2. Frequency tuning range for different AlN thickness, Si thickness=5µm

AlN	a/b	Short (MHz)	Open (MHz)	Tuning Range(ppm)
1.5µm	5.94	28.907	28.989	**2824**
2µm	5.94	29.519	29.647	**4300**

9-2-2) Tuning in Pure AlN Resonators

Based on the schematic shown in figure 9-8, designs are fabricated on a wafer with just AlN similar to the resonators in [18]. As it is expected the tuning range increases compared with TPoS resonator since the contribution of the piezoelectric modulus on the overall effective modulus is maximized. The highest overall frequency shift is measured from pure AlN devices which is more than 9000ppm at 31.5MHz. Increasing the thickness of the AlN from 1.5µm to 2µm has also caused the tuning range to increase substantially (table 9-3).

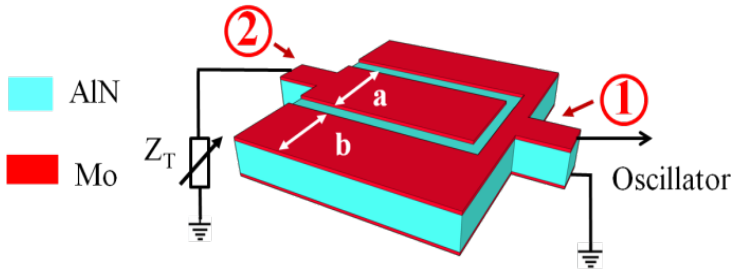

Figure 9-8. Pure AlN resonator

Table 9-3. Frequency tuning range for different AlN thickness, without Si body

AlN	a/b	Short (MHz)	Open (MHz)	Tuning Range(ppm)
1.5µm	5.94	30.493	30.745	**8260**
2µm	5.94	31.571	31.860	**9150**

9-3) TPoS oscillator tuning characterization

The schematic of the oscillator circuit used for frequency tuning is shown in figure 9-9 where port one on the resonator is integrated in the oscillation loop. The oscillation loop consists of two amplification stages (the second stage is mostly used for phase correction). Output signal waveform is converted to square wave through a comparator in order to enable jitter measurement. On the second port a varactor diode is used to implement the variable impedance.

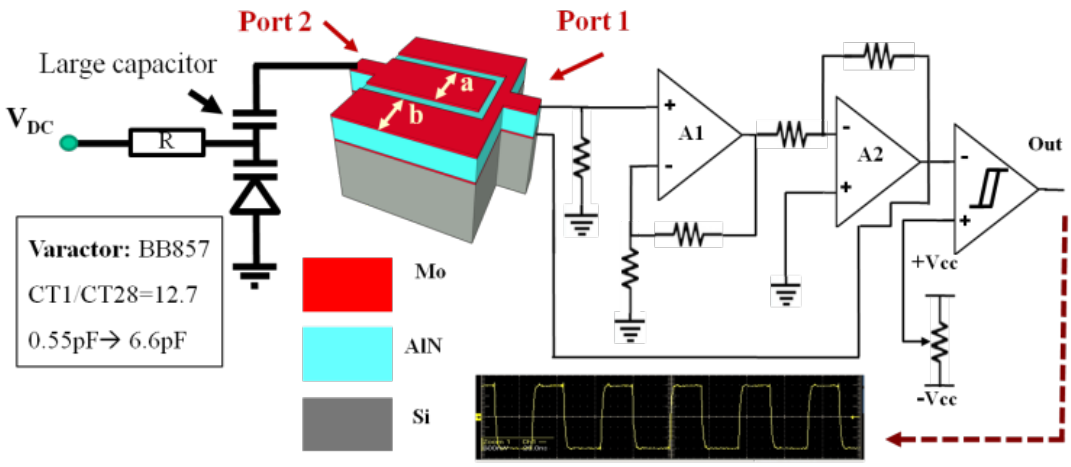

Figure 9-9. The schematic of the tunable oscillator circuit

Both TPoS and pure AlN resonators were employed in the oscillator. Through applying a tuning DC voltage to the varactor diode the effective shunt impedance at port two is varied. Therefore, the resonance frequency of the resonator and consequently the oscillation frequency of the circuit changes with the DC voltage. Preliminary results show oscillator-tuning ranges that are less than the measured frequency shift of the resonator on the probe station. This is because the tuning range is limited by the parasitic capacitor at the tuning port generated by wire bond and PCB tracks, which degrade the ideal, open condition. Another limitation is the upper and lower capacitance values of the varactor diode, which creates a smaller range of shunt impedance compared to what is achievable on the probe station. Maximum oscillator tuning from a TPoS oscillator was measured to be 1200ppm where as a tuning range of 2718ppm was recorded for a pure 2µm thick AlN resonator (figure 9-10) Assuming an approximate TCF of -25ppm/°C for the resonator [18], 2718ppm tuning range can compensate for 110ºC of temperature change.

The oscillator jitter is measured for the whole tuning range, which changes from 22ps to 23ps (cycle-to-cycle standard deviation) between DC voltages of 0v to 25v showing that the jitter is not affected by the tuning impedance.

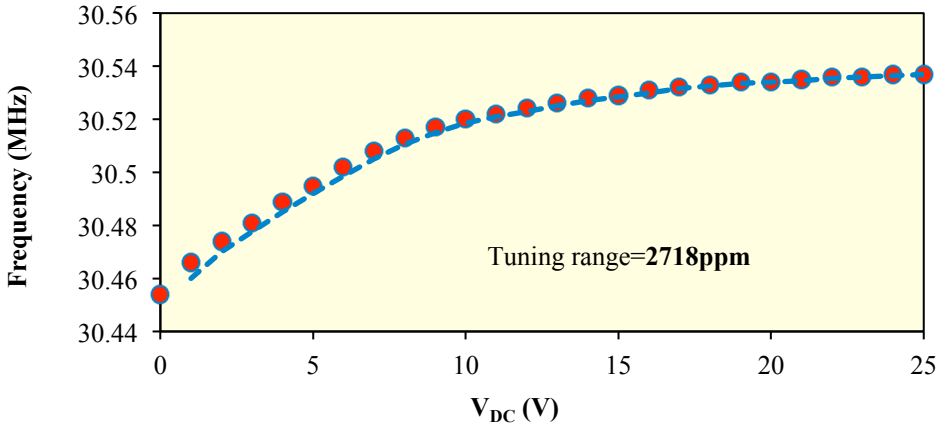

Figure 9-10. Pure AlN oscillator frequency as a function of DC voltage applied to the varactor

The oscillator circuit is placed in an environmental oven to control the temperature. Temperature is set to 10C and frequency is measured, as it is 30.458MHz. Temperature is gradually increased from 10C to 90C and it is observed that the oscillation frequency goes down (figure 9-11). It is reduced because the TCF of pure AlN resonator is negative. In order to compensate for temperature shift of frequency DC voltage manually applied to the varactor as the temperature changed. The oscillation frequency is brought back to what it was at 10C by varying the DC voltage. As it is seen in the figure 9-11 the effect of the temperature on the oscillator frequency can be compensated by the tuning technique, which is introduced in this work.

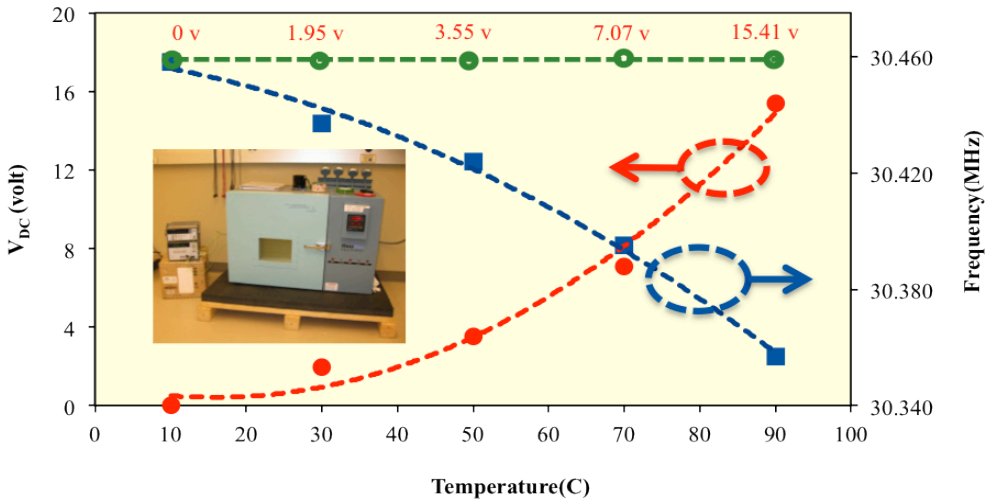

Figure 9-11. Temperature compensated oscillator test results

CHAPTER X

CONCLUSION

In this work jitter and temperature dependency of the oscillation frequency were studied. For the first time the evidence of suppressed overall noise in a MEMS-based oscillator was reported as a result of operating the resonator beyond the bifurcation point. Meanwhile, the motional impedance of the thin-film piezoelectric-on-substrate (TPoS) resonator was shown to have a dominant effect on the oscillator jitter. Resonators with lower motional impedance seem to yield lower jitter at any given oscillation amplitude. However, cycle-to-cycle jitter for all oscillators assembled based on different TPoS resonators converged to the same level of ~7psec standard deviation at very large device applied voltages.

The effect of the quality factor on nonlinearity of the TPoS resonators was investigated. Measurements confirmed that an increase in quality factor results in lower deliverable power to the device at bifurcation. However, by adding multiple supports at modal nodes along the device width a concurrent enhancement in quality factor and power handling can be achieved. By following this design strategy, 1 GHz resonators with an unloaded Q in excess of 6800 were realized with enhanced deliverable power of ~7.1 dBm at bifurcation point.

It was shown for the first time that nonlinearity in n-type doped silicon micro-resonators can be reduced by modifying the doping concentration and the resonator alignment to a different crystalline orientation. Spring hardening, a trend opposite to the commonly observed spring softening, is demonstrated in extensional [100]-oriented resonators fabricated on highly phosphorus- and Arsenic-doped silicon substrate. By choosing the right doping concentration, the overall effect of amplitude-dependent stiffness coefficients can be reduced to near zero, which results in superior linearity in resonators.

A novel method was introduced for passive temperature compensation in extensional-mode highly doped silicon microresonators. It was demonstrated that, by properly orienting an extensional-mode resonator on a highly n-type- doped silicon substrate, the TCF sign can change from positive to negative (crossing zero) within the industrial temperature range (-40C−85C). The existence of turnover point was demonstrated by fabricating AlN-on-silicon resonators on a highly phosphorus-doped ($N \sim 5 \times 10^{19}$ cm^{-3}) SOI substrate and aligning them to [100] crystallographic orientations. An overall temperature-induced frequency variation of less than 250 ppm was measured over the range of -40C−85C, showing more than 15 times reduction with respect to the conventional silicon resonators reported before. The effects of doping level, silicon and AlN thicknesses, and orientation on the TCF trend were also investigated.

MEMS oscillators with controlled temperature coefficient of frequency (TCF), assembled through mixing the frequencies of two oscillators that are made of silicon micro-resonators with known and dissimilar TCF, were also introduced. Based on this method, a MEMS oscillator is assembled in which the first-order TCF is virtually cancelled resulting in a parabolic TCF curve yielding less than 90ppm frequency shift over 25-85°C.

A new passive frequency tuning method through varying termination load connected to an isolated tuning port is demonstrated in TPoS resonators. The Effect of resonator characteristics on

the frequency tuning range is also studied. Frequency tuning range of more than 4300ppm in TPoS resonators and more than 9000ppm in pure AlN devices are reported at ~29.5MHz and ~31.5MHz respectively. An oscillator tuning range of more than 2700ppm is reported which shows a great potential for temperature compensated oscillators.

REFERENCES

[1] H. C. Nathanson, W. E. Newell, R. A. Wickstrom, and J. R. Davis, "The Resonant Gate Transistor," *IEEE Trans. Electron Devices, vol.*, vol. ED-14, no. 3, pp. 117–133, 1967.

[2] R. F. Adams and D. O. Pederson, "Temperature sensitivity of frequency of integrated oscillators," *IEEE J. Solid-State Circuits*, vol. 3, no. 4, pp. 391–396, Dec. 1968.

[3] K. E. Petersen, "Silicon as a mechanical material," *Proc. IEEE*, vol. 70, no. 5, pp. 420–457, 1982.

[4] C. T.-C. Nguyen and R. T. Howe, "An integrated CMOS micromechanical resonator high-Q oscillator," *IEEE J. Solid-State Circuits*, vol. 34, no. 4, pp. 440–455, Apr. 1999.

[5] S. Lee and C. Nguyen, "Influence of automatic level control on micromechanical resonator oscillator phase noise," in *Proc. IEEE Int. Frequency Control Symp*, 2003, pp. 341–9.

[6] W.-T. Hsu and M. Pai, "The New Heart Beat of Electronics - Silicon MEMS Oscillators," in *2007 Proceedings 57th Electronic Components and Technology Conference*, 2007, pp. 1895–1899.

[7] B. P. Harrington, M. Shahmohammadi, and R. Abdolvand, *Toward ultimate performance in GHZ MEMS resonators: Low impedance and high Q*. IEEE, 2010, pp. 707–710.

[8] H. M. Lavasani, W. Pan, B. Harrington, R. Abdolvand, and F. Ayazi, "A 76dBOhm, 1.7 GHz, 0.18um CMOS Tunable Transimpedance Ampflier Using Broadband Current Pre-Amplifier for High Frequency Lateral Micromechanical Oscillators," *IEEE J. Solid-State Circuits*, vol. 46, no. 1, pp. 224–235, Jan. 2011.

[9] C. T. C. Nguyen, "MEMS technology for timing and frequency control.," *IEEE Trans. Ultrason. Ferroelectr. Freq. Control*, vol. 54, no. 2, pp. 251–70, Feb. 2007.

[10] H. Lee, A. Partridge, and F. Assaderaghi, "Low jitter and temperature stable MEMS oscillators," *2012 IEEE Int. Freq. Control Symp. Proc.*, pp. 1–5, May 2012.

[11] H. Bhugra, Y. Wang, W. Pan, and D. Lei, “High Performance pME EMS ™ Oscillators – The Next Generati ion Frequency References,” pp. 477–480, 2011.

[12] C. Zuo, J. Van der Spiegel, and G. Piazza, “1.05-GHz CMOS oscillator based on lateral-field-excited piezoelectric AlN contour- mode MEMS resonators.,” *IEEE Trans. Ultrason. Ferroelectr. Freq. Control*, vol. 57, no. 1, pp. 82–7, Jan. 2010.

[13] R. Abdolvand, H. M. Lavasani, G. K. Ho, and F. Ayazi, “Thin-film piezoelectric-on-silicon resonators for high-frequency reference oscillator applications.,” *IEEE Trans. Ultrason. Ferroelectr. Freq. Control*, vol. 55, no. 12, pp. 2596–606, Dec. 2008.

[14] M. Shahmohammadi, B. P. Harrington, and R. Abdolvand, “Concurrent enhancement of Q and power handling in multi-tether high-order extensional resonators,” in *2010 IEEE MTT-S International Microwave Symposium*, 2010, pp. 1452–1455.

[15] M. Shahmohammadi, M. J. Modarres-Zadeh, and R. Abdolvand, “Low jitter thin-film piezoelectric-on-substrate oscillators,” in *2010 IEEE International Frequency Control Symposium*, 2010, pp. 613–617.

[16] M. S. McCorquodale and V. Gupta, “A history of the development of CMOS oscillators: The dark horse in frequency control,” in *2011 Joint Conference of the IEEE International Frequency Control and the European Frequency and Time Forum (FCS) Proceedings*, 2011, pp. 1–6.

[17] R. Melamud, S. A. Chandorkar, J. C. Salvia, G. Bahl, M. A. Hopcroft, and T. W. Kenny, “Temperature-Insensitive Composite Micromechanical Resonators,” *J. Microelectromechanical Syst.*, vol. 18, no. 6, pp. 1409–1419, Dec. 2009.

[18] G. Piazza, P. J. Stephanou, and A. P. Pisano, “Piezoelectric Aluminum Nitride Vibrating Contour-Mode MEMS Resonators,” *J. Microelectromechanical Syst.*, vol. 15, no. 6, pp. 1406–1418, Dec. 2006.

[19] R. Bechmann, A. D. Ballato, and T. J. Lukaszek, “Frequency Temperature Characteristics of Quartz Resonators Derived from the Temperature Behavior of the Elastic Constants,” *Freq. Control*, 1962.

[20] J. Vig and F. Walls, “Fundamental limits on the frequency instabilities of quartz crystal oscillators,” *Freq. Control Symp.*, 1994.

[21] K. F. Graff, “A History of Ultrasonics,” in in *Physical Acoustics V15*, Thurston and Mason, Eds. Academic Press, 1981.

[22] A. M. Nicholson, “Generating and transmitting electric currents,” U.S. Patent 2,212,845.

[23] W. G. Cady, “The piezoelectric resonator,” *Phys. Rev. A*, vol. 17, pp. 531–533, 1921.

[24] K. S. Van Dyke, “The Piezo-Electric Resonator and Its Equivalent Network,” *Proc. IRE*, vol. 16, no. 6, pp. 742–764, Jun. 1928.

[25] C. S. Lam, “A review of the recent development of MEMS and crystal oscillators and their impacts on the frequency control products industry,” in *2008 IEEE Ultrasonics Symposium*, 2008, pp. 694–704.

[26] J. T. M. van Beek and R. Puers, “A review of MEMS oscillators for frequency reference and timing applications,” *J. Micromechanics Microengineering*, vol. 22, no. 1, p. 013001, Jan. 2012.

[27] M. Sherwood, “Where is the Xtal and Oscillator Content in the iPhone?,” 2008. [Online]. Available: http://www.timing-is-everything.net/id75.html.

[28] H. Hellwig, *Frequency standards and clocks : a tutorial introduction : Hellwig, Helmut. : Free Download & Streaming : Internet Archive*. 1972.

[29] J. R. Vig, “Quartz Crystal Resonators and Oscillators For Frequency Control and Timing Applications - A Tutorial,” 2012.

[30] K. Hashimoto, *RF Bulk Acoustic Wave Filters for Communications*. Norwood: Artech House, 2009.

[31] R. Tabrizian, M. Pardo, and F. Ayazi, “A 27 MHz temperature compensated MEMS oscillator with sub-ppm instability,” in *2012 IEEE 25th International Conference on Micro Electro Mechanical Systems (MEMS)*, 2012, pp. 23–26.

[32] R. Tabrizian, G. Casinovi, and F. Ayazi, “Temperature-Stable Silicon Oxide (SilOx) Micromechanical Resonators,” *IEEE Trans. Electron Devices*, vol. 60, no. 8, pp. 2656–2663, Aug. 2013.

[33] R. C. Ruby, R. Parker, P. W. Fisher, M. A. Unkrich, and J. D. Larson, “A Temperature-Stable Film Bulk Acoustic Wave Oscillator,” *IEEE Electron Device Lett.*, vol. 29, no. 4, pp. 315–318, Apr. 2008.

[34] A. K. Samarao and F. Ayazi, “Temperature Compensation of Silicon Resonators via Degenerate Doping,” *IEEE Trans. Electron Devices*, vol. 59, no. 1, pp. 87–93, Jan. 2012.

[35] J. C. Salvia, R. Melamud, S. A. Chandorkar, S. F. Lord, and T. W. Kenny, “Real-Time Temperature Compensation of MEMS Oscillators Using an Integrated Micro-Oven and a Phase-Locked Loop,” *J. Microelectromechanical Syst.*, vol. 19, no. 1, pp. 192–201, Feb. 2010.

[36] S. Humad, R. Abdolvand, G. K. Ho, G. Piazza, and F. Ayazi, “High frequency micromechanical piezo-on-silicon block resonators,” in *IEEE International Electron Devices Meeting 2003*, 2003, pp. 39.3.1–39.3.4.

[37] R. Abdolvand and F. Ayazi, “Enhanced Power Handling and Quality Factor in Thin-Film Piezoelectric-on-Substrate Resonators,” in *2007 IEEE Ultrasonics Symposium Proceedings*, 2007, pp. 608–611.

[38] B. P. Harrington and R. Abdolvand, “In-plane acoustic reflectors for reducing effective anchor loss in lateral–extensional MEMS resonators,” *J. Micromechanics Microengineering*, vol. 21, no. 8, p. 085021, Aug. 2011.

[39] B. P. Harrington and R. Abdolvand, “Q-enhancement through minimization of acoustic energy radiation in micromachined lateral-mode resonators,” in *TRANSDUCERS 2009 - 2009 International Solid-State Sensors, Actuators and Microsystems Conference*, 2009, pp. 700–703.

[40] A. Ballato, E. P. EerNisse, and T. Lukaszek, “The Force-Frequency Effect in Doubly Rotated Quartz Resonators,” pp. 8–16, 1977.

[41] S. Stein, “Frequency and time-their measurement and characterization,” in in *Precision Frequency Control, vol.2*, E. Gerber and A. Ballato, Ed. New York: Academic Press, 1985, pp. 191–232, 399– 416.

[42] M. A. Lombardi, “Fundamentals of Time and Frequency,” in in *The mechatronics handbook*, R. H. Bishop, Ed. Boca Raton, FL: CRC Press (2002).

[43] J. R. Vig and T. R. Meeker, “The aging of bulk acoustic wave resonators, filters and oscillators,” in *Proceedings of the 45th Annual Symposium on Frequency Control 1991*, 1991, pp. 77–101.

[44] R. B. Belser and W. H. Hicklin, “Aging Characteristics of Quartz Resonators with Comments on the Effects of Radiation,” in *17th Annual Symposium on Frequency Control*, 1963, pp. 127–175.

[45] “Fundamentals of Quartz Oscillators,” *Hewlett-Packard Appl. Note AN 200-2, Hewlett-Packard Co.*, pp. 1–28, 1997.

[46] V. Kaajakari, T. Mattila, A. Lipsanen, and A. Oja, “Nonlinear mechanical effects in silicon longitudinal mode beam resonators,” *Sensors Actuators A Phys.*, vol. 120, no. 1, pp. 64–70, 2005.

[47] L. C. Shao, M. Palaniapan, and W. W. Tan, “The nonlinearity cancellation phenomenon in micromechanical resonators,” *J. Micromechanics Microengineering*, vol. 18, no. 6, p. 065014, Jun. 2008.

[48] M. Agarwal, K. Park, R. Candler, M. Hopcroft, C. Jha, R. Melamud, B. Kim, B. Murmann, and T. W. Kenny, “Non-linearity cancellation in MEMS resonators for improved power-handling,” in *IEEE InternationalElectron Devices Meeting, 2005. IEDM Technical Digest.*, 2005, pp. 286–289.

[49] F. D. Bannon, J. R. Clark, and C. T.-C. Nguyen, “High-Q HF microelectromechanical filters,” *IEEE J. Solid-State Circuits*, vol. 35, no. 4, pp. 512–526, Apr. 2000.

[50] V. Kaajakari, T. Mattila, A. Oja, and H. Seppa, “Nonlinear Limits for Single-Crystal Silicon Microresonators,” *J. Microelectromechanical Syst.*, vol. 13, no. 5, pp. 715–724, Oct. 2004.

[51] M. Shahmohammadi, D. Dikbas, B. P. Harrington, and R. Abdolvand, “Passive tuning in lateral-mode thin-film piezoelectric oscillators,” in *2011 Joint Conference of the IEEE International Frequency Control and the European Frequency and Time Forum (FCS) Proceedings*, 2011, pp. 1–5.

[52] T. H. Lee and A. Hajimiri, “Oscillator phase noise: a tutorial,” *IEEE J. Solid-State Circuits*, vol. 35, no. 3, pp. 326–336, Mar. 2000.

[53] K. Y. Kim and W. Sachse, “Nonlinear elastic equation of state of solids subjected to uniaxial homogeneous loading,” *J. Mater. Sci.*, vol. 35, no. 13, pp. 3197–3205, Jul. 2000.

[54] R. Keyes, “Electronic Effects in the Elastic Properties of Semiconductors,” *Solid State Phys.*, pp. 37–90, 1968.

[55] J. Hall, “Electronic Effects in the Elastic Constants of n-Type Silicon,” *Phys. Rev.*, vol. 161, no. 3, pp. 756–761, Sep. 1967.

[56] H. Fatemi and R. Abdolvand, “Fracture limit in thin-film piezoelectric-on-substrate resonators: Silicon VS. diamond,” in *2013 IEEE 26th International Conference on Micro Electro Mechanical Systems (MEMS)*, 2013, pp. 461–464.

[57] B. Yurke, D. S. Greywall, A. N. Pargellis, and P. A. Busch, “Theory of amplifier-noise evasion in an oscillator employing a nonlinear resonator,” *Phys. Rev. A*, vol. 51, no. 5, p. 4211 LP – 4229, May 1995.

[58] A. Hajimiri and T. H. Lee, “A general theory of phase noise in electrical oscillators,” *IEEE J. Solid-State Circuits*, vol. 33, no. 2, pp. 179–194, 1998.

[59] M. Shahmohammadi, B. P. Harrington, and R. Abdolvand, “Zero temperature coefficient of frequency in extensional-mode highly doped silicon microresonators,” in *2012 IEEE International Frequency Control Symposium Proceedings*, 2012, pp. 1–4.

[60] M. Shahmohammadi, B. P. Harrington, J. Gonzales, and R. Abdolvand, “Temperature-compensated extensional-mode MEMS resonators on highly N-type doped silicon substrates,” in *in Proc. Solid-State Sens., Actuators, Microsyst. Workshop (Hilton Head 2012), Hilton Head Island, SC, USA*, pp. 371–374.

[61] M. Shahmohammadi, B. P. Harrington, and R. Abdolvand, “Turnover Temperature Point in Extensional-Mode Highly Doped Silicon Microresonators,” *IEEE Trans. Electron Devices*, vol. 60, no. 3, pp. 1213–1220, Mar. 2013.

[62] T. Pensala, A. Jaakkola, M. Prunnila, and J. Dekker, “Temperature compensation of silicon MEMS Resonators by Heavy Doping,” *2011 IEEE Int. Ultrason. Symp.*, pp. 1952–1955, Oct. 2011.

[63] H. McSkimin, W. Bond, E. Buehler, and G. Teal, “Measurement of the Elastic Constants of Silicon Single Crystals and Their Thermal Coefficients,” *Phys. Rev.*, vol. 83, no. 5, pp. 1080–1080, Sep. 1951.

[64] R. J. Bruls, H. T. Hintzen, G. de With, and R. Metselaar, “The temperature dependence of the Young’s modulus of MgSiN2, AlN and Si3N4,” *J. Eur. Ceram. Soc.*, vol. 21, no. 3, pp. 263–268, 2001.

[65] K. Sundaresan, S. Pourkamali, and F. Ayazi, “Temperature Compensated IBAR Reference Oscillators,” in *19th IEEE International Conference on Micro Electro Mechanical Systems*, 2006, pp. 910–913.

[66] A. Hajjam, A. Rahafrooz, and S. Pourkamali, “Sub-100ppb/°C temperature stability in thermally actuated high frequency silicon resonators via degenerate phosphorous doping and bias current optimization,” in *2010 International Electron Devices Meeting*, 2010, pp. 7.5.1–7.5.4.

[67] K. Sundaresan, G. Ho, S. Pourkamali, and F. Ayazi, “A Low Phase Noise 100MHz Silicon BAW Reference Oscillator,” *IEEE Cust. Integr. Circuits Conf. 2006*, no. CICC, pp. 841–844, Sep. 2006.

[68] a. Ballato, “P3H-1 Tunable Solidly Mounted Resonators,” *2007 IEEE Ultrason. Symp. Proc.*, pp. 1870–1873, Oct. 2007.

[69] W. W. CLARK, “Vibration Control with State-Switched Piezoelectric Materials,” *J. Intell. Mater. Syst. Struct.*, vol. 11, no. 4, pp. 263–271, Apr. 2000.

APPENDIX I

The formulation of Mixer-enabled MEMS oscillators with controlled TCF

A general block diagram of a mixer-enabled MEMS oscillator with controlled TCF is shown in figure I-1.

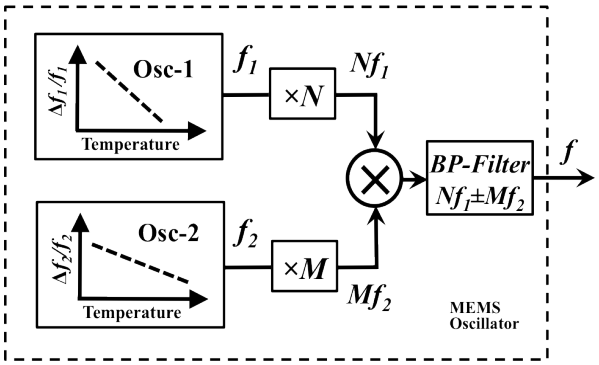

Figure I-1. Block diagram of a mixer-enabled MEMS oscillator

Considering the first and second order terms, the frequency drifts versus temperature as well as the temperature turnover points of oscillators 1 and 2 are given as:

$$\Delta f_1(T)/f_1(T_0) = \alpha_1 \Delta T + \beta_1 \Delta T^2 \qquad T_{p1} = -\alpha_1/2\beta_1 \qquad \beta_1 \neq 0 \qquad \text{I.1}$$

$$\Delta f_2(T)/f_2(T_0) = \alpha_2 \Delta T + \beta_2 \Delta T^2 \qquad T_{p2} = -\alpha_2/2\beta_2 \qquad \beta_2 \neq 0 \qquad \text{I.2}$$

where, T_0 is a reference point.

By manipulating the I.1 and I.2:

$$f_1(T) = f_1(T_0) + \alpha_1 f_1(T_0)\Delta T + \beta_1 f_1(T_0)\Delta T^2 \qquad \text{I.3}$$

$$f_2(T) = f_2(T_0) + \alpha_2 f_2(T_0)\Delta T + \beta_2 f_2(T_0)\Delta T^2 \qquad \text{I.4}$$

The mixer output can be filtered to have both frequencies at the output:

$$f = Nf_1 \pm Mf_2 \quad \text{I.5}$$

Putting f_1 and f_2 from I.3 and I.4 into I.5:

$$f(T) = (Nf_{01} \pm Mf_{02}) + (N\alpha_1 f_{01} \pm M\alpha_2 f_{02})\Delta T + (N\beta_1 f_{01} \pm M\beta_2 f_{02})\Delta T^2 \quad \text{I.6}$$

$$f(T) = f_0 + \alpha f_0 \Delta T + \beta f_0 \Delta T^2$$

$$\Delta f(T)/f_0 = \alpha \Delta T + \beta \Delta T^2 \quad \text{I.7}$$

$$f_0 = Nf_{01} \pm Mf_{02} \quad \text{I.8}$$

$$\alpha = \frac{N\alpha_1 f_{01} \pm M\alpha_2 f_{02}}{Nf_{01} \pm Mf_{02}} \quad \text{I.9}$$

$$\beta = \frac{N\beta_1 f_{01} \pm M\beta_2 f_{02}}{Nf_{01} \pm Mf_{02}} \quad \text{I.10}$$

The first and second order of temperature coefficient of frequency as well as turnover point of the output (f) in terms of the first and second order coefficients and turnover points of oscillator 1 and 2 are given as follow:

$$\alpha = \frac{1}{1 \pm \lambda}\alpha_1 \pm \frac{\lambda}{1 \pm \lambda}\alpha_2 \quad \text{I.11}$$

$$\beta = \frac{1}{1 \pm \lambda}\beta_1 \pm \frac{\lambda}{1 \pm \lambda}\beta_2 \quad \text{I.12}$$

$$T_p = \frac{1}{1 \pm \gamma}T_{p1} \pm \frac{\gamma}{1 \pm \gamma}T_{p2} \quad \text{I.13}$$

where,

$$\lambda = \frac{Mf_{02}}{Nf_{01}}$$

$$\gamma = \frac{M\beta_2 f_{02}}{N\beta_1 f_{01}} = \frac{\beta_2}{\beta_1}\lambda$$

Special case:

Setting the first order TCF, α, to zero, the following condition should be satisfied:

$$N\alpha_1 f_{01} \pm M\alpha_2 f_{02} = 0 \quad \text{I.14}$$

or,

$$\alpha_1/\alpha_2 = \pm Mf_{02}/Nf_{01} \quad \text{I.15}$$

VITA

Mohsen Shahmohammadi Ghahsareh

Candidate for the Degree of

Doctor of Philosophy

Thesis: FREQUENCY STABILITY IN THIN-FILM PIEZOELECTRIC-ON-SUBSTRATE OSCILATORS

Major Field: Electrical Engineering

Education:

Completed the requirements for the Doctor of Philosophy in electrical engineering at Oklahoma State University, Stillwater, Oklahoma in December 2013.

Completed the requirements for the Master of Science Electrical Engineering at K. N. Toosi University of Technology, Tehran, Iran in 1999.

Completed the requirements for the Bachelor of Science in Electrical Engineering at Isfahan University of Technology, Isfahan, Iran in 1995.

Mohsen was born in 1973 in Isfahan, Iran. He received the B.S. degree in electrical engineering from Isfahan University of Technology, Isfahan, Iran and the M.S. degree from K.N. Toosi university of Technology, Tehran, Iran in 1995 and 1998 respectively. He is currently pursuing the Ph.D. degree in electrical engineering at Oklahoma State University, Tulsa, Oklahoma. His research interests include piezoelectric micromechanical resonators for oscillator circuits.